Schriftenreihe des
Instituts für Mikrowellentechnik



3

Linus Böhm

Measurement Techniques for Highly Integrated mm-Wave Antennas

Institut für Mikrowellentechnik
Universität Ulm

Measurement Techniques for Highly Integrated mm-Wave Antennas



ulm university universität
uulm

Measurement Techniques for Highly Integrated mm-Wave Antennas

DISSERTATION

zur Erlangung des akademischen Grades eines

DOKTOR-INGENIEURS (Dr.-Ing.)

der Fakultät für Ingenieurwissenschaften, Informatik und Psychologie der Universität Ulm

von

Linus Böhm

aus Sindelfingen

Gutachter:	Prof. Dr.-Ing. Christian Waldschmidt
	Prof. Dr.-Ing. Dirk Heberling
Amtierender Dekan:	Prof. Dr.-Ing. Maurits Ortmanns

Ulm, 18. März 2019

Bibliografische Information der Deutschen Nationalbibliothek
Die Deutsche Nationalbibliothek verzeichnet diese Publikation in der Deutschen Nationalbibliografie; detaillierte bibliografische Daten sind im Internet über http://dnb.dnb.de abrufbar.

Dissertation, Universität Ulm,
Fakultät für Ingenieurwissenschaften, Informatik und Psychologie, 2019

Impressum
Universität Ulm
Institut für Mikrowellentechnik
Prof. Dr.-Ing. Christian Waldschmidt
Albert-Einstein-Allee 41
89081 Ulm
https://www.uni-ulm.de/mwt

Eine Übersicht über alle Bände der Schriftenreihe finden Sie unter
https://www.uni-ulm.de/mwtschriften

Diese Veröffentlichung ist im Internet auf dem institutionellen Repositorium der Universität Ulm (https://oparu.uni-ulm.de) verfügbar und dort unter der Lizenz CC BY-NC-ND 4.0 publiziert.



Details zur Lizenz finden Sie unter
https://creativecommons.org/licenses/by-nc-nd/4.0/

ISBN 978–3–948303–04–4 ISBN 978–3–948303–05–1 (E-Book)

Acknowledgments

This work was written during my time at the Institute of Microwave Engineering at Ulm University.

First and foremost, I would like to thank my advisor, Prof. Dr. Christian Waldschmidt, for his guidance and insight throughout this thesis. He granted me the required freedom for my research, while also nudging me in the right direction when needed. I would also like to thank Prof. Dr. Dirk Heberling for his interest in this work and for co-examining this thesis, and Dr. Jürgen Hasch, whose initiative brought me to Ulm University.

A special thanks to all my colleagues at the institute, who made my time in Ulm extremely enjoyable — both in and outside of work; particularly to Dr. Martin Hitzler for keeping me company at frequencies beyond 100 GHz and for the many helpful discussions. I am very grateful to have shared an office for almost four years with Claudia Vasanelli, who became a good friend and who offered her help whenever needed.

Thank you to Dr. Frank Bögelsack for his frank (!) and honest nature, his great sense of humor, and his constant support from start to finish concerning all aspects of this thesis.

Furthermore, I would like to thank my students, whose many contributions were invaluable to this thesis.

Lastly, I would like to thank Mary Teresa for her support and her keen proofreader's eye, and of course, my parents for always being there for me.

Sindelfingen, March 2019

Linus Böhm

Contents

1 Introduction **1**
- 1.1 Antenna Measurements . . . 2
- 1.2 Objective and Outline . . . 7

2 Measurement Setups and Accuracy **11**
- 2.1 mm-Wave Antenna Measurements . . . 11
- 2.2 Uncertainty Analysis . . . 14

3 Robotic Antenna Measurement Setup **19**
- 3.1 Requirements . . . 19
- 3.2 Components . . . 21
  - 3.2.1 Robot Controller . . . 21
  - 3.2.2 Robot . . . 22
  - 3.2.3 Measurement Equipment . . . 22
  - 3.2.4 Probe Station . . . 23
- 3.3 Measurement Procedure and Alignment . . . 24
- 3.4 Supported Measurements . . . 28
- 3.5 Optimization . . . 33
  - 3.5.1 Cable Routing . . . 34
  - 3.5.2 Robot and Probe Station Reflections . . . 34
  - 3.5.3 Movement Limitations . . . 35
  - 3.5.4 Chuck Reflections . . . 36
- 3.6 Wafer-Probe Distortions . . . 38
- 3.7 Comparison Measurement – Simulation . . . 48
  - 3.7.1 Horn-Antenna Measurements . . . 49
  - 3.7.2 Integrated Antenna Measurements . . . 53

4 Uncertainty **59**
- 4.1 Error Sources . . . 60
- 4.2 Measurement Campaign . . . 63
- 4.3 Achievable Accuracy . . . 63

5 Reflection Suppression in Post-Processing **67**
5.1 Post-Processing Techniques 68
5.2 Source Reconstruction 70
5.3 MARS 78
5.3.1 Spherical Wave Expansion 81
5.3.2 Cylindrical Wave Expansion 91
5.3.3 Antenna Displacement 95
5.3.4 Patch Antenna at 120 GHz 98
5.3.5 Passive Integrated Antenna Measurements 104
5.3.6 Active Integrated Antenna Measurements 116

6 Conclusion **123**

A Appendix **127**

Bibliography **129**

Index of variable names, indices, and acronyms

As far as possible, variable names and indices were chosen according to DIN 1304 in order to avoid double entries as far as possible. For all remaining double entries, the correct meaning can be gathered from the context. Common running indices and basic operators are not listed here.

In accordance with DIN 1304 all symbols are displayed in italics. The page numbers state the page a certain variable is used for the first time.

Symbols

ϕ	Azimuth angle	12
J_n	Bessel function of the first kind of order n	82
Y_n	Bessel function of the second kind of order n	82
j_n	Spherical Bessel function of the first kind of order n	81
n_n	Spherical Bessel function of the second kind of order n	81
k	Coverage factor	16
$B_m^{(1)}$	First cylindrical mode coefficient	93
$B_m^{(2)}$	Second cylindrical mode coefficient	93
D	Diameter	3
d	Distance	3
D	Directivity of an antenna	3
η	Efficiency of an antenna	3
$\mathbf{E}$	E-field vector	29
E_ϕ	E-field in ϕ-direction	19
E_r	E-field in r-direction	72
E_θ	E-field in θ-direction	19
θ	Elevation angle	12
$\mathbf{J}$	Electric current density vector	71
x	Error source	15
U_c	Expanded uncertainty budget	16
G	Gain of an antenna	3
$\mathbf{H}$	H-field vector	29

$H_m^{(1)}$	Hankel function of the first kind of order m	91
$H_m^{(2)}$	Hankel function of the second kind of order m	91
$h_n^{(1)}$	Spherical Hankel function of the first kind of order n	81
$h_n^{(2)}$	Spherical Hankel function of the second kind of order n	81
Z	Impedance	3
Δ	Laplace operator	81
P_n^m	Associated Legendre function of degree n and order m	84
$\bar{P}_n^m$	Normalized associated Legendre function of degree n and order m	84
δ	Loss tangent	2
$\mathbf{M}$	Magnetic current density vector	71
$\hat{\mathbf{n}}_S$	Normal vector to surface S	72
ε	Permittivity	2
μ	Permeability	71
$\mathbf{f}$	Plane wave spectrum	30
χ	Polarization angle	4
P	Power	5
S	Power density	29
$\mathbf{k}$	Propagation factor vector	31
C	Radiation pattern of an antenna	3
c	Sensitivity	15
Σ_M	Measurement surface	69
Σ_R	Reconstruction surface	69
$\mathbf{m}_{mn}^{(4)}$	Spherical wave function (TE)	86
$\mathbf{M}_{mn}^{(4)}$	Normalized spherical wave function (TE)	87
$\mathbf{n}_{mn}^{(4)}$	Spherical wave function (TM)	86
$\mathbf{N}_{mn}^{(4)}$	Normalized spherical wave function (TM)	87
$B_{mn}^{(1)}$	First spherical mode coefficient	87
$B_{mn}^{(2)}$	Second spherical mode coefficient	87
s	Standard deviation	16
R_X	Receiver	11
T_X	Transmitter	11
u	Uncertainty	16
u_c	Uncertainty budget	16
$\boldsymbol{\psi}$	Scalar wave function	81
η	Wave impedance	71
λ	Wavelength	3

k	Wave number	25
Z	Impedance	72

Indices

0	Free space	30
co	Co-polarization	32
cross	Cross-polarization	32
eq	Equivalent	71
F	Fraunhofer	3
i	Isotropic radiator	5
in	Input	3
meas	Measurement	14
r	Relative	2
rad	Radiated	29
Rx	Receiver	50
sim	Simulation	15
Tx	Transmitter	50

Acronyms

AUT	Antenna under test	4
CATR	Compact antenna test range	3
CMC	Cylindrical mode coefficient	93
DoF	Degrees of freedom	13
FSPL	Free-space path loss	44
GSG	Ground signal ground	23
GUI	Graphical user interface	21
IC	Integrated circuit	23
MARS	Mathematical absorber reflection suppression	9
MMIC	Monolithic microwave integrated circuit	1
MoM	Method of moments	72
MRC	Minimum radius cylinder	95
MRE	Maximum radial extend	88
MRS	Minimum radius sphere	70
mvg	Microwave Vision Group	73

NIST	National Institute of Standards and Technology	13
OTF	On the fly	28
PCB	Printed circuit board	6
PTP	Point to point	28
PVC	Polyvinyl chloride	37
RWG	Rao-Wilton-Glisson	72
SGH	Standard gain horn	19
SiGe	Silicon-Germanium	1
SMC	Spherical mode coefficient	87
SRM	Source reconstruction method	69
TE	Transverse electric	86
TM	Transverse magnetic	86
VNA	Vector network analyzer	11

1 Introduction

A mere 100 years after they established the basics for wireless transmission of electromagnetic waves, Heinrich Hertz and Guglielmo Marconi would probably marvel at how many new technologies have emerged that rely on wireless transmission and at how much of an impact it has had on modern society. Climate monitoring, traffic control, space exploration, imaging techniques in medicine, the entertainment industry, and communication are just some of the areas which have undergone fundamental changes enabled by wireless data transmission and remote sensing. With the development of handheld devices and the wide distribution of smartphones, wireless technologies have arrived in the day-to-day life of billions of people, who carry complex transmitters in their pockets and who have grown so used to the features that handheld devices seem to be indispensable in modern society—not even 20 years after the first smartphone was unveiled.

The ever-growing user base and the increasing importance of cloud services pose high demands on the required data transfer rate and handheld devices push the development of small and cheap components [1, 2]. Facilitated by the development of faster integrated transistors with maximum oscillation frequencies of 500 GHz [3] and beyond [4, 5] in Silicon-Germanium (SiGe)-technology, research has moved towards mm-wave integrated circuits that operate at frequencies above 100 GHz, where the available bandwidths of many GHz increase the channel capacity and satisfy the need for higher data rates [6, 7]. Furthermore, the small dimensions of passive components make small, inexpensive transceivers possible [8–10, 11, 12]. With wavelengths of less than 3 mm, it is possible to integrate the antenna and other passive components on the same chip as the active circuitry, such that only low frequency connections to outside circuitry are required [13, 14, 15]. This makes it possible to fabricate mm-wave devices that can be integrated into a single monolithic microwave integrated circuit (MMIC) and that are energy-efficient, inexpensive, and easy to utilize in a larger system.

With millions of users and safety-relevant applications (e.g. automated driving), ensuring reliable and efficient transmission is paramount and requires

finely tuned components. One crucial component of wireless devices are antennas since they serve as the link between guided signals and free-space propagation. In 2010, users of the newly released iPhone 4 noticed that the network connection could be lost depending on the users' finger placement on the device. If a certain area of the device was covered, the performance of the antenna was seriously impeded, which resulted in plenty of negative press and a temporary loss in market cap of around 9 billion dollars [16].

This incident not only highlights the importance of an antenna on the performance of a transceiver module, but also the importance of proper measurement procedures to verify the reliable operation of an antenna [17].

However, these measurement procedures for the characterization of integrated antennas have not yet been established. The measurement of integrated antennas is a relatively new research area and emerging challenges are not addressed by the IEEE standard test procedures for antennas [18] and many of the problems arising at mm-wave frequencies have yet to be investigated.

The small wavelengths put stringent requirements on the mechanical accuracy of measurement setups and small deviations can result in comparatively large phase errors [19]. Antenna sizes of less than 1 mm and the required contacting apparatuses interact with the radiated fields and distort the results of integrated antenna measurements. Some of the concepts that are used to measure antennas at lower frequencies are not applicable to integrated antenna measurements, which is why new measurement techniques are needed for integrated mm-wave antenna measurements.

1.1 Antenna Measurements

After an antenna structure has been designed, optimized in simulation, and fabricated, the performance of the prototype has to be verified through measurements. Only measurement results can ensure that the basic principle of the antenna is viable, that the antenna works as desired in the final deployment environment (which might be hard to model in a simulation), that the used materials have the expected properties, and that the fabrication process does not yield malfunctioning antennas. The importance of measurements is especially high for mm-wave frequencies as the fabrication of small structures is challenging and material properties are often only known at lower frequencies with sufficient accuracy. Deviations between the assumed and the true material parameters (e.g. permittivity ε_r and loss tangent δ) is one of the main reasons

for erroneous simulation results [20].

Antennas can be tested for a number of different characteristics, among which are the radiation pattern C, the directivity D, the gain G, the radiation efficiency η, the input impedance Z_{in}, and the polarization of the antenna [21]. Ideally, these characteristics would be measured with a setup that only contains the AUT without any supporting structures or feeding networks that influence the measurement. However, this is not possible in a real world measurement setup. Various different test ranges have been developed and optimized to obtain accurate measurement results, such as near-field, far-field, and compact antenna test ranges (CATRs) [18].

In most cases the antenna properties in the far field of the AUT are of interest. The far field is defined as the observable radiation in a distance larger than the Fraunhofer distance

$$d_{\text{F}} = \frac{2D^2}{\lambda}\,, \tag{1.1.1}$$

with the wavelength λ and the aperture diameter D. The parameter d_{F} marks the distance for which the phase error is $\lambda/16$ when approximating the spherical wave of an antenna with a planar wave front, with a decreasing phase error for larger distances. Far-field ranges have an antenna separation larger than the Fraunhofer distance, such that the radiation characteristics can be obtained without any additional post-processing of the measurement data. Usually the AUT is mounted on a rotary table with a static probe antenna, which means that the radiation characteristics for different azimuth, elevation, and polarization angles of the AUT can be obtained as indicated in Fig. 1.1. Antennas with a sufficiently small far-field distance (i.e. electrically small aperture) can be measured in anechoic chambers, which have absorber covered walls to prevent unwanted reflections that interfere with the measurement results, a problem that can occur from ground reflections in outside test ranges.

Anechoic chamber measurements of larger antennas with a large far-field distance can either be performed in a CATR or with a near-field measurement of the AUT with a subsequent near-field to far-field transformation [22–25]. A compact range uses one or multiple curved reflectors to increase the separation between the feed antenna and the AUT as shown in Fig. 1.2. The reflector is used to collimate the field of the feed and usually has serrated edges to reduce edge diffraction. The volume, where the sum of taper and peak-to-peak ripple is less than $\pm 0.5\,\text{dB}$ for the amplitude and less than $\pm 0.5\,^\circ$ for the phase is

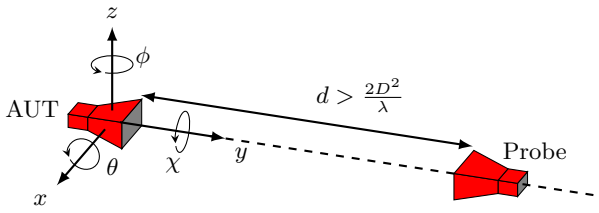

Fig. 1.1: Schematic of a far-field measurement setup with static probe. The radiation pattern can be measured by turning the antenna under test (AUT) around its phase center in ϕ- and θ-direction. A rotation of the AUT in χ-direction sets the polarization.

called the quiet zone [26, 27]. The quality of the pseudo plane wave in the quiet zone determines the achievable measurement accuracy, which is why the reflector has to be shaped with high accuracy and other unwanted reflections have to be minimized. The radiation pattern and polarization of an antenna can be obtained by rotating the AUT around its phase center in the quiet zone of the CATR.

In a near-field measurement the radiation of the AUT is measured on a surface in close proximity to the AUT. The most common measurement geometries are planar, cylindrical, and spherical surfaces as these allow for a simple transformation into the far field and can be measured with fairly easy to realize positioning systems. After the complex vector field information has been obtained on a well-defined surface, the radiation pattern can be calculated at an arbitrary distance from the AUT and thus, the far-field pattern can be determined. As the measurement results are weighted with the radiation pattern of the near-field probe, which changes over the scanning position especially for planar and cylindrical scans, a probe correction can be performed, which reduces the influence of the near-field probe and thus increases the measurement accuracy [28–31].

The directivity D describes the ability of an antenna to direct the radiation into a certain spatial region [32] and is often approximated using the 3 dB beamwidths in E- and H-plane. The measurement of the directivity requires scanning the radiated fields on a sphere around the AUT and can be calculated by integrating over the measured E-field [33].

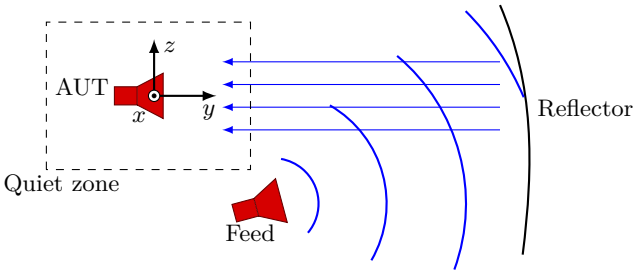

Fig. 1.2: Schematic of a compact range measurement setup. The radiation pattern and polarization can be measured by turning the AUT around the x-, y-, and z-axis.

The antenna gain G is specified as the ratio between the power that is fed into an antenna P_{in} and the input power of an isotropic radiator $P_{\text{in,i}}$, if both powers were set such that the power density of both antennas are equal at a given distance in the far field. Gain measurements can be performed using the gain comparison method [34,35]. This method requires a reference antenna of known gain. By comparing the measurement result of the AUT to a measurement of the reference antenna, while taking into account the attenuation of any connectors that were altered between the two measurements, the gain of the AUT can be calculated. Other gain measurements are the two- and the three-antenna methods, which require two of the same AUTs or three different AUTs, respectively [36–38].

The efficiency η of an antenna is defined as the ratio of the radiated power over the input power to the antenna and is especially important for handheld devices as inefficient antennas can drain the battery. The efficiency can be determined via the input and radiated power and as the ratio between gain and directivity $\eta = G/D$. Other methods use reverberation chambers [39], or a so-called Wheeler cap [40, 41], which is used to short the radiation resistance of the AUT. By measuring the input resistance with and without the cap, the efficiency can be calculated. Furthermore, improved Wheeler-cap methods have been proposed since [42–44].

While these methods have been applied to traditional antenna measurements successfully, integrated antenna measurements are substantially different and

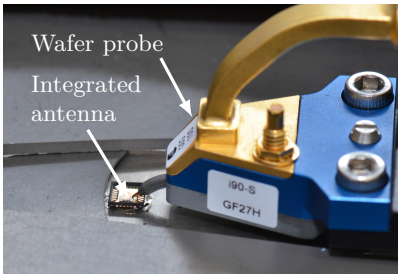

(a) Passive: Integrated antenna within a package fed with a comparatively much larger wafer probe.

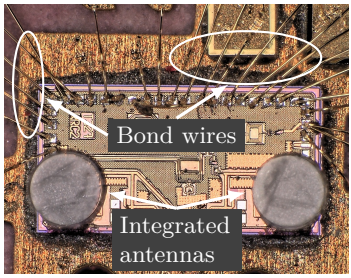

(b) Active: Integrated antennas fed by active circuitry on the chip. Connections to outside circuitry through bond wires.

Fig. 1.3: Both passive and active measurements suffer distortions from surrounding objects.

cannot be measured using the same approaches. Traditional antenna measurement setups usually use flexible coaxial cables to connect the AUT with the measurement device. Flexible connectors make it possible to turn the AUT as indicated in Fig. 1.1 in order to obtain the angle-dependent radiation pattern. Integrated antennas, on the other hand, have to be contacted using wafer probes, which have to be placed precisely on the corresponding pads on the chip that holds the AUT. The wafer-probe tips that connect to the pads are fragile and can be damaged even by slight movements, which would render the wafer probe unusable and therefore, the integrated AUT has to remain static during a measurement. Small chip dimensions of around $1\,\mathrm{mm}^2$ limit the distance between the wafer probe and AUT as it is not possible to use long feeding lines to increase the separation, which would be a viable option in printed circuit board (PCB)-technology. Additionally, antennas realized in SiGe-technology cannot radiate through the substrate and therefore, wafer probe and boresight direction are in the same hemisphere. As wafer probes are much bigger than the AUT itself (see Fig. 1.3a) they present a large reflective surface that has a significant impact on the measurement results [45] and signal blockage occurs in the shadow of the probe, reducing the spherical measurement area [46]. Sufficient shielding of the probe with absorbing material is hampered by its small size and fragility. In traditional antenna measurements, in contrast, the influ-

ence of the feeding structures and connectors often has a negligible influence on the results, as they are usually located on the back of the antenna with a much smaller relative size. The usage of wafer probes to contact antenna prototypes also requires a solid probe station in the measurement setup that guarantees minimal relative movement between the wafer probe and the landing pads on the surface of the MMIC. A wafer chuck is used to carry the AUT and hold it in place. Probe station and chuck are usually made of metal, which causes further unwanted reflections.

If an antenna is integrated on a chip with active circuitry that can generate the transmit frequency, no wafer probe is required to feed the AUT. In this case, however, bond wires are needed for the power supply and low frequency connections, as shown in Fig. 1.3b. While being much smaller than wafer probes, these bond wires are also extremely close to the antenna and disturb measurements.

Efficiency measurements using a reverberation chamber or Wheeler cap are also extremely difficult to realize for integrated antennas. The large dimensions of a probe station would make it difficult to integrate it within a reverberation chamber and the small chip dimensions and the wafer probe inhibit a closed, well grounded Wheeler-cap design, which would be required for meaningful Wheeler-cap measurement results. Another approach to measuring the efficiency would be to measure the input power to the AUT and compare it to the total radiated power that is radiated into free space by the antenna. The radiated power can be calculated by integrating over the power density on a sphere around the AUT; however, the input power to the antenna is difficult to measure, because on-chip power measurement is difficult to realize and calibrate at mm-wave frequencies with sufficient accuracy to obtain reliable measurement results.

1.2 Objective and Outline

This work seeks to make reliable integrated antenna measurements possible—despite the aforementioned problems and challenges that accompany the characterization of such antennas. The measurement should not only give a best-effort estimate of the antenna parameters, but it should rather provide a dependable result as close as possible to the true value of the measurand for isolated and in-system antennas. For a dependable measurement result, a reliable statement about the achievable measurement accuracy for different measurement

quantities is to be derived. In order to minimize measurement errors, hardware modifications and post-processing algorithms are to be investigated to reduce distortions of standard, off-the-shelf components that exhibit non-ideal characteristics for antenna measurements in terms of reflectivity and size.

As classic setups do not satisfy the requirements of integrated antenna measurements, a new setup architecture dedicated to integrated antenna measurements is necessary. The setup should not only provide sufficient mechanical and electrical accuracy, but it should also offer high flexibility to support different measurement quantities and scenarios, as this lays the foundation for the analysis of different error sources and for the post-processing procedures.

In order to meet these goals, the main areas of focus were the following:

- Measurement setup architecture: as rotating AUT setups are not applicable for integrated antennas, a new setup with a static AUT was developed.
- Components: many standard modules that are required in a measurement setup are not natively optimized for antenna measurements (e.g. low reflectivity or small dimensions) and were modified to lessen their impact on the result.
- Measurement procedure: various different measurement methods were implemented and conducted in order to understand occurring error sources and limit their impact on the results.
- Measurement accuracy: a thorough error analysis was conducted in order to quantify the achievable measurement accuracy for mm-wave antenna measurements.
- Post-processing: error sources that could not be removed through setup modifications or an optimized measurement procedure can still be reduced using post-processing algorithms that isolate the desired fields in order to filter unwanted sources.

The findings are structured as follows:

Chapter 2 provides an overview of the existing integrated antenna measurement setups starting with the first ones that made it possible to characterize wafer-probe-fed antennas. More recently, elaborate setups with higher positional accuracy, wider frequency range, and higher flexibility were developed

and are discussed in more detail. The second part of this chapter states the basis for an uncertainty analysis of a measurement setup. This method will be used to evaluate the performance of the developed setups for different measurement scenarios.

A detailed description of the measurement setup developed in this work is given in Chapter 3. The setup uses a robotic arm as a positioner for maximum spacial accuracy and flexibility. The robot and all other required components are described before the measurement procedure is illustrated. Two different alignment techniques between probing antenna and AUT are supported, one based on a laser range finder and the second on a far-field measurement of the AUT.

In addition, this chapter presents the supported measurement types that are used to analyze different antenna characteristics. Due to the flexibility of the robot, many different measurement types can be performed, which can be selected and adjusted by software rather than hardware modifications. Various optimizations were necessary to lessen the impact of different error sources and to ensure accurate results. Each error source and relevant counter measures are described in this chapter before measurement results of a horn and an integrated antenna at 160 GHz and 280 GHz are compared to simulation results in the last part of Chapter 3 in order to showcase the capabilities of the system.

After the setup was modified based on the initial horn and integrated antenna measurements, an in-depth uncertainty analysis was performed to assess the achievable measurement accuracy at 160 GHz and 280 GHz. Chapter 4 details all errors taken into consideration for the analysis and gives a detailed overview of their individual contributions towards the total measurement uncertainty for radiation pattern, directivity, and gain measurements.

While a high accuracy can be achieved using special wafer probes that are modified for antenna measurements, cheaper standard wafer probes interact with the radiated fields, which can cause heavy distortions in a measurement. The results thus often do not constitute a good representation of the actual antenna characteristics. In Chapter 5, two different post-processing algorithms are investigated and applied to integrated antenna measurements in order to filter unwanted distortions from standard probe measurement results. The two methods are the source reconstruction and the Mathematical Absorber Reflection Suppression (MARS) method and results are shown for active and passive integrated antenna measurements.

2 Measurement Setups and Accuracy

Different research institutions and companies have been developing antenna measurement setups to characterize antennas at mm-wave frequencies. This chapter provides an overview of the different approaches that were taken to tackle the challenges of mm-wave antenna measurements, as well as their respective strengths and limitations. The setups use a vector network analyzer (VNA) to generate and measure the signals that are sent by the T_X- and received by the R_X-antenna. As the VNAs usually do not support frequencies above 100 GHz, converter modules (i.e. mixer circuits) are used to extend their frequency range. A block diagram of a basic setup is shown in Fig. 2.1. The main difference between the setups that have been presented so far is the mechanical design of the actuator that positions the moving probe antenna and the design of the wafer chuck that holds the integrated AUT.

While the mechanical details of many setups have been described in detail and measurement results have been presented, the achievable measurement accuracy has yet to be discussed for integrated antenna measurements. In this chapter, the basis for an in-depth uncertainty analysis is given, which will be used in Chapter 4 to quantify the measurement uncertainty of the setup and assess its performance for far-field measurements of different antenna characteristics.

2.1 mm-Wave Antenna Measurements

As previously stated in Section 1.1, integrated antennas have to be static during a measurement to minimize wafer-probe movements and to minimize the risk of damaging the probe. After wafer probes were used for the first time to contact and characterize antennas [47], measurement setups were built for 1D radiation pattern measurements as shown in [48, 49] for an antenna at 25 GHz, which also facilitates the rotation of the probe antenna to measure the co- and cross-polarization. Subsequent setups used a similar mechanical design with an extendable rotating arm to ensure a far-field measurement distance [50] for frequencies up to 40 GHz, or for end-fire antennas [51] around 60 GHz.

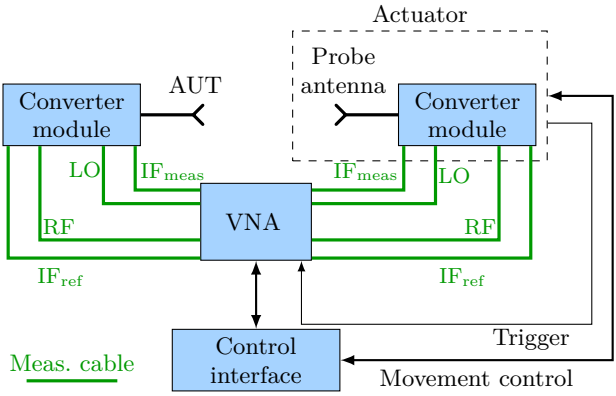

Fig. 2.1: Block diagram of a common measurement setup with moving probe antenna for integrated antenna measurements.

The first custom-made measurement setups for 2D-radiation pattern measurements were presented in [52–55]. They use two rotating arms that support measurements on almost an entire sphere around the AUT except for an area required for the waveguide connection between wafer probe and converter module. The systems operate at around 60 GHz, and in 2013 the setup presented in [55] was extended to operate at frequencies of up to 325 GHz. As the orientation of the probe antenna cannot be adjusted during a measurement, the co-polarization cannot be measured directly for multiple cuts, and the 3D-directivity has to be calculated from the measured fields in ϕ- and θ-direction.

While these setups support spherical measurements of integrated antennas for the first time, the positional accuracy is limited due to the custom-made mechanical setups, which can cause erroneous measurement results [56]. Mechanical vibrations also become more and more problematic with increasing frequency, which is why new systems with an improved mechanical setup that guarantee a better position accuracy have been demonstrated [57] and commercial setups have been presented [58]. Both of these setups use two rotational joints that support spherical measurements in a fixed distance. The sturdy mechanical setup ensures mechanical accuracy, unwanted reflections are reduced by the surrounding anechoic chambers.

The most recent setups use robotic arm positioning systems to achieve high accuracy with three [59] or six rotary joints [60–63]. The setup in [59] supports spherical measurements and a turning probe antenna to adjust the polarization during a measurement. For an improved phase measurement accuracy, a laser tracker is used to obtain the true measurement position, which can be used in post-processing to mitigate the effect of positional errors. The 6-degrees of freedom (DoF) robotic arm used in [61] was developed by the National Institute of Standards and Technology (NIST) and offers high flexibility in terms of supported measurement geometry. Measurement trajectories are mainly limited by the software that controls the movements of the robot. A hexapod is used to align the AUT as desired with respect to the axis of the measurement coordinate system.

The main focus of the setup is near-field measurements of electrically large antennas for frequencies of up to 500 GHz. Stringent mechanical requirements have to be met in order to guarantee positional error of less than $\lambda/16$, which is necessary for accurate near-field to far-field conversions and equates to a positional error of less than 40 µm at 500 GHz. Laser trackers are used to monitor and correct the position of the AUT and probe antenna in order to achieve sufficiently small phase errors. While the robotic arm performs movements in θ-direction, an azimuth rotator that holds the AUT carries out movements in ϕ-direction. With this azimuth rotator, the robot movements can be confined to the plane of maximum mobility, orthogonal to the plane where the movements are hampered by the base of the robot. Additionally, the weight distribution of the setup undergoes fewer shifts for single plane measurements compared to full sphere measurements, which facilitates the laser-based location correction. Therefore, using a rotator for AUT movements in ϕ-direction makes it possible to accurately cover large θ-ranges and thus a large portion of a spherical measurement surface. The same approach, however, cannot be used when measuring integrated antennas with wafer probes, as the fragility of the probes prohibits any AUT movements and therefore, the scanning in ϕ-direction has to be achieved through the robot rather than a rotating AUT-carrier.

The setup that was developed in this work was built at the same time as [61] and also uses a robotic 6-DoF arm as a positioner. As the focus was on integrated antenna measurements, all movements to cover the desired scanning geometry are performed by the robot with a static AUT. With AUT dimensions that are typically much smaller than 1 mm, most studies could be performed in the far field and therefore, the phase information and the positional accuracy

are less critical compared to the near-field measurements in [61]. However, post-processing algorithms that can be used to filter unwanted interference from the preliminary results as shown in Chapter 5 do need the phase information, which is why a high phase accuracy must still be achieved. A detailed description of the components, the supported measurement types, as well as the measurement procedure is given in Chapter 3.

2.2 Uncertainty Analysis

Due to random and systematic errors that occur during a measurement, the result is a random variable X_{meas} with a certain expected value $\mathrm{E}[X_{\mathrm{meas}}]$ and variance $\mathrm{Var}(X_{\mathrm{meas}})=\sigma^2$. The obtained results are only meaningful if they are reliable and close to the true values of the measured quantities. In order to assess the validity of a result, it is thus important to state the measurement accuracy that can be achieved [64, 65].

Precision and accuracy (also referred to as the 'trueness') can be used to quantify the performance of a measurement setup. The precision is a measure for the scattering of the result around $\mathrm{E}[X]$ caused by random errors and noise (reproducibility of a measurement). The lower the variance of the measurement result X_{meas}, the higher is the precision of the setup. The accuracy/trueness is a measure for systematic measurement errors that cause deviation of $\mathrm{E}[X]$ from the true value as shown in Fig. 2.2. The total error is the sum of the systematic and random simulation/measurement errors.

While accuracy analyses have been performed for lower frequency setups [66, 67], they have yet to be done for mm-wave measurements even though the quantification of the overall error is particularly important for measurements that are not well established and necessary to assess the validity of the results.

In order to determine the measurement accuracy, the expected deviation between $\mathrm{E}[X_{\mathrm{meas}}]$ and the true value of the measured quantity must be analyzed. Simulation results can be used as a reference value, if the total simulation error is sufficiently small. Simulations typically have a high precision, but just like measurement results, simulated quantities have a finite accuracy and can differ from the true value of the analyzed quantity. This is especially true for antenna measurements at mm-wave frequencies because material parameters that are not known with sufficient accuracy (e.g. the permittivity ε or the loss tangent δ) cause deviations between the simulation result and the true value. Fabrication tolerances are difficult to replicate in a simulation and cause further

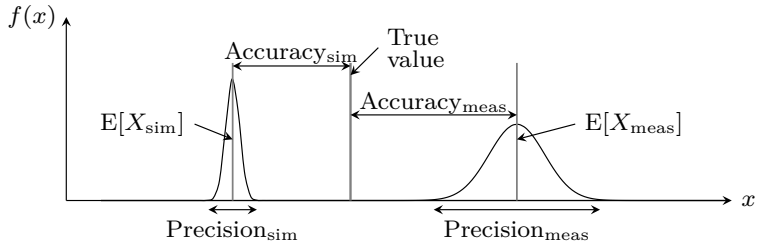

Fig. 2.2: Probability density function $f(x)$ of the obtained measurement/simulation result of a measurement quantity.

deviations and thus increase the systematic simulation error, which means that the expected value of the simulation $\text{E}[X_{\text{sim}}]$ does not necessarily coincide with the true value (see Fig. 2.2). For an uncertainty analysis, it is thus not sufficient to compare simulation and measurement as this can over- or underestimate the achievable measurement accuracy depending on the precision and trueness of the simulation.

For the determination of the overall measurement accuracy of the setup, the precision was increased by averaging a number of measurements such that the averaged result is sufficiently close to $\text{E}[X_{\text{meas}}]$. This makes it possible to investigate systematic errors independent from noise and other random errors to quantify the accuracy.

After all error sources that limit the accuracy have been identified, the sensitivity c_i of the result y (e.g. gain or radiation pattern) towards each error source x_i has to be determined [68]. Assuming a linear relation between one error source x_k and the measured quantity, the sensitivity c_k towards x_k can be calculated with

$$c_k = \frac{\mathrm{d}y(x_k)}{\mathrm{d}x_k}\,. \tag{2.2.1}$$

If the relation between error source and y is known, $\mathrm{d}y$ can be determined using propagation of error by calculating the influence of a changing error source $\mathrm{d}x_k$ on the result. This approach can be used, for example, to determine the sensitivity towards measurement distance uncertainties of gain measurements, since the impact of an erroneous distance can be calculated easily using the

free space attenuation. For more complex cases, propagation of error is often not applicable. In these cases, the sensitivity can be assessed by deliberately varying one error source (e.g. the antenna alignment or the measurement distance) by the maximum expected uncertainty of this error source $u(x_k)$. The erroneous measurement result obtained from this measurement y_{x_k} can then be compared to a reference measurement y_{ref}, where no deliberate error was introduced, in order to obtain the impact on the result

$$\Delta y(x_k) = \left| y_{x_k} - y_{\mathrm{ref}} \right| . \tag{2.2.2}$$

Multiple measurements have to be averaged for these analyses in order to make sure that dy is only caused by the introduced error and not due to random errors.

Once the sensitivity is determined for all identified error sources, the overall uncertainty budget $u_c(y)$ of the measurement can be calculated with

$$u_c(y) = \sqrt{\sum_{i=1}^{N} \left(c_i s_{x_i} \right)^2} \quad , \tag{2.2.3}$$

where N is the total number of error sources that are taken into account and s_{x_i} is the standard deviation of x_i. Usually a normal distribution for the error sources is assumed [69], in which case the standard deviation can be calculated as

$$s_{x_i} = \frac{1}{3} u(x_i) . \tag{2.2.4}$$

For other probability distributions, a different multiplication factor has to be chosen [70].

The extended uncertainty budget $U_c(y) = k u_c(y)$ can be adjusted to obtain a higher level of confidence. A coverage factor of $k = 2$ is commonly used, which corresponds to a 95 % confidence.

For some commonly used measurement procedures, standardized uncertainty analysis methods have been developed like the 18-term list of error sources composed by the NIST [71] that contains alignment, polarization, mismatch, truncation, and other error sources. Several studies on the sensitivity towards error sources and the accuracy of antenna measurement setups for planar [71, 72], spherical [73–76], and cylindrical [77,78] near-field measurements, as well as

for compact ranges [70,79] and far-field measurements [80] have been presented.

In [79] an uncertainty analysis is proposed that is based on 16 error terms at around 35 GHz. One of the main error sources that is unique to compact ranges are diffractions from the edges of the used reflectors and the amplitude taper of the quiet zone. The occurring errors for the different near-field measurement techniques are similar and mainly consist of mechanical inaccuracies, electrical errors, truncation, and unwanted reflections.

Despite the number of publications on the measurement uncertainty of antennas for various different setups and measurement quantities, the achievable accuracy for integrated mm-wave antenna measurements and measurement setups with static AUTs has not yet been addressed.

3 Robotic Antenna Measurement Setup

Due to the fragility of wafer probes, the AUT cannot be moved once the probe is contacted. Therefore, the probe antenna has to be moved around the AUT for radiation pattern measurements. This requires new mechanical solutions compared to rotating AUT measurement setups. Previous setups mostly use custom-made positioners that support spherical measurements in a fixed distance of the E_ϕ- or the E_θ-component of the radiated fields using rotating arms. While this makes it possible to measure the radiation pattern on a surface around the AUT, the flexibility of the setups is limited and field analyses are restricted to spherical geometries.

In this chapter, the realized setup and its components are explained in detail, as well as the measurement procedure and the supported measurement types. Furthermore, the changes that were made to some components are discussed and their effect on the measurement results are illustrated.

The AUTs used for these measurements were a standard gain horn (SGH) antenna with a gain of around 26 dBi and integrated antennas at 160 GHz and 280 GHz. The integrated antennas are scaled versions of the antenna presented in [83]. It uses a strip line to couple into a substrate integrated resonator, which then couples through a slot into a dielectric resonator, which is glued to the chip surface. A much higher efficiency can be achieved through the resonator compared to antennas without a superstrate. The simulated efficiency and gain of the antenna at 280 GHz are $\eta = 0.56$ and $G = 6.8$ dBi. A picture of this antenna is shown in Fig. 3.1.

3.1 Requirements

The stringent requirements of integrated antenna measurements demand a highly accurate and flexible measurement setup to minimize measurement errors and to support subsequent analyses like measurement uncertainty evaluations and interference mitigation in post-processing.

In order to meet these demands, the realized system features a 6-DoF robotic arm to move the probe antenna precisely on the desired measurement surface

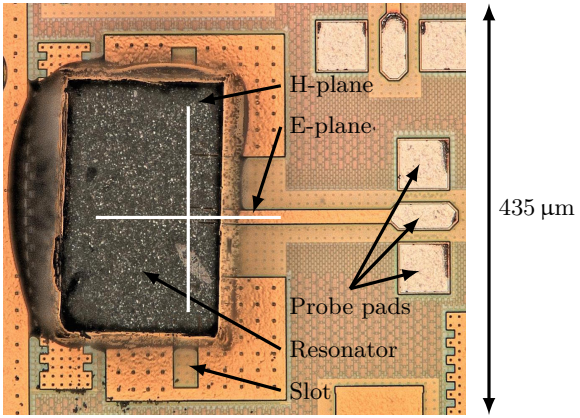

Fig. 3.1: Picture of the integrated antenna at 280 GHz [81], © 2016 IEEE.

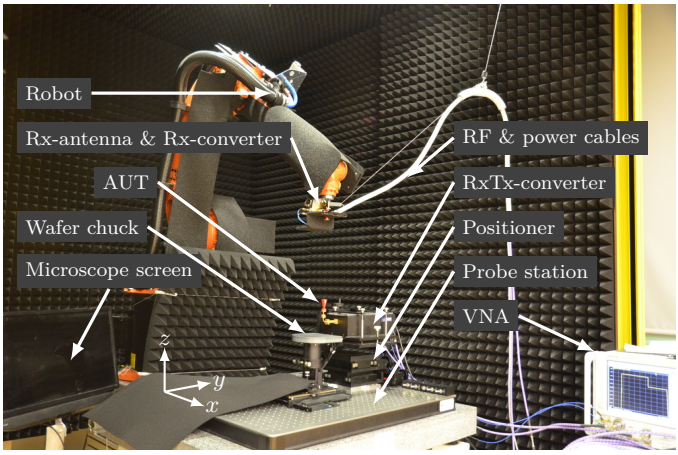

Fig. 3.2: Measurement setup with components [82], © 2017 IEEE.

around the AUT and to trigger the VNA at the specified measurement positions [84,85]. Due to the flexibility of the robot, the measurement trajectory is only limited by the software controlling its movements and by the mechanical limitations of the robotic arm used. Measurements settings can easily be adjusted to changing AUT sizes, orientations, positions, dimensions, and antenna separations through software rather than through mechanical setup modifications. This makes it possible to analyze different error sources independently and thus to quantify the total measurement uncertainty based on the individual contributions of different error sources.

As the combination of a probe station with a robotic arm to perform measurements around a static AUT presents a fundamentally new approach to integrated antenna measurements, and as the unique capabilities of the setup are essential for the subsequent chapters, a detailed description of the chosen components (see Fig. 3.2) will be given in this chapter. Software-adjustable measurements make it possible to align the antennas automatically and to cover a wide range of trajectories, which is why the measurement routine, alignment procedure, and supported measurement types are also presented.

3.2 Components

The main components that were used for the setup are the robotic arm to position the probe antenna at the desired locations, the probe station that holds the AUT and provides the required mechanics for probe contact, the VNA with the converter modules to perform the field measurements, and a control computer that runs a graphical user interface (GUI) through which the user can align the antennas, choose the required settings, and initiate measurements.

3.2.1 Robot Controller

The entire setup is run through a Python [86] user interface that allows to align AUT and probe antenna, choose the desired measurement type, adjust all required settings, initiate a measurement, and monitor its progress. During a measurement, it receives the trigger positions of the robot and saves them with their respective measurement results.

3.2.2 Robot

The robot offers high flexibility in terms of scanning geometry, measurement origin, and orientation. The positional accuracy is 350 µm, the repeatability 50 µm, and the supported scan geometries are only limited by the mechanical limitations of the robot. The coverable surface for 3D-scans heavily depends on the measurement distance [87]. Movements in $-x$-direction are obstructed by the robot base itself and mechanical limitations of the robot joints limit the movements in positive x-direction. For a measurement distance of 150 mm the maximum θ-value for a 3D-scan is over 90°, such that the complete upper hemisphere can be covered. If the distance is increased to 250 mm, the maximum θ-angle reduces to around $\pm 60°$. As 2D-scans can be performed in the less critical y-z-plane (see Fig. 3.2), they are only limited by the surface of the probe station—not by the joints of the robot.

The robot is controlled through an interrupt-driven program. Whenever a measurement is initiated through the GUI, the program enters a routine that carries out the respective measurement and triggers the VNA at the specified positions. In order to make sure the correct probe antenna dimensions are entered and to prevent collisions for short measurement distances, the robot moves the tip of the probe antenna to a spatial reference point within the measurement environment. If they do not align, false dimensions have been entered and the measurement can be stopped.

3.2.3 Measurement Equipment

The measurements are performed using a VNA. For frequencies above 60 GHz, converter modules for the desired frequency band are used to extend the frequency range of the network analyzer. The probe antenna that is mounted to the robotic arm is connected to an Rx module, which is why all measurements are performed with a transmitting AUT. Due to the movement of the robot, cables with a high amplitude and phase stability were chosen to connect the converter modules and a spring balancer that guides the cables between the Rx module and VNA ensures minimum stress and constant curvature of the cable during a measurement. For a planar near-field measurement on a 150 mm × 150 mm area, the measured phase error caused by cable movements is less than 3° at 160 GHz as shown in Fig. 3.3. The error was determined by measuring the phase of two identical back-to-back cables that were both run from the VNA to the robot using the default cable routing. The measurement was

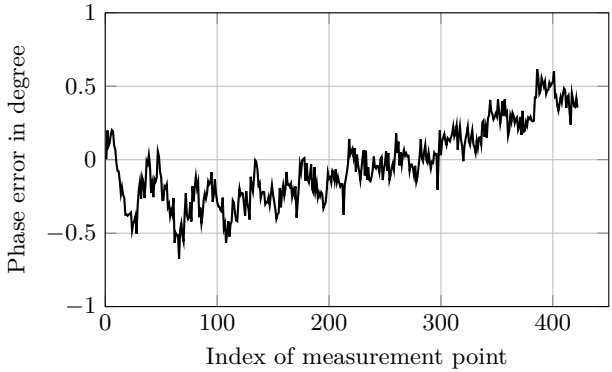

Fig. 3.3: Measured phase error at 160 GHz of the cable connecting the robot with the VNA.

conducted at the maximum frequency of 18 GHz that the cables carry when it is connected to the converter module at the robot during a regular measurement. The phase error at 18 GHz was then multiplied by 12, which is the multiplication factor of the converter module in the WR5.1 frequency band (140 GHz–220 GHz), to obtain the error at 160 GHz.

3.2.4 Probe Station

The probe station is required to contact integrated circuits (ICs). Positioners for the x-, y-, z-alignment and a microscope are used to precisely move the wafer probe and connect its tips with the probe pads on the chip surface. A chuck holds the IC and uses a vacuum pump to suck the chip to its surface to keep the chip in place as any relative movements between chip and probe could destroy the probe tips. Ground-signal-ground (GSG) probes are commonly used to contact integrated circuits as they offer good matching characteristics and the field distribution ensures minimal radiation from the probe tips when contacted.

The magnitude of probe radiation during an antenna measurement is difficult to determine as it heavily depends on the load. However, it can be expected to be relatively low compared to the AUT radiation, if the impedances of probe and antenna are well matched. A worst-case estimate can be obtained by a gain

measurement of an open-ended probe as shown in [88]. When not contacted to a chip the analyzed probe has a maximum gain of −12 dBi and should be even smaller when connected to a matched load. As the measured pattern has an end-fire characteristic and a much lower gain in the critical z-direction, it can be assumed that the probe radiation, when contacted to a matched antenna, only has a minor impact on measurements in the upper hemisphere.

The microscope is mounted on a rotating arm such that it can be easily moved away from the AUT before a measurement is initialized. The station has a modular setup that can be adjusted to the requirements of the current AUT. Two independent positioners can be removed or rearranged on the probe station to support in-line- and 90°-probing with two wafer probes. The chuck can also be repositioned or removed depending on the requirements of the respective setup.

3.3 Measurement Procedure and Alignment

As the AUT does not have a predefined position on the probe station and can change depending on its dimensions, feeding method, and radiation characteristics, the AUT location has to be specified before a measurement can be conducted.

A first alignment can be performed using a laser range finder that can be attached to the Rx module, which is mounted to the robot. The robot can then be moved through the GUI until the laser points down on the AUT, and the distance to the AUT can be measured using the range finder. Based on the current position of the robot, the offset between laser and robot, and the measured distance, the AUT location can be calculated. With a laser accuracy of around 2 mm and a diameter of the laser of over 4 mm, the AUT position is sufficiently accurate for amplitude measurements, but can be problematic for integrated antennas that are much smaller than the laser diameter, for high-gain antennas, where the transmitted amplitude changes quickly over the measurement position, and for post-processing algorithms that require the phase information.

A more accurate approach is to calculate the phase center of the AUT based on an initial far-field measurement as shown for a rotating AUT in [89, 90], where the offset between the rotation and phase center is critical. The flip-test method described in [91–93] is also used to determine the offset between phase center and rotational axes for measurement setups with rotating AUT. The method, however, has not been applied to 3D-measurements and requires two

measurements to determine the offset in one plane.

The phase center can also be determined based on the radiated fields on two orthogonal planes by analyzing the phase progression [94]. This procedure is applicable to static AUT measurements and only requires one scan per plane. A phase measurement around the phase center of an isotropic radiator on a spherical surface should theoretically result in a constant phase [38], whereas an out-of-center AUT will result in a phase progression along the spherical path. Offsets in x- and y-directions cause asymmetries in the measured phase, and offsets in z-direction lead to a symmetric cosine shape depending on the direction of the offset (see dashed plots in Fig. 3.4). As the phase center of a real antenna changes over frequency and viewing angle, the considered area has to be specified for a certain phase-center position.

The phase distribution around different measurement origins $\vec{o}\,'$ is determining by recalculating the phase in post-processing based on the path difference between the original measurement distance r and the distance between each measurement point $\vec{p}_i = (x_{p_i}, y_{p_i}, z_{p_i})$ and the moved origin

$$\Delta r = r - r' = r - |\vec{p}_i - \vec{o}\,'| \,. \tag{3.3.1}$$

Using the wave number k, this path difference can be expressed as a phase change of

$$\Delta\phi = k\Delta r \,. \tag{3.3.2}$$

The measured signal for a measurement around $\vec{o}\,'$ would therefore be

$$S'_{21} = S_{21}\mathrm{e}^{-\mathrm{j}\Delta\phi} \,. \tag{3.3.3}$$

The phase center can now be determined by minimizing the standard deviation of $\arg(S'_{21})$ with respect to $\vec{o}\,'$. The optimization of two spherical orthogonal measurements (e.g. one in the x-z-plane and one in the y-z-plane) yields the offset to the phase center in x- and z-direction (Δx, Δz_x) and in y- and z-direction (Δy, Δz_y) respectively.

The location of the phase center $\vec{c}$ can be calculated with

$$\vec{c} = \vec{o} + \left(\Delta x, \Delta y, \frac{\Delta z_x + \Delta z_y}{2}\right) \,. \tag{3.3.4}$$

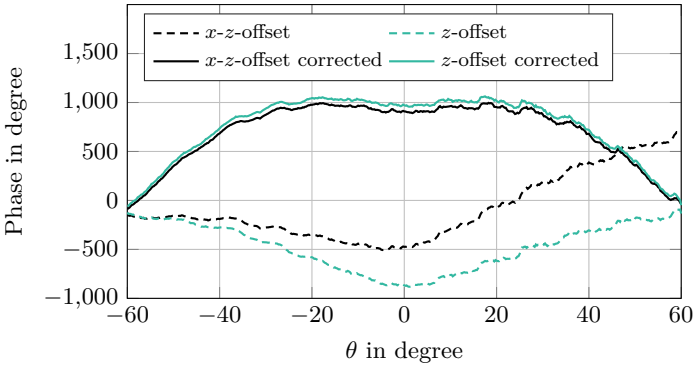

Fig. 3.4: Original and corrected phase of two measurements based on the calculated phase center [94], © 2017 IEEE.

As the phase center of an antenna depends on the plane [95], the average of Δz_x and Δz_y is used as the z-offset.

Figure 3.4 shows the corrected phase in the H-plane of two antenna measurements with different offsets. The criterion for the optimization of the phase was a minimum standard deviation of $\arg(S'_{21})$ within 40 dB of the main lobe. An offset of 5 mm in z-direction was used for both measurements, and an additional offset of $\Delta x = 1.5$ mm was applied in the x-z-offset measurement. The calculated phase centers based on the two measurement results were within 150 µm, and the calculated phases based on the respective phase centers show close agreement with a mean difference of less than 50° compared to over 400° for the original results. A second validation of the phase correction was done by comparing the corrected phase of an offset measurement to a measurement around the calculated phase center, which yielded a standard phase deviation of less than 30°.

Figure 3.5 depicts the phase of the 3D-x-z-offset measurement before and after correction. The x-offset shows itself clearly in the phase asymmetry in $\phi = 0°$-direction. This asymmetry can be corrected through the phase-center calculation and the maximum phase difference is reduced from more than 1,600° to less than 800°.

In order to assess the achievable accuracy with this antenna alignment method, the standard deviation of the phase-center position that was determined based

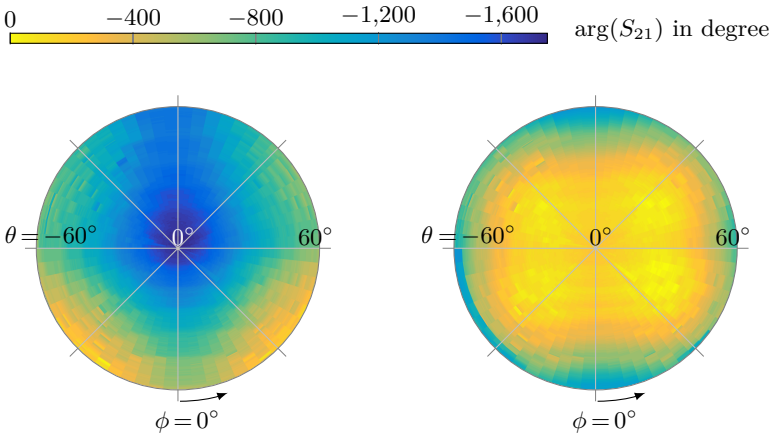

(a) x-z-offset.

(b) Corrected offset based on calculated phase center.

Fig. 3.5: Phase of a spherical horn antenna measurement at 280 GHz. x-offset $= 1.5$ mm, z-offset $= 5$ mm [94], ©2017 IEEE.

on multiple horn-antenna measurements to factor in the impact of different offsets in x-, y-, and z-direction and different angular evaluation regions ($\theta_{\max}$), was analyzed. The offsets were chosen between 1 mm and 5 mm and the evaluation region was chosen such that the pattern from 10 dB up to 50 dB within the main lobe was covered. The resulting standard deviation of the calculated phase center in x- and y-direction was 150 µm and 4.6 mm in z-direction. The comparably large standard deviation in z-direction is due to the fact that the phase center of horn antennas moves further into the antenna for larger θ-angles. For a fixed evaluation range of 40 dB within the main lobe, the standard deviation of the phase-center position was within 50 µm for all three dimensions.

Once the AUT position is specified, the measurement method can be selected. Multiple measurement procedures are supported like spherical, planar, extrapolation, polarization, and arbitrary measurements. Once all required settings for the respective measurement type are chosen, the measurement can be initiated through the GUI.

3.4 Supported Measurements

The setup supports various different measurement scenarios that are only limited by the software and the mechanical limitations of the robot itself. All measurements can be performed on the fly (OTF) or point to point (PTP). During an OTF-measurement the robot triggers the VNA at each measurement point without stopping. As the measurement is being conducted while the robot is still moving, this method is only suited for measurements with a short acquisition time at a moderate robot velocity. Multi-frequency measurements are carried out one frequency after another such that the measurement is conducted once for each frequency. This can increase the measurement time significantly, which is why OTF-measurements are mainly used when measuring a low number of different frequencies and for measurements with a large number of points, e.g. 3D-measurements.

In an PTP-measurement, the robot moves to a specified point and initiates the measurement after a predefined wait time to allow any vibrations to decay and ensure an accurate position during the measurement. Once the VNA has finished the measurement and sent the transmitted the data back to the control computer, the robot moves on to the next point. This procedure is mainly used for broadband measurements as all frequencies can be measured in one single run.

The currently supported measurement methods are:

- Spherical measurements
- Planar measurements
- Polarization scans
- Phase-center measurements
- Offset measurements
- Extrapolation measurements
- Custom measurements

Spherical scan trajectories can be specified with the minimum and maximum ϕ- and θ-angles and their respective angular increments, as depicted in Fig. 3.6a. For E_ϕ- and E_θ-measurements, the probe antenna maintains a constant χ-alignment, whereas the alignment is adjusted by rotating the probe

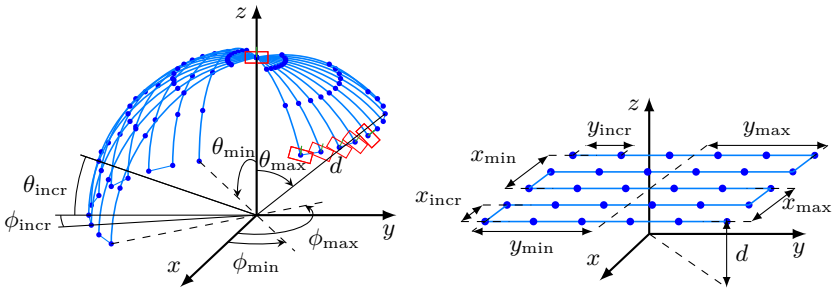

(a) Spherical scan trajectory. **(b)** Planar scan trajectory.

Fig. 3.6: Spherical and planer measurements [85], ©2017 IEEE.

antenna around its axis as indicated in Fig. 3.6a between two cuts for co- and cross-polarization measurements. Two orthogonal spherical far-field cuts can be used to determine the phase center of the AUT automatically as explained in Section 3.3. The calculated phase center can then be used as the measurement origin for subsequent measurements (e.g. to determine the radiation pattern C of an antenna), which is defined as the angle-dependent, normalized electric vector field $\mathbf{E}$ or magnetic vector field $\mathbf{H}$ in the far field

$$C(\phi,\theta) = \left.\frac{|\mathbf{E}(\mathbf{r})\,\mathrm{e}^{\mathrm{j}k_0 r}\,|}{|\mathbf{E}(\mathbf{r})\,\mathrm{e}^{\mathrm{j}k_0 r}\,|_{\max}}\right|_{r\to\infty} = \left.\frac{|\mathbf{H}(\mathbf{r})\,\mathrm{e}^{\mathrm{j}k_0 r}\,|}{|\mathbf{H}(\mathbf{r})\,\mathrm{e}^{\mathrm{j}k_0 r}\,|_{\max}}\right|_{r\to\infty} \tag{3.4.1}$$

with $\mathbf{r} = (r, \phi, \theta)$. A spherical measurement can also be used to determine the directivity D of an antenna, which is defined as the maximum power density $S_{\max}$ transmitted by an antenna into a certain direction compared to the power density radiated by an isotropic radiator S_{i}. S_{i} in turn can be determined by dividing the total radiated power P_{rad} by the surface of a sphere over which the power is distributed

$$D = \frac{S_{\max}}{S_{\mathrm{i}}} = \frac{4\pi r^2}{P_{\mathrm{rad}}} S_{\max}\,. \tag{3.4.2}$$

Equation (3.4.1) and the definition of the power density

$$S = \frac{\mathbf{E} \cdot \mathbf{H}}{2} = \frac{\mathbf{E}^2}{2Z_0} \tag{3.4.3}$$

can be used to calculate the total radiated power by integration over the power density on a spherical surface enclosing the AUT

$$\begin{aligned} P_{\mathrm{rad}} &= \int_{\phi=0}^{2\pi} \int_{\theta=0}^{\pi} S\, r^2 \sin\theta \,\mathrm{d}\theta \,\mathrm{d}\phi \\ &= r^2 \frac{\mathbf{E}_{\max}^2}{2Z_0} \int_{\phi=0}^{2\pi} \int_{\theta=0}^{\pi} \frac{\mathbf{E}^2}{\mathbf{E}_{\max}^2} \sin\theta \,\mathrm{d}\theta \,\mathrm{d}\phi \\ &= r^2 S_{\max} \int_{\phi=0}^{2\pi} \int_{\theta=0}^{\pi} C^2(\phi,\theta) \sin\theta \,\mathrm{d}\theta \,\mathrm{d}\phi \,. \end{aligned} \tag{3.4.4}$$

By plugging (3.4.4) into (3.4.2) the directivity can be calculated with

$$D = \frac{4\pi}{\int_{\phi=0}^{2\pi} \int_{\theta=0}^{\pi} C^2(\phi,\theta) \sin\theta \,\mathrm{d}\theta \,\mathrm{d}\phi} \,. \tag{3.4.5}$$

This means that the fields must be measured on a complete sphere around the AUT in order to determine the directivity. Areas that cannot be covered during a measurement therefore cause a truncation error in the measurement result.

Additionally, spherical offset measurements are supported where the phase center of the AUT is at an offset position in z-direction from the center of the measurement coordinate system. This measurement type is required for the MARS post-processing algorithm discussed in Chapter 5.

For planar near-field measurements the minimum and maximum values for the x- and y-position and their increments can be specified to define the scanning pattern. An exemplary near-field trajectory is shown in Fig. 3.6b.

The planar near-field to far-field transformation is based on the plane wave expansion, which is used to represents the measured E-field as a superposition of plane waves of different amplitude and direction [96]. The collection of plane waves required to represent the original arbitrary field is called the modal expansion. For a plane wave of known amplitude, phase, and direction at one point in space, the field at any other point can be determined, which means that the plane wave spectrum $\mathbf{f}(k_x, k_y)$ of a measured field can be used to

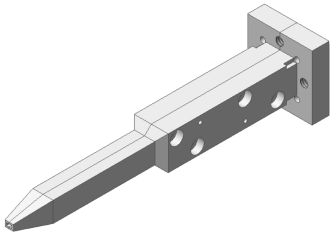

Fig. 3.7: Model of the fabricated near-field probe.

calculate the field at an arbitrary location in space [96]

$$\mathbf{E}(x,y,z) = \frac{1}{4\pi^2}\int_{-\infty}^{\infty}\int_{-\infty}^{\infty}\mathbf{f}(k_x,k_y)\,\mathrm{e}^{-\mathrm{j}\mathbf{k}\cdot\mathbf{r}}\,\mathrm{d}k_x\,\mathrm{d}k_y\,, \tag{3.4.6}$$

with the propagation factor $\mathbf{k} = k_x\hat{\mathbf{x}} + k_y\hat{\mathbf{y}} + k_z\hat{\mathbf{z}}$. The x- and y-components, $f_x(k_x,k_y)$ and $f_y(k_x,k_y)$, of the plane wave spectrum $\mathbf{f}(k_x,k_y)$ can be obtained through a 2D-Fourier transform of the field data $\mathbf{E}(x,\,y,\,z=0)$ measured in x- and y-direction (E_x,E_y) on a rectangular measurement plane with a width of a and a height of b at $z=0$ [96]:

$$f_x(k_x,k_y,z=0) = \int_{-b/2}^{+b/2}\int_{-a/2}^{+a/2}E_x(x,y,z=0)\,\mathrm{e}^{\mathrm{j}(k_x x+k_y y)}\,\mathrm{d}x\,\mathrm{d}y\,, \tag{3.4.7}$$

$$f_y(k_x,k_y,z=0) = \int_{-b/2}^{+b/2}\int_{-a/2}^{+a/2}E_y(x,y,z=0)\,\mathrm{e}^{\mathrm{j}(k_x x+k_y y)}\,\mathrm{d}x\,\mathrm{d}y\,. \tag{3.4.8}$$

For a near-field measurement on an $M\times N$ grid, the wavenumber spectrum points are given by

$$k_x = \frac{2\pi m}{M\Delta x}\,,\quad -\frac{M}{2}\le m\le\frac{M}{2}-1\,, \tag{3.4.9}$$

$$k_y = \frac{2\pi n}{N\Delta y}\,,\quad -\frac{N}{2}\le n\le\frac{N}{2}-1\,. \tag{3.4.10}$$

When sampling the near-field of the AUT, the Nyquist sampling theorem has to be satisfied and thus, the sample spacing Δx, Δy must be set to less than $\lambda/2$.

Knowing the x- and y-component of the plane wave spectrum, the spherical far-field radiation pattern at $k_x = k_1$ and $k_x = k_1$ can be approximated with [96]

$$\mathbf{E}(r,\theta,\phi) \approx \mathrm{j}\frac{k\,\mathrm{e}^{-\mathrm{j}kr}}{2\pi r}\left[\cos\theta\,\mathbf{f}(k_1 = k_0\sin\theta\cos\phi, k_2 = k_0\sin\theta\sin\phi)\right]. \quad (3.4.11)$$

Probe compensation can be applied to reduce the influence of the probing antenna on the far-field result, and many other techniques have been demonstrated to improve the accuracy or to reduce the number of required samples; however, since this work focuses on far-field measurements, these techniques are not discussed.

The open-ended waveguide probe shown in Fig. 3.7 was used in this work for the near-field measurements. Its small aperture yields a large beamwidth, which reduces the impact of the near-field probe on the far-field measurement result.

Polarization measurements can be performed by turning the probe antenna in χ-direction around its axis while it is facing down on the AUT as indicated in Fig. 3.8a. The results of a polarization scan can be used for an automatic co- and cross-polarization alignment for subsequent measurements. The cross-polarization angle χ_{cross} is obtained by a minimum search of the measured $|S_{21}(\chi)|$. The co-polarization angle χ_{co} is then calculated with $\chi_{\mathrm{co}} = \chi_{\mathrm{cross}} \pm 90°$, as the cross-polarization is usually a well-defined notch and can therefore be determined with higher accuracy.

The gain of an antenna can be determined with the gain comparison method, where the measurement result of the AUT is compared to a second antenna of known gain. Both antennas are measured in the desired frequency range at a distance which should satisfy the far-field condition for both antennas. By comparing the received signals of both measurements, the gain of the AUT can be determined using the formula

$$G_{\mathrm{AUT}}\big|_{\mathrm{dBi}} = |S_{21,\mathrm{AUT}}|\big|_{\mathrm{dB}} - |S_{21,\mathrm{ref}}|\big|_{\mathrm{dB}} + |G_{\mathrm{ref}}|\big|_{\mathrm{dBi}} - S_{21,\mathrm{con}}\big|_{\mathrm{dB}}. \quad (3.4.12)$$

The parameter $S_{21,\mathrm{con}}$ takes all connectors that differ between the two measurements into account. For the investigated integrated antennas, these connectors were a 90 °-waveguide bend ($S_{21,\mathrm{WGB}}$), which was used to connect the reference horn antenna, the wafer probe to contact the chip ($S_{21,\mathrm{probe}}$), and the

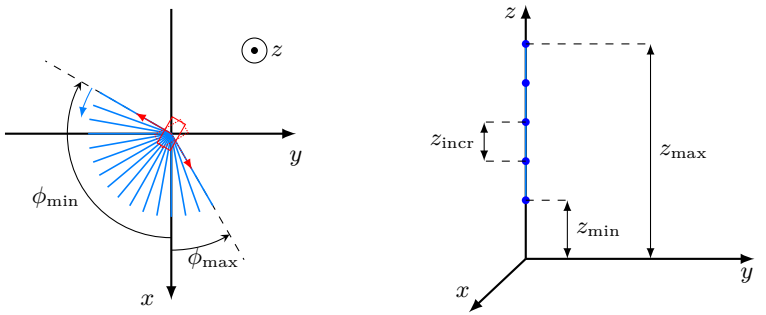

(a) The Rx-antenna rotates around the z-axis during a polarization measurement.

(b) Radiation measurement for different AUT-to-Rx-antenna separation distances.

Fig. 3.8: Polarization and extrapolation measurements [85], ©2017 IEEE.

microstrip line on the chip itself ($S_{21,\text{chip}}$):

$$S_{21,\text{con}}\big|_{\text{dB}} = |S_{21,\text{probe}}|\big|_{\text{dB}} + |S_{21,\text{chip}}|\big|_{\text{dB}} - |S_{21,\text{WGB}}|\big|_{\text{dB}} . \tag{3.4.13}$$

Extrapolation measurements [97, 98] can be conducted in order to analyze the impact of reflections that occur in the measurement environment. By measuring the radiated fields over the separation between AUT and probe antenna, as shown in Fig. 3.8b, the field can be measured and analyzed for different relative path lengths between the direct path and a reflected path.

The setup also supports custom measurements, where the desired path, orientation, velocity, acceleration, trigger, and wait time can be specified in a text file to support any desired measurement geometry only limited by the mechanical constraints of the robot.

3.5 Optimization

Many of the components that are used in the measurement setup were not designed and optimized for integrated antenna measurements and were originally intended for different purposes. Probe station, wafer probes, and the robotic arm are mainly made of metal and were designed for durability and sturdiness rather than reflectivity and size. These components disturb the measurement

results severely and can have a bigger influence on the result than the AUT itself. In order to reduce the impact of the measurement environment on the measured quantity, different components were modified to improve their performance.

3.5.1 Cable Routing

As the cables connecting the Rx module at the robot with the VNA must follow the movements of the robot, they have to endure considerable bending, twisting, and stretching during measurement. As a ϕ-rotator is not suitable for measurements with wafer probe, the AUT cannot be rotated under the robot to realize spherical scans. Therefore, the axis of the robot must cover a much wider angular range to support spherical scanning geometries compared to [61], where the robot movements are limited to one cut. In order to minimize cable movements for all supported measurement geometries, a detached cable routing that does not follow the geometry of the robot was chosen. For minimum stress the cables are suspended from the ceiling using a spring balancer. The cables are routed through a flexible tube that takes the stress from the cables and connectors by guiding the spring balancer and ensures a minimum bending radius during all measurements to avoid fractures of the dielectric and the conductors.

When performing a spherical E_ϕ- or E_θ-scan, the polarization χ is maintained throughout the entire measurement, which can cause the cables to wind up around the receiver module. The setup constantly monitors the current rotation of the Rx module at the robot and unwinds the cable by turning the module by 180° in the opposite direction when necessary. This rotation around 180° shifts the phase of the measurement signal by π, which has to be reversed for further processing.

3.5.2 Robot and Probe Station Reflections

The metallic surface of the robot presents a large reflective surface, which is especially problematic when the robot is facing down on the probe station as the radiation from the AUT can bounce back and forth between the two metallic surfaces, which causes interference and ripples on the measurement surface. These reflections have to be mitigated by covering the reflecting metallic surfaces with absorbers.

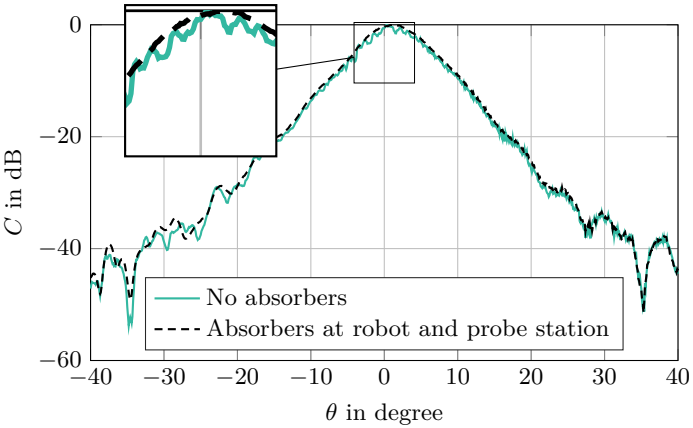

Fig. 3.9: Influence of absorbers on the measured antenna pattern [85], ©2017 IEEE.

Figure 3.9 shows a comparison between a measurement without any absorbers and a measurement with absorbers on the probe station and robot. Most ripples occur when the robot is directly over the AUT around $\theta = 0^\circ$ and when the robotic arm reaches over the AUT at angles $\theta > 15^\circ$, but can be successfully suppressed by the absorbers.

3.5.3 Movement Limitations

Due to mechanical limitation in the joints, the robot cannot reach arbitrary points with any orientation. For far-field measurements, this means that the robot cannot maintain its orientation beyond a certain maximum θ-angle. This can cause truncation errors (e.g. in directivity measurements), see (3.4.5).

The maximum angle increases with decreasing measurement distance. As the robot-to-AUT separation is the sum of the measurement distance and the receiver module length, the receiver module should be as compact as possible. Figure 3.10 compares the initial mount and an updated version with rotated receiver module and a 180°-waveguide bend, which reduces the distance between the robot and the aperture of the probe antenna by approximately 5 cm and therefore decreases the overall separation between robot and AUT for a certain

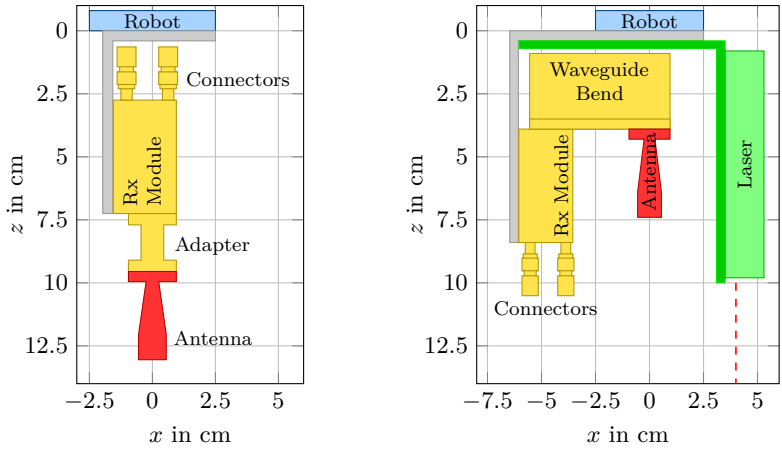

(a) Mounting structure without waveguide bend.

(b) Mounting structure with waveguide bend and removable laser range finder.

Fig. 3.10: Comparison of Rx module mounting structures [85], ©2017 IEEE.

measurement distance. Due to the small beamwidth of the horn antenna, the connectors of the Rx module in the new mount have a negligible impact on the measurement result. Additionally, the receiver unit can be covered with absorbers to avoid any interference during a measurement. Figure 3.10b also shows the removable laser range finder that is used for the antenna alignment.

3.5.4 Chuck Reflections

Most commercially available chucks are metallic for their durability and the precision that can be achieved in production, which is required to realize the small air channels for the vacuum suction that holds the chip carrier, on which the IC is glued, in place. Metal chucks, however, reflect parts of the radiated signals from the AUT, as shown in Fig. 3.11a, and cause ripples over the measurement angle in the radiation patterns and over frequency for gain measurements [81]. A second type of reflection is shown in Fig. 3.11b and is caused by radiation that is bouncing back and forth between the chuck and the metallic surface of the robot, similar to the reflections discussed in Section 3.5.2. [50] uses a cavity under the wafer with the AUT; however, this approach is not applicable

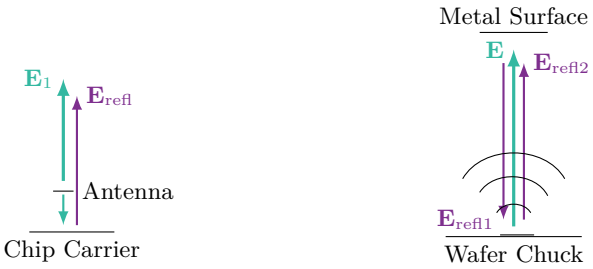

(a) Type 1 **(b)** Type 2

Fig. 3.11: Chuck reflections [81], ©2016 IEEE.

to single-chip measurements.

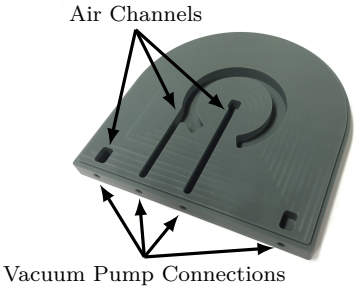

(a) Bottom part of the PVC chuck.

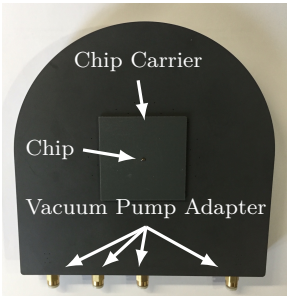

(b) PVC chuck with vacuum pump connections and chip.

Fig. 3.12: Fabricated non-metallic chuck with air channels for vacuum suction [81], ©2016 IEEE.

In order to minimize chuck reflections, a non-metallic chuck was designed. Polyvinyl chloride (PVC) was chosen as chuck material for its relatively low permittivity of $\varepsilon_r \approx 3$, durability, and workability. The chuck was made of two parts to support the air channels. Figure 3.12a shows the lower part with the milled channels; the finished chuck with chip carrier and IC is shown in Fig. 3.12b.

The reflectance of a PVC chuck for a perpendicular incident wave can be

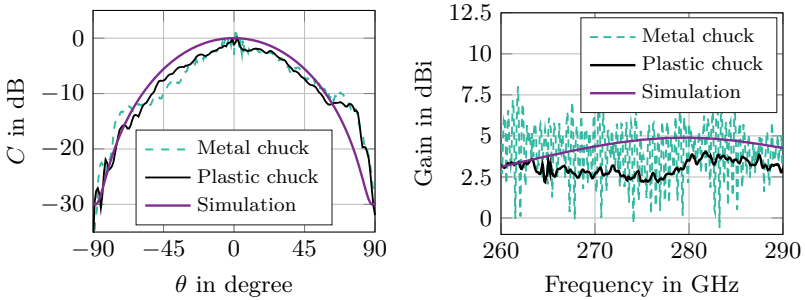

(a) Measurement of the integrated antenna in the H-plane.

(b) Gain measurement of the integrated antenna.

Fig. 3.13: Measurement of the integrated antenna at 280 GHz [81], ©2016 IEEE.

calculated using the Fresnel equations and the refractive indices $n_x = \sqrt{\varepsilon_x}$ of PVC and air

$$R = \frac{n_1 - n_2}{n_1 + n_2} \approx 7.2\%\,, \tag{3.5.1}$$

which is significantly lower compared to a metallic interface where almost the entire intensity is reflected.

Figures 3.13a and 3.13b show a comparison between metallic and PVC chuck measurement for radiation pattern and gain measurement respectively. It can be seen that the chuck reflections have a significant impact on the measurement result especially when measuring around the z-axis, perpendicular to the chuck surface, where the reflections are the strongest. The gain measurements were performed using the gain comparison method explained in Section 3.4. By using a less reflective chuck, the maximum ripple over the measured frequency was reduced from almost 7.5 dB to less than 1.5 dB.

3.6 Wafer-Probe Distortions

The wafer probe is the main source of reflection in passive integrated antenna measurements. Due to its relatively large size, the metallic surface, and the proximity to the AUT, wafer-probe distortions have a significant impact on the

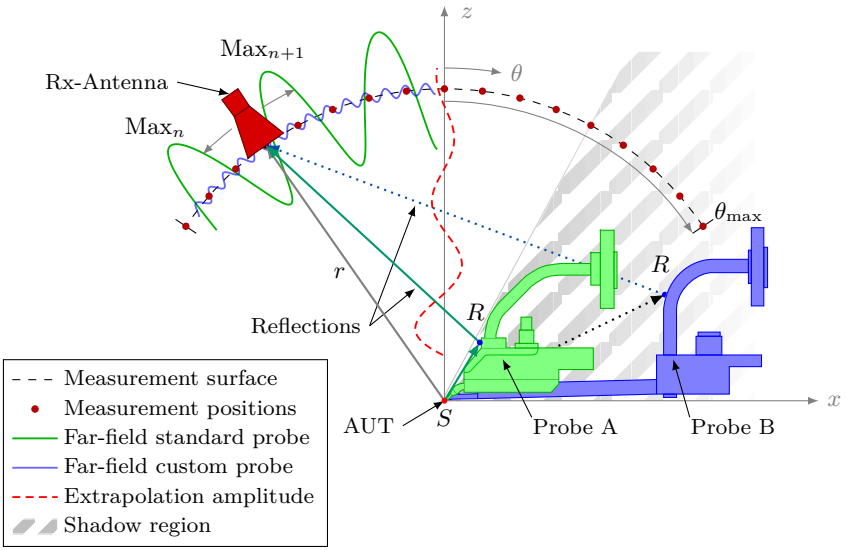

Fig. 3.14: Wafer-probe reflections interfere with the direct radiation from the AUT and cause ripples on the measurement surface with alternating minima and maxima depending on the θ-position. Similarly, the reflections cause interference for extrapolation measurements.

measurement result. The reflected signal superimposes with the desired signal from the AUT on the measurement surface and causes an interference pattern over the measurement angle with alternating minima and maxima depending on the relative phase between the two signals, as depicted in Fig. 3.14. This is especially critical in the contacting plane the probe is located in (x-z-plane in Fig 3.14), but also causes ripples in the orthogonal plane for small θ angles. With PCB technology, this problem can be reduced by using longer microstrip feeding lines [99] or by bending the PCB substrate in order to move the probe out of the measurement plane as shown in [57]. However, due to the limited size and mechanical characteristics of the chip, these approaches are not possible for integrated antennas. A second option to lessen wafer-probe disturbances

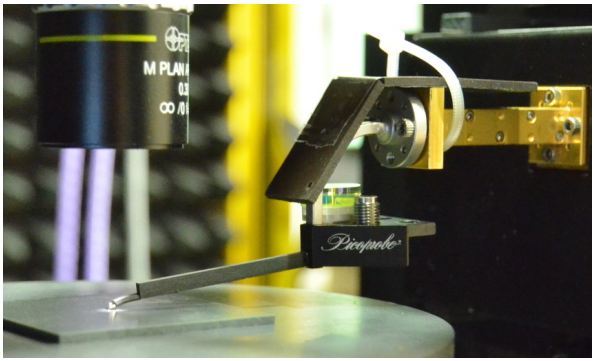

Fig. 3.15: Custom wafer probe optimized for integrated antenna measurements [85], © 2017 IEEE.

is to modify the probe design as shown in Fig. 3.14, where the length of the coaxial probe tip was increased for a maximum separation between probe and AUT, while still maintaining mechanical stability through an approximately 5 cm-long plastic support of the probe tip. A picture of the extended probe is shown in Fig. 3.15.

The extended probe tip not only increases the separation between the metallic body and the AUT, but also moves the probe into a less illuminated region of the radiation pattern for antennas that radiate in z-direction. This significantly reduces the disturbance on the measurement surface. Due to the longer path difference between direct and reflected path, the relative phase changes faster with θ, which is why the distance between two adjacent maxima decreases. The additional insertion loss of around 3 dB of the extended probe does not have a significant effect on the measurement results, as the measured signal levels are well above the noise floor.

A similar approach at 60 GHz was taken in [45, 99], where the probe body was moved underneath the AUT plane by modifying the shape of the probe tip. This approach, however, was not producible for higher frequencies as the smaller wavelengths pose even higher requirements for the fabrication of the probes.

The longer probe tip increases the probe losses, which is why the modified probe has around 2 dB higher attenuation compared to the standard probe

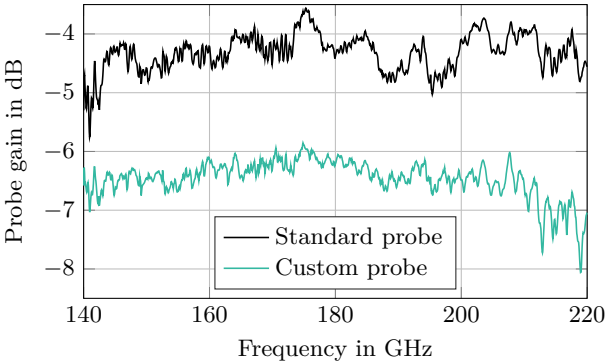

Fig. 3.16: Comparison of the probe attenuation.

shown in Fig. 3.16. The insertion loss of the probes was determined with a 3-short calibration technique, similar to the open-short-load deembedding presented in [101], but with three short standards of different lengths instead of the more difficult to fabricate load and not as well defined open standard.

The higher attenuation of the extended probe does not impair the measurement, as the signal level at the receiver is still sufficient when measuring with the extended probe. The new probe design, in contrast, drastically reduces probe reflections, which makes it possible to obtain meaningful measurements results, while the reflections of the standard probe overshadow the true measurement as shown in Fig. 3.17, where a spherical scan of an integrated antenna is shown for $\theta \leq 50^\circ$. Due to the probe distortions, the standard probe measurement bears no resemblance to the custom probe result and cannot be used for a meaningful characterization of the AUT. Apart from the ripples in the radiation pattern, the standard probe also blocks part of the radiated signal in the shadow of the probe in $\phi = 0^\circ$-direction where the signal declines (see Fig. 3.17b).

In order to determine the critical reflection centers on the probe body that cause the undesired distortions, the measured far-field pattern can be analyzed [102]. After determining the location of the maxima Max_i in the measured radiation pattern (see Fig. 3.14), all possible centers of reflection can be calculated for two adjacent maxima (Max_n, Max_{n+1}). For constructive interference in the far field, the direct path and the reflected path must be in phase on

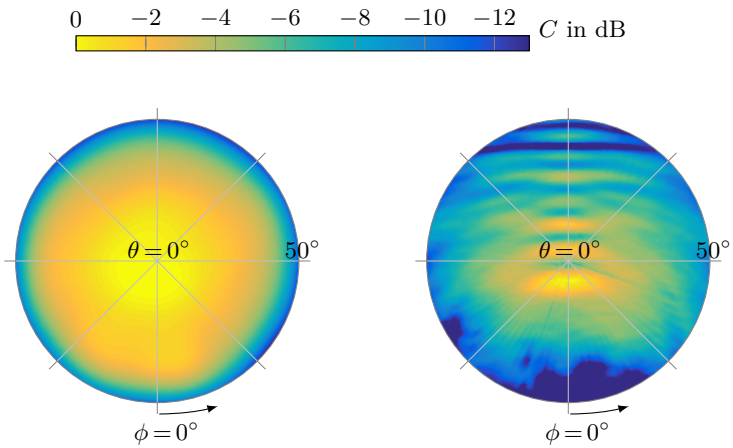

(a) Measurement with extended probe. **(b)** Measurement with standard probe.

Fig. 3.17: 3D-radiation pattern of the integrated antenna at 160 GHz. The probe is located at $\phi = 0°$ [100], ©2017 IEEE.

the measurement surface. As the phase is changed by π when the signal is reflected on the metallic surface, the path difference must be an uneven multiple of $\lambda_0/2$

$$\Delta_{\text{path}} = \left(\overline{SR} + \overline{R\text{Max}_i}\right) - \overline{S\text{Max}_i} = (2n-1)\lambda_0/2, \quad n \in \mathbb{Z}^+ . \tag{3.6.1}$$

Assuming that the measurement is conducted around the phase center of the AUT, the length of the direct path ($S \to \text{Max}_i$, Fig. 3.14) is constant. With the further assumption that the point of reflection does not depend on the measurement location, the distance between AUT and the point of reflection R remains constant. Therefore, the length of the reflected signal path l_i ($R \to \text{Max}_i$) must change by λ_0 between two adjacent maxima. For a reflection center position R as in Fig. 3.18, the distance is

$$l_i = \overline{R\text{Max}_i} = \sqrt{d_i^2 + e_i^2} = \sqrt{(b + r\sin\alpha_i)^2 + (r\cos\alpha_i - c)^2} . \tag{3.6.2}$$

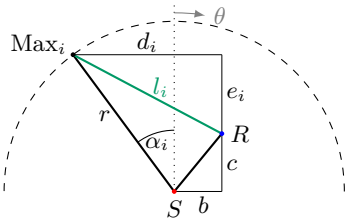

Fig. 3.18: Direct path and path reflected by the wafer probe.

As the path difference between two adjacent maxima must be λ_0, the condition for possible reflections centers is

$$|l_n - l_{n+1}| = \lambda_0 \,. \tag{3.6.3}$$

All possible reflection centers that fulfill this condition for a pair of maxima constitute a straight line, which intersects the probe surface at the actual point of reflection. If the analysis is performed for multiple pairs of maxima, as indicated in Fig. 3.19a, the obtained reflection lines cross each other where the reflection on the probe surface occurs. The result of this analysis is shown in Fig. 3.20a for a standard probe measurement and in 3.20b for a measurement with the custom probe of an integrated antenna at 160 GHz. As the center of reflection is closer to the AUT when measuring with the standard probe, the θ-dependency of the reflected path length is reduced and thus less maxima are observed. Therefore, less reflection lines can be calculated compared to the custom probe measurement. However, the location of the maxima is more difficult to determine for the custom probe measurement as noise and non-probe reflections have a bigger effect on the comparatively small ripples. Therefore, the reflection lines are spread over a larger area and thus, the uncertainty of the scattering center is higher compared to the standard probe. However, the results of both probes yield reasonable results with a center of reflection at the transition between waveguide connector and probe body for the standard probe and at the waveguide bend for the custom wafer probe. Similar results were obtained for a standard probe antenna measurement at 280 GHz, which also indicated a reflection center at the waveguide to probe body transition.

In order to verify these findings, a second approach to determine the reflection centers on the probe surface can be investigated. When performing an

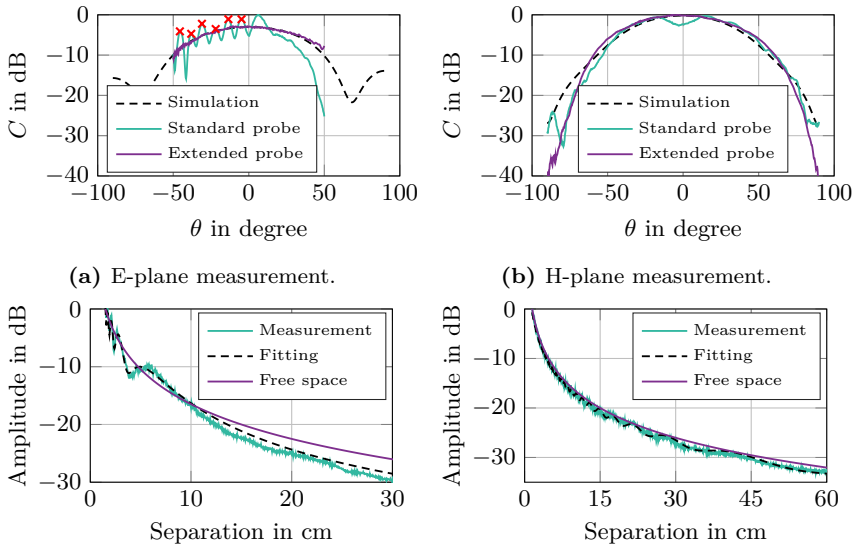

(a) E-plane measurement.

(b) H-plane measurement.

(c) Extrapolation standard probe.

(d) Extrapolation custom probe.

Fig. 3.19: Far-field and extrapolation measurements to determine the scattering location [102, 103], ©2017 IEEE.

extrapolation measurement, where the signal is measured over the separation between AUT and probe antenna, the expected outcome is that the amplitude of the received signal decreases according to the free-space path loss (FSPL) for increasing measurement distances [103]. In the presence of reflections, however, ripples can be observed due to the interference between direct and reflected radiation as shown in Figs. 3.19c and 3.19d for the standard and the custom probe respectively. The closer the reflections occur to the primary radiator, the smaller the antenna separation at which they manifest themselves. The amplitude of the measured signal can be calculated by adding the direct and the reflected signal, taking into account the phase difference between the two signals that is caused by the path difference

$$A_{\text{total}} = A_{\text{direct}} + A_{\text{reflected}} = \frac{\lambda_0}{4\pi l_{\text{direct}}} + \frac{\lambda_0 G_{\text{refl}}}{4\pi l_{\text{refl}}} \mathrm{e}^{\mathrm{j}k(l_{\text{direct}} - l_{\text{refl}})}, \quad (3.6.4)$$

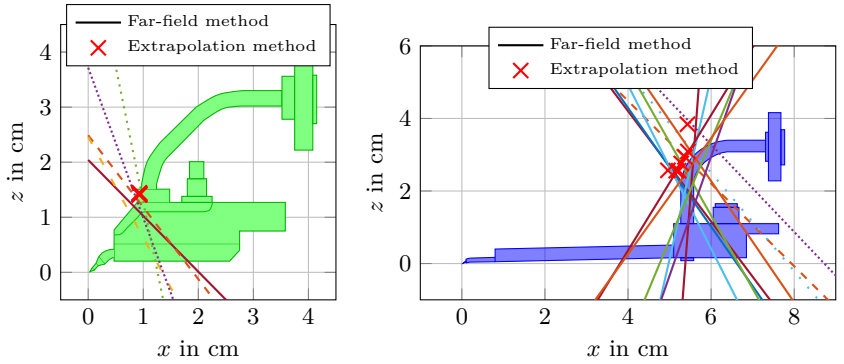

(a) Standard probe. **(b)** Extended probe.

Fig. 3.20: Determined scattering center locations for based on the measured far field and an extrapolation measurement [102,103], © 2017 IEEE.

where k is the wave number, and l_{direct} and l_{refl} are the direct and reflected path lengths. The gain of the reflected signal G_{refl} takes the higher attenuation of the longer reflected path into account, as well as the attenuation caused by the reflection on the non-ideal probe surface itself. l_{direct} corresponds to the separation between the two antennas. The reflected path length is

$$l_{\text{refl}}(x_{\text{refl}}, y_{\text{refl}}) = \sqrt{x_{\text{refl}}^2 + y_{\text{refl}}^2} + \sqrt{x_{\text{refl}}^2 + (l_{\text{direct}} - y_{\text{refl}})^2}\,, \tag{3.6.5}$$

where $(x_{\text{refl}}, y_{\text{refl}})$ is the position of the reflection for an AUT at $(0,0)$. The point of reflection can now be obtained by optimizing $(x_{\text{refl}}, y_{\text{refl}})$ such that the difference between the calculated total amplitude A_{total} and the measurement result is minimal. Apart from x_{refl} and y_{refl}, the optimization variables were G_{refl} and a normalization constant.

Figures. 3.19c and 3.19d show the calculated (fitted) curve for an evaluation region between 1 cm and 30 cm for the standard probe and between 1 cm and 60 cm for the extended probe. An open waveguide was used as a probe antenna instead of an SGH since the smaller aperture of the open waveguide made it possible to measure closer to the AUT without colliding with the wafer probe. The figures show that the close reflection center of the standard probe causes most distortions at relatively short measurement distances, whereas the

Tab. 3.1: Calculated scattering centers (all numbers in cm)

Standard probe		Extended probe	
Evaluation range	(x_{refl}, y_{refl})	Evaluation range	(x_{refl}, y_{refl})
1...20	(0.93, 1.41)	10...80	(5.28, 2.76)
1...30	(0.93, 1.41)	20...80	(5.37, 2.94)
1...40	(0.93, 1.41)	30...80	(5.44, 3.09)
1...50	(0.93, 1.42)	40...80	(5.16, 2.56)
1...60	(0.93, 1.43)	50...80	(5.43, 3.84)
1...70	(0.93, 1.44)	60...80	(5.22, 2.56)
1...80	(0.93, 1.44)	70...80	(4.96, 2.57)
Standard deviation:	(<0.1, <0.1)		(0.2, 0.5)

significant ripples only occur at distances larger than 10 cm for the custom wafer probe, because the point of reflection is further away from the AUT. As the point of reflection is obtained by reproducing the distorted signal for different (x_{refl}, y_{refl}), it is important to evaluate the regions that are most affected by the reflections. Therefore, the evaluation region should contain the first 10 cm for the standard probe and larger separation distances for the custom probe.

Table 3.1 shows the calculated reflection centers for both the standard and the extended probe for different evaluation centers. The results are also displayed in Figs. 3.20a and 3.20b. Similarly to the far-field method, the calculated reflection center position has larger deviations for the extended probe, because the characteristic ripples are less defined and therefore, the curve fitting is less accurate compared to the standard probe, where a curve can be fitted with high accuracy to the strong ripples that occur within the first 10 cm.

Despite the higher uncertainty for the extended probe, the results of both methods agree and clearly indicate a reflection center at the waveguide bend. The results obtained from the extrapolation measurement for the standard probe have a much smaller standard deviation and again point to a reflection center at the transition between waveguide to probe body and confirm the findings of the far-field method.

Besides using the custom probe to minimize probe reflections during the measurement, absorbers could be placed on the wafer probes; however, the thickness combined with the close proximity between standard probe and AUT

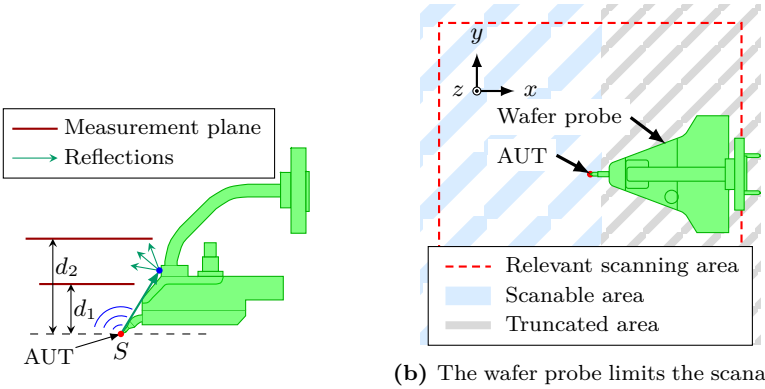

(a) Impact of probe scattering depending on the measurement distance.

(b) The wafer probe limits the scanable area for near-field scans [85], © 2017 IEEE.

Fig. 3.21: Near-field measurements reduce the impact of probe reflection, but the far-field results are distorted due to the signal truncation in area around the wafer probe.

cause more blockage by the absorber, which increases the shadow region behind the probe. Furthermore, with the additional thickness of the absorber on the standard probe, it is not possible to position the microscope above the AUT to monitor the contacting process.

Another way to reduce the impact of unwanted scattering is proposed in [104], where an integrated antenna is measured in the near field [105, 106]. If the measurement plane is close enough to the AUT, the reflected radiation of the wafer probe radiates past the covered measurement area and has less impact on the measurement result as shown in Fig. 3.21a, where the reflections radiate past the closer measurement plane at a distance d_1 and only affect the measurements taken at a larger distance d_2. This is true and observable in measurement results taken at different distances as shown in Fig. 3.22 for two near-field measurements taken at $d_1 = 15\,\text{mm}$ and $d_2 = 30\,\text{mm}$, where the 30 mm-measurement shows many more ripples around $y = 0\,\text{mm}$ compared to the measurement at d_1. However, the scanable area is extremely limited by the wafer probe and a large portion of the relevant scanning area cannot be reached (see Fig. 3.21b). While the near-field to far-field transformation yields a reasonable far-field result in the y-z-plane, the truncation of the near-field data in x-direction translates to

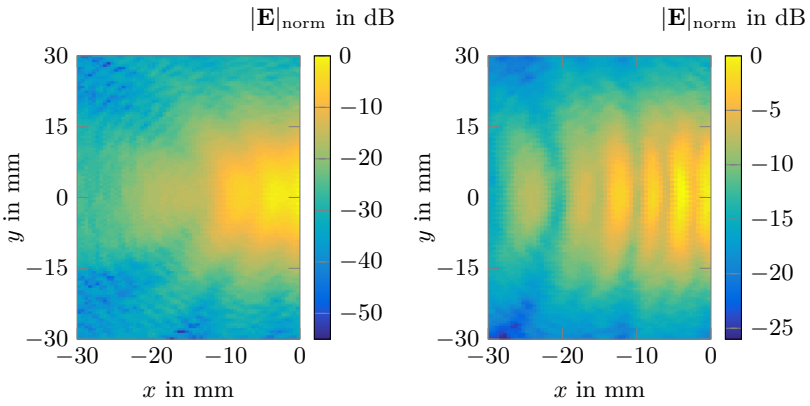

(a) 15 mm-measurement distance. **(b)** 30 mm-measurement distance.

Fig. 3.22: Impact of probe reflections on the near field at different measurement distances.

a significant error in the x-z-plane far-field results as shown in Fig. 3.23, which shows more ripples for the 30 mm-measurement for negative θ-angles. However, due to the signal truncation in positive x-direction, the pattern suffers strong distortions in probe direction and can only yield meaningful results in the plane orthogonal to the wafer probe. Therefore, the near-field measurement does not provide superior results compared to the far-field measurement, while posing much more stringent requirements on the measurement setup in terms of phase stability of the cables and positional accuracy of the robotic setup. This is why the focus in this work was put on far-field measurements; near-field optimization techniques were not investigated.

3.7 Comparison Measurement – Simulation

By modifying the critical components and ensuring minimal reflections from the measurement environment, many sources of measurement errors can be mitigated and accurate results can be obtained despite the high frequency. This section shows the results of a horn and of an integrated antenna measurement taken with the measurement setup after all of the modifications previously

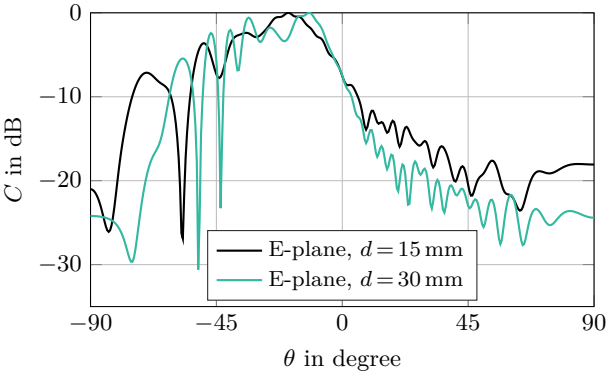

Fig. 3.23: Far-field result of a horn antenna near-field measurement at 280 GHz [85], © 2017 IEEE.

discussed were implemented. The remaining deviations between measurement and simulation results are not necessarily caused by measurement errors, but can also be due to fabrication inaccuracies and simulation errors, which cause deviations between the simulated and the true values of the fabricated antenna, as shown in Fig. 2.2 on page 15. Therefore, the comparison of measurement and simulation results cannot provide a reliable way to determine the measurement accuracy, but it can still be used as a validity check for measurement results to analyze the dynamic range of the setup, and to assess the impact of reflections.

The compared parameters are the radiation pattern, the polarization, and the gain of the antennas. For a minimum measurement time, all measurements were performed on the fly, which has a comparable accuracy with point-to-point measurements when using a sufficiently small θ-step and measurement speed [84].

3.7.1 Horn-Antenna Measurements

Figure 3.24 shows the measurement and simulation result of an SGH antenna. While the deviations for $|\theta| < 20^\circ$ are much smaller than 1 dB, they increase for larger θ-angles. The two main reasons are reflections in the measurement environment that cause the ripples visible for relative amplitudes below −50 dB and production tolerances of the fabricated antenna.

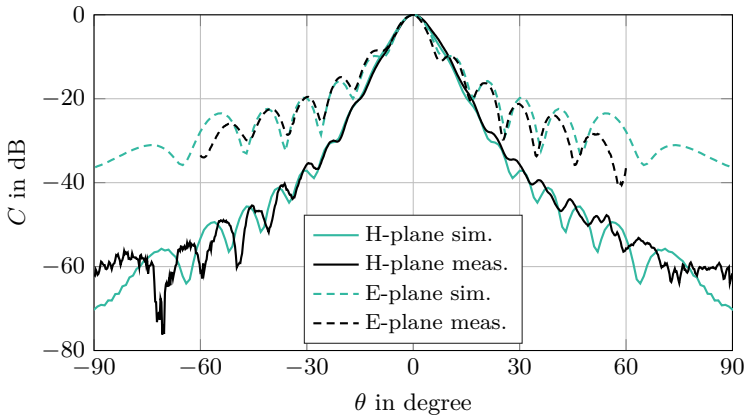

Fig. 3.24: Measurement of a horn antenna at 280 GHz.

Antenna measurements that cover a high dynamic range can suffer from distortions by reflected signals, because the amplitude of an attenuated reflected signal can be at a similar power level as the direct radiation. These reflections limit the dynamic range of the setup to around 50 dB, which is primarily a problem for measurements of highly directive antennas like aperture antennas, but it has less of an impact on the measurement results of integrated antennas.

The impact of production tolerances can be seen when comparing two measurements of the same antenna rotated by 180°. The results are a mirrored version of each other, which means that the asymmetries in the measurement result for $30^\circ < |\theta| < 60^\circ$ are caused by the antenna itself rather than the measurement setup.

The directivity of the antenna was calculated using (3.4.5) with a spherical measurement and was calculated to 26.3 dB, which matches the simulated value of 26.2 dB. The measurement was conducted up to a maximum angle of $\theta = 45^\circ$; the rest of the pattern was truncated. However, due to the high directivity of the antenna, the magnitude at larger angles is attenuated by at least 20 dB, which is why the scanning area is sufficient and angles $\theta > 45^\circ$ can be neglected.

The gain of the horn antenna G_{AUT} was determined using Friis equation as

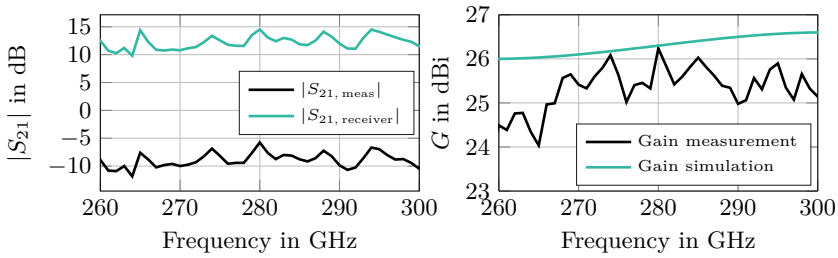

(a) Transmission Coefficient. **(b)** Gain.

Fig. 3.25: Determination of the absolute gain of a horn antenna at 280 GHz.

shown in [107]:

$$G_{\mathrm{AUT}} = \frac{P_{\mathrm{Rx}}}{P_{\mathrm{Tx}}} \left(\frac{4\pi R}{\lambda} \right)^2 \frac{1}{G_r}\,, \tag{3.7.1}$$

with the known receiver gain G_{Rx} and the measurement distance R. The ratio of $P_{\mathrm{Rx}}/P_{\mathrm{Tx}}$ can be determined through an S_{21} measurement. As the reference planes of an uncalibrated measurement are at the ports of the VNA, the measurement result contains the transmission coefficient of the transmitter, the desired ratio between the input power of the AUT and the output power of the receiving antenna $P_{\mathrm{Rx}}/P_{\mathrm{Tx}}$, and transmission coefficient of the receiver and of the required cables

$$|S_{21,\mathrm{meas}}|\big|_{\mathrm{dB}} = |S_{21,\mathrm{TR}}|\big|_{\mathrm{dB}} + 10\log_{10}\left(\frac{P_r}{P_t}\right) + |S_{21,\mathrm{Rx}}|\big|_{\mathrm{dB}}\,. \tag{3.7.2}$$

After a back-to-back measurement of transmitter and receiver, which yields $|S_{21,\mathrm{TR}}|\big|_{\mathrm{dB}} + |S_{21,\mathrm{Rx}}|\big|_{\mathrm{dB}}$, $P_{\mathrm{Rx}}/P_{\mathrm{Tx}}$ can be determined.

Figure 3.25 shows the uncalibrated values of $S_{21,\mathrm{meas}}$ as well as the gain of the receiver module. The receiver module exhibits non-linearities over the frequency with a ripple of up to 5 dB. The transmission coefficient $S_{21,\,\mathrm{meas}}$ of the antenna shows a similar progression over frequency; however, the ripples have a different amplitude, which causes a non-ideal calibration and ripples in the final gain measurement result shown in Fig. 3.25b. The different frequency response of the receiver module for the back-to-back and horn-antenna measure-

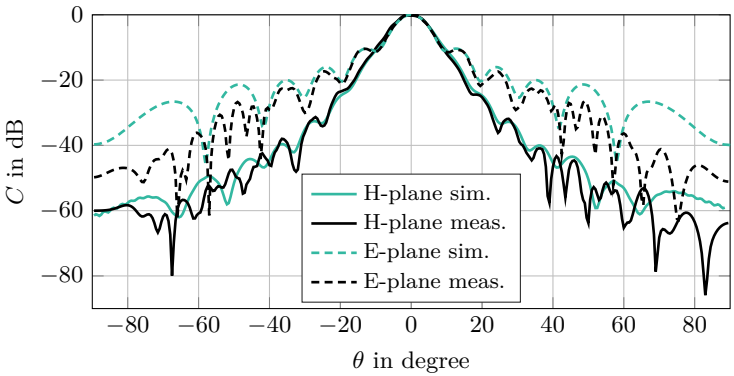

Fig. 3.26: Far-field antenna pattern of a horn antenna at 160 GHz after the near-field to far-field transformation.

ment could be caused by an input power dependency of the receiver module, which results in a flawed calibration. The final ripple in the gain measurement result is reduced to 2 dB through the calibration, but some of the peaks of the transfer function of the receiver module are still clearly visible, e.g. at 265 GHz, 275 GHz, and 280 GHz.

Near-field measurements are also supported by the robot measurement setup and the far-field result of a planar near-field scan is shown in Fig. 3.26. Due to the small aperture and large beamwidth, no probe correction was performed, which is—apart from phase errors caused by cable movements and positional inaccuracies—the main reason for the inaccurate measurement results at angles $|\theta| > 30°$. While the near field could be an interesting approach when measuring integrated antennas with lenses, it is of limited interest when characterizing on-chip antennas on their own, since the small Fraunhofer distance of these antennas facilitate direct far-field measurements.

The horn-antenna measurement results indicate that the setup is working as desired and meaningful measurement results can be obtained and show a dynamic range of approximately 50 dB.

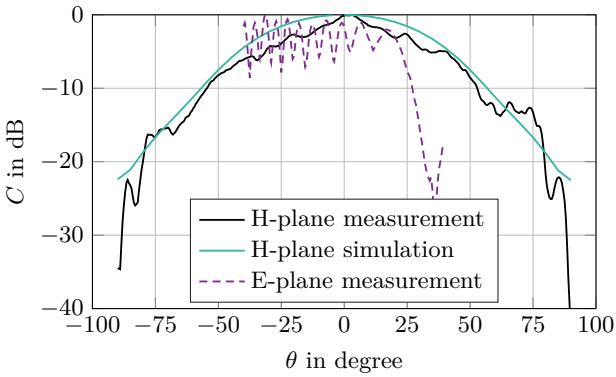

Fig. 3.27: Radiation pattern of an integrated antenna at 280 GHz [108], © 2017 IEEE.

3.7.2 Integrated Antenna Measurements

After the functionality of the measurement setup was confirmed using a horn antenna as AUT, the measurement results of integrated antenna at 160 GHz and 280 GHz were compared to simulation results in order to assess the performance when measuring on-chip antennas.

Figure 3.27 shows the result of a radiation pattern measured in the E- and H-plane. As explained in Section 3.6, the plane in contacting direction (E-plane) is heavily distorted by probe reflections and does not give a meaningful representation of the true radiation pattern of the integrated antenna. The ripples have a peak-to-peak amplitude of around 8 dB and the probe blocks part of the signal for positive θ-angles, causing the received signal to drop in the probe shadow.

These reflections, however, have only a limited effect on the orthogonal H-plane, which matches the simulation result with deviations of less than 2 dB. The signal drop at $|\theta| \approx 90^\circ$ is due to absorbers that were placed on the wafer chuck to minimize reflections. Depending on the relative amplitude between the direct signal and the signal reflected from the wafer probe, a notch or a peak can occur for angles around $\theta = 0^\circ$, which causes an offset due to a false normalization factor. In this case, the E-plane result shows that a maximum

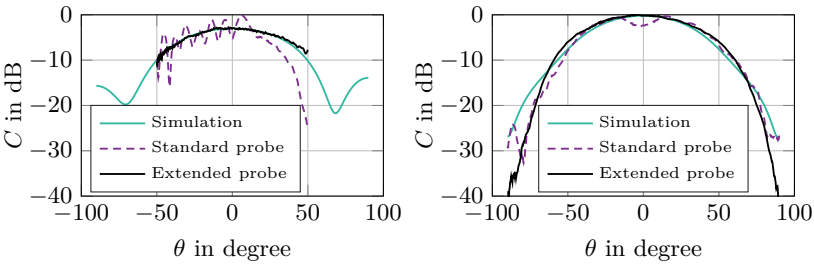

(a) E-plane measurement. **(b)** H-plane measurement.

Fig. 3.28: Simulation and measurement results of the integrated antenna at 160 GHz with the standard and extended probe [102], ©2016 IEEE.

occurs for $\theta \approx 0°$, which means that the normalization factor in the H-plane is too large, resulting in slightly lower values for the radiation pattern for angles $|\theta| < 50°$ compared to the simulation result.

The measurement result at 160 GHz in Fig. 3.28a shows a minimum in broadside direction; however, due to the wide beamwidth, a minimum has a smaller impact on the normalization factor, resulting in a slightly better alignment between measurement and simulation result, see Fig. 3.28b, compared to Fig. 3.27 at 280 GHz. Using the custom wafer probe presented in Section 3.6, much better results can be achieved both in the E-plane and in the H-plane, as shown in Fig. 3.28. The E-plane closely matches the simulation result with a maximum deviation of much smaller than 1 dB. The measurement was performed for $|\theta| < 50°$ in order to avoid collisions with the converter module feeding the wafer probe. In the H-plane, the measurement was performed on a half circle (180° -coverage). Due to the lower reflections from the custom probe, the notch around $\theta = 0°$, which occurred when measuring with the standard probe, was removed. The maximum deviation within $|\theta| < 60°$ is around 1 dB.

Using (3.4.5) on page 30, the directivity was calculated based on a 280 GHz measurement with the standard probe and two 160 GHz measurements with the standard and custom probe up to a maximum angle of $\theta = 50°$, in order to prevent collisions with the converter module connected to the wafer probe. Unlike the horn antenna discussed in Section 3.7.1, the integrated antenna has a lower directivity and radiates a significant amount of power towards the uncovered section of the measurement sphere with a radiation pattern that

Tab. 3.2: Measured directivity of integrated antennas at 160 GHz and 280 GHz. Ranges specify the lower and upper bounds for incomplete measurement surfaces.

Frequ. in GHz	Simulation in dBi	Standard probe in dBi	Extended probe in dBi
160	9.6	11.8–13.8	8.7–10.7
280	9.3	10.5–14.0	no probe available
Optimized coverage (extended probe)			
Frequ. in GHz	Simulation in dBi	Lower/upper bound in dBi	Substitution in dBi
160	9.6	9.0–9.8	9.6

decreases by less than 10 dB at $\theta = 50^\circ$. In order to assess the resulting truncation error, a lower and an upper bound for the directivity can be calculated by over-/underestimating the magnitude in the truncated measurement area ($0^\circ \leq \phi < 360^\circ$, $50^\circ < \theta \leq 90^\circ$). The integral in (3.4.5) can be underestimated by assuming zero radiation for angles $\theta > 50^\circ$, which yields an upper bound for the directivity D. A lower bound for D can be obtained by assuming that the radiation in the truncated area is equal to the radiation at the edge of the measurement sphere

$$\mathbf{E}(\phi, \theta > 50^\circ) = \mathbf{E}(\phi, \theta = 50^\circ)\,. \tag{3.7.3}$$

Table 3.2 shows the upper and lower bound for integrated antenna measurements at 160 GHz for the standard and extended probe and at 280 GHz for the standard probe only, as the extended probe could not be fabricated by the manufacturer in the WR3.1-frequency range. The standard probe measurements yield too large directivity values in both frequency ranges as both the lower and the upper bound are above the simulated directivity value. For the extended probe measurement, in contrast, the simulated directivity value lies within the range set by the upper and lower bound. This shows that the measurements obtained using the extended probe yield a much more accurate result than the standard wafer-probe measurements.

In order to mitigate the truncation error, the measurement area can be in-

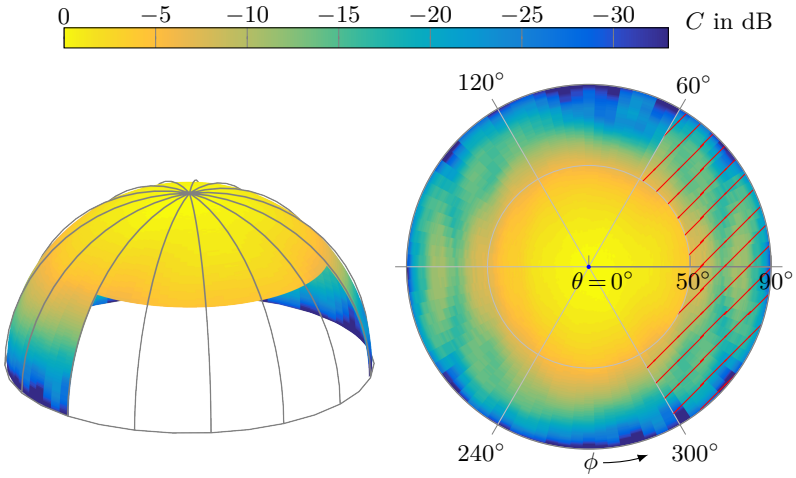

(a) Covered measurement area.

(b) Inserted measurement results from accessible area.

Fig. 3.29: Optimized coverage for directivity measurements [85], © 2017 IEEE.

creased in areas that are not obstructed by the measurement setup, while omitting the occupied regions. This makes it possible to cover the entire upper hemisphere except for a 40°×120°-section around the frequency converter module. The covered area is shown in Fig. 3.29a. With the larger measurement surface, the radiation pattern can be captured up to a relative amplitude of −30 dB for all angles $60° \leq \phi \leq 120°$. When calculating the upper and lower bound of the directivity based on these results, the range is decreased significantly with a lower and upper bound of 9.0 dBi and 9.8 dBi respectively (see optimized coverage in Table 3.2).

For an even better estimate of the directivity, the obstructed section of the measurement surface can be substituted with the mirrored results from the opposite side of the measurement surface, as indicated in Fig. 3.29b. A similar approach was taken in [53], but the inserted data was generated with simulation results rather than using the measurement results. Here the E-field in the

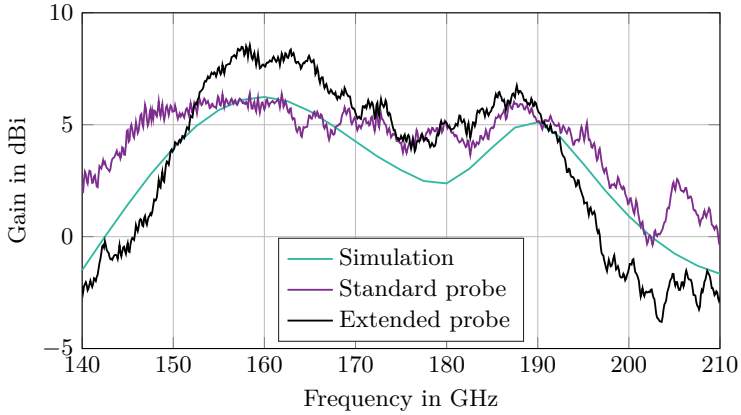

Fig. 3.30: Gain of the integrated antenna [102], © 2016 IEEE.

inaccessible hashed area was obtained by

$$\mathbf{E}(\phi_1, \theta_1) = \mathbf{E}(\phi_1 + 180°, \theta_1), \tag{3.7.4}$$

where $50° < \phi_1 \leq 90°$, $-60° < \theta_1 < 60°$. Using this directivity approximation, the measured directivity result is 9.6 dBi and matches the simulated value exactly.

The gain comparison method, as described in Section 3.4, was used to determine the AUT gain. The horn antenna of Section 3.7.1 was used as a reference antenna of known gain. The result of a measurement in the WR5.1-frequency band from 140 GHz to 210 GHz is shown in Fig. 3.30 for both waveguide probes. The simulated gain value of the antenna at 160 GHz is 6.2 dBi and the measurement results with the standard and extended probe are 5.8 dBi and 7.6 dBi respectively. While this seems to indicate that the standard probe yields better results, the observed lower gain value of the standard probe measurement stems from the destructive interference in $\theta = 0°$-direction between the direct and probe reflected radiation, as shown in Fig. 3.28a. Reasons for the approximately 2 dB difference between simulation and measurement are mainly inaccuracies of the material parameters in the simulation and inaccurate connector attenuation values $S_{21,\mathrm{con}}$ (see (3.4.13)). Gain measurements of the horn

reference antenna also indicate a lower gain than specified in the datasheet (see Fig. 3.25b) which would, according to (3.4.12), yield an increased gain value of the AUT. The reference horn-antenna gain parameter and the adapter attenuations are particularly critical as they add linearly into the measurement error.

The measurements conducted in the WR5.1- and WR3.4-bands show that probe reflections are a major error source for integrated antenna measurements with standard probes and even after the discussed measurement setup optimizations, only limited information about the AUT can be obtained. However, by using dedicated custom-made wafer probes, optimized for antenna measurements, the results can be improved significantly, which is especially noteworthy for pattern and directivity measurements, since the custom probe design makes it possible to obtain meaningful results in all planes of the upper hemisphere. Gain measurements also benefit from fewer probe reflections, because standard probe gain measurement results are dominated by the constructive and destructive superposition of direct and reflected signals.

4 Uncertainty

In Section 3.7 of the previous chapter, antenna measurements were compared to simulation in order to provide a first insight into the performance of the setup for different antenna types. The measurements were conducted after different components were altered and optimized for antenna measurements to guarantee results as accurate as possible. However, as explained in Section 2.2, comparing measurement to simulation can only be used to assess the performance of a measurement setup if the simulation results are sufficiently close to the real value of the measurand compared to the measurement, i.e. high simulation accuracy and precision. This condition cannot be considered to be met for integrated antenna simulations at mm-wave frequencies, as inaccurate material parameters, especially loss tangent and the permittivity, can cause false simulation results. Furthermore, fabrication tolerances (e.g. due to the manual mounting process of dielectric radiators) affect the radiation characteristics of the manufactured antennas.

Figure 4.1 shows a range of simulated radiation patterns (simulation spread) of the integrated antenna obtained by varying the position of the dielectric radiator in the simulation by $\pm 40\,\mu m$ in x- and y-direction. While the confidence that the fabricated antennas fall within this radiation pattern range is high, if all factors of uncertainty are taken into account, it shows that the performance of a measurement cannot be analyzed by comparing measurement and simulation results.

A more reliable quantification of the achievable measurement accuracy can be achieved through a measurement uncertainty analysis, as outlined in Section 2.2. The goal is to determine the effect of a certain error source on the desired measurement quantity by introducing deliberate errors in the measurement setup while monitoring the effect on the measurand. Once the sensibility of a quantity towards all possible error sources is determined, the expected standard deviation of each error source and the respective sensitivities can be used to determine the overall measurement uncertainty of a setup for a certain measurement quantity as per (2.2.3).

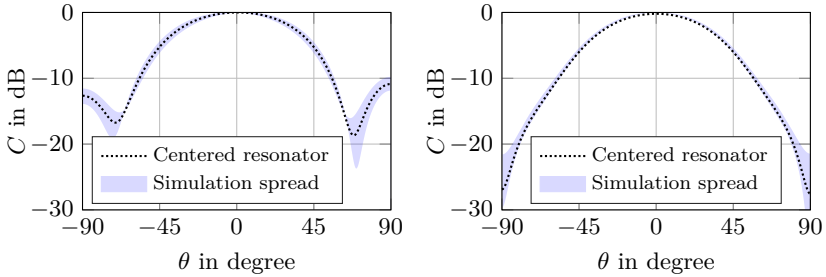

(a) E-plane. **(b)** H-plane.

Fig. 4.1: Simulated radiation pattern of an integrated antenna at 160 GHz. The highlighted area indicates the simulation results for different resonator positions (± 40 µm variation).

4.1 Error Sources

This analysis was performed for radiation pattern, directivity, and gain measurements with two different types of antennas – a high gain horn antenna and a lower gain integrated antenna – in order to get a comprehensive understanding independent of the AUT characteristics [108].

The first column in Table 4.1 lists all considered error sources divided into different categories, e.g. AUT-, reference antenna-, and alignment-related errors. AUT-related error sources were uncertainties of its position in x-, y-, and z-direction. If a laser range finder is used to determine the position of the AUT instead of the phase-center determination method described in Section 3.3, the offset between the alignment reference position on the AUT and the phase center presents another error source. Angular misalignment of the AUT (#5) affects all three measured quantities, while mismatches of the AUT only have minor impact on the gain result.

The probing antenna (#6–9) does not impact the accuracy as misalignments are canceled through normalization (radiation pattern and directivity) or through calibration (gain).

Uncertainties of the reference horn-antenna characteristics (#10–13) used for the gain comparison method as well as the adapters used to contact AUT and the reference antenna (#14) were taken into account for the overall gain

Tab. 4.1: Uncertainty budgets based on integrated antenna measurements at 160 GHz with the extended probe [85], ©2017 IEEE.

#	Source of Uncertainty x_i	Affected Measurements	Uncertainty ($\pm$) $u(x_i)$	Radiation Pattern c_i	Radiation Pattern s_{x_i}	Directivity c_i	Directivity s_{x_i}	Gain c_i	Gain s_{x_i}
1	AUT x-position	RP/D/G	1.5 mm	0.072 dB/mm	0.5 mm	0.002 dB/mm	0.5 mm	0.048 dB/mm	0.5 mm
2	AUT y-position	RP/D/G	1.5 mm	0.100 dB/mm	0.5 mm	0.004 dB/mm	0.5 mm	0.04 dB/mm	0.5 mm
3	AUT z-position	RP/D/G	2.0 mm	0.127 dB/mm	0.67 mm	0.001 dB/mm	0.67 mm	0.063 dB/mm	0.67 mm
4	AUT phase center	RP/D/G	1.0 mm	0.034 dB/mm	0.03 mm	0.001 dB/mm	0.03 mm	0.027 dB/mm	0.33 mm
5	AUT tilt	RP/D/G	0.125 °	0.2 dB/°	0.042 °	≈ 0	—	0.01 dB/°	≈ 0
6	AUT mismatch	G		—	—	—	—	≈ 0	—
7	Rx tilt	—	0.1 °	—	—	—	—	—	—
8	Rx length	—	100 µm	—	—	—	—	—	—
9	Rx phase center	—	5.0 mm	—	—	—	—	—	—
10	Rx Gain	—	0.2 dB	—	—	—	—	—	—
11	REF gain	G	0.4 dB	—	—	—	—	1	0.13 dB
12	REF tilt	G	0.125 °	—	—	—	—	1.37 dB/°	0.04 °
13	REF phase center	G	5.0 mm	—	—	—	—	0.015 dB/mm	2.33 mm
14	REF mismatch	G		—	—	—	—	≈ 0	—
15	Connectors	G	0.4 dB	—	—	—	—	1 dB/dB	0.53 dB
16	Trigger position	RP	350 µm					—	—
17	Cable flex	RP		1 dB/dB	0.04 dB	1 dB/dB	0.01 dB	—	—
18	Noise	RP/G						1 dB/dB	0.09 dB
19	AUT-Rx polarization	RP/D/G	0.1 °	—	≈ 0	—	≈ 0	—	≈ 0
20	Distance	G	350 µm	—	—	—	—	≈ 0	≈ 0
21	Reflections	RP/D/G		1 dB/dB	0.04 dB	1 dB/dB	0.02 dB	1 dB/dB	0.04 dB
22	ϕ resolution (4 °)	D		—	—	1 dB/dB	0.04 dB	—	—
23	θ resolution (0.5 °)	RP/D		≈ 0	—			—	—
24	Maximum-θ truncation	D		—	—	1 dB/dB	0.07 dB	—	—
25	VNA crosstalk	RP/D	112 nV_{rms}	—	≈ 0	—	≈ 0	—	≈ 0
26	Absorber placement	RP/D/G		—	≈ 0	—	≈ 0	—	≈ 0
27	Probe placement	RP/D/G		1 dB/dB	0.07 dB	—	≈ 0	—	≈ 0
28	Receiver non-linearity	RP/D/G		1 dB/dB	0.05 dB	1 dB/dB	0.07 dB	—	≈ 0
29	Long term effects	RP/D/G		1 dB/dB	0.03 dB	1 dB/dB	0.07 dB	1 dB/ dB	0.33
Expanded uncertainty $U_c(y)$ (95% confidence):				0.3 dB		0.3 dB		1.3 dB	

uncertainty calculation.

Random measurement errors like inaccurate trigger positions, amplitude changes caused by cable movements, and noise were determined by calculating the standard deviation between a set of reference measurements. This does not allow for finding the individual contributions of the random sources, which is why their combined contribution is shown in Table 4.1. The accuracy of the trigger position depends on the measurement speed of the robot for on-the-fly (OTF) measurements. For this analysis, the speed and acceleration were set such that the measurement time for a single cut was 1 min ($-90° < \theta < 90°$) and 60 min for a spherical directivity measurement ($-60 < \theta < 60°$, $0° < \phi < 180°$). For gain measurements, #16 and #17 can be neglected since the probing antenna remains static.

The AUT-Rx-polarization error (#18) can be neglected due to the automatic alignment process based on a polarization measurement. As long as the antenna separation fulfills the far-field condition, measurement distance errors do not have an effect on radiation pattern and directivity measurements. For gain measurements, an error in the measurement distance is negligible in comparison to the uncertainty of the phase center of the reference horn antenna and is therefore not taken into account.

The impact of multiple reflections was measured by comparing two sets of measurements taken at different distances with $\Delta d = \lambda_0/4$ as suggested in [66, 109]. It should be noted that this technique only works for far-away reflection centers, as a small distance change does not significantly change the relative path length between the direct and reflected paths, if the measurement is conducted in the far field of the antenna and the point of reflection is close to the AUT (see Fig. 3.19c for distances $d > 10\,\text{cm}$). Close reflections were avoided through setup modifications as shown in Section 3.5.

Due to the OTF-movement, the θ-resolution can be set sufficiently fine with a reasonable measurement time. The measurement time for directivity measurements, however, depends heavily on the chosen ϕ-resolution and #22 shows the impact of an increased ϕ-step. The sensitivity of the directivity was calculated by determining the maximum expected uncertainty using the difference between the best estimate of the directivity (see Section 3.7.2) and the calculated upper bound of a reference measurement D_{upB} in order to calculate the estimated maximum error. With (2.2.4) this yields

$$s_{\max_\theta} = \frac{1}{3}\left|D_{\text{best}} - D_{\text{upB}}\right| = 0.07\,\text{dB}\,. \tag{4.1.1}$$

Other error sources like #24, #25, and #27 were found to have a minor impact and were not considered for the final analysis. The receiver non-linearity was measured using a 20 dB attenuator at the input of the receiver module to test the setup for different receiver magnitudes.

4.2 Measurement Campaign

As described in Section 3.7, the results of 10 measurements were averaged in order to separate noise contributions from the analyzed error source in order to make sure the error is only caused by the introduced error. With 29 possible error sources and three quantities that were analyzed, this results in a considerable measurement effort, which is why the setup was adjusted to support multiple automated consecutive measurements. All error sources were checked for their relevance regarding the overall measurement error and propagation of error was used where possible. For each of the remaining error sources of each quantity, the measurement was initiated once and the robot performed the necessary repetitions for the averaging.

4.3 Achievable Accuracy

For the radiation pattern calculations, all angles within 30 dB of the main lobe were considered for the accuracy analysis to cover the dynamic range of an integrated antenna in the upper hemisphere. As depicted in Fig. 4.2a, which shows the standard deviation of 10 measurements, lower relative amplitudes suffer higher distortions, because they are more prone to errors from multiple reflections and from random sources (e.g. cable movements). The maximum deviations occur for relatively small amplitudes below -50 dB at magnitudes of minor importance for integrated antennas.

Figure 4.2b gives an exemplary result of a measurement to calculate the sensitivity of a measurand towards an error source. In this case the impact of an erroneous y-position of the AUT is analyzed for a radiation pattern measurement. A set of measurements with an AUT that was moved out of center in y-direction ($+\theta$) is compared to a set of reference measurements. The impact $\Delta C_{y\text{-pos}}$ on an erroneous y-position is calculated with

$$\Delta C_{y\text{-pos}} = \text{mean}(|C_{y\text{-offset}} - C_{\text{ref}}|) \tag{4.3.1}$$

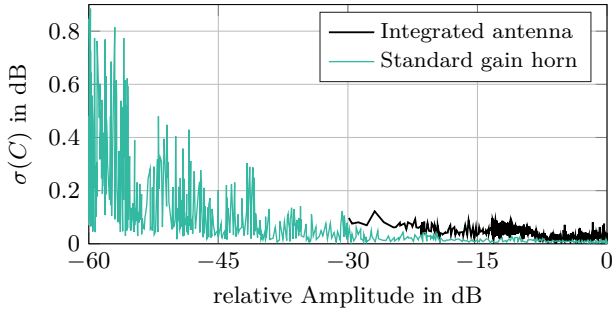

(a) Standard deviation of 10 radiation pattern measurements at 280 GHz [108], © 2016 IEEE.

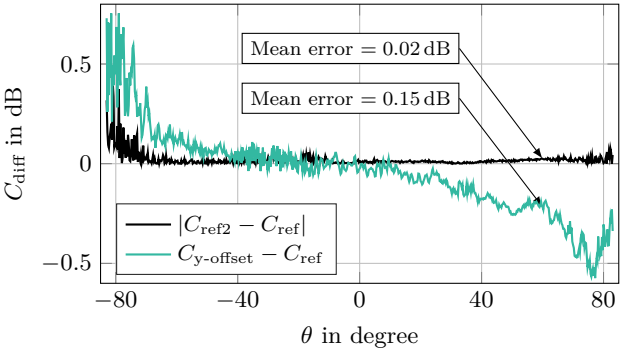

(b) Deviation between two sets of reference measurements and between a y-offset and reference measurement.

Fig. 4.2: Standard deviations for radiation pattern measurements.

and the sensitivity is

$$c_{y\text{-pos}} = \frac{\Delta C_{y\text{-pos}}}{\Delta y_{\text{pos}}} = \frac{0.15\,\text{dB}}{1.5\,\text{mm}} = 0.1\frac{\text{dB}}{\text{mm}}\,. \tag{4.3.2}$$

Similar approaches were taken for all relevant error sources to calculate the sensitivities and maximum expected deviations for an error source, as shown in Table 4.1, to determine the overall expected accuracy for radiation pattern,

Tab. 4.2: Achieved measurement accuracy at 160 GHz (95% confidence).

	Radiation pattern	Directivity	Gain
Horn antenna	0.2 dB	0.2 dB	1.3 dB
Integrated antenna	0.3 dB	0.3 dB	1.3 dB

directivity, and gain measurements. The table with the results of the horn-antenna analysis can be found in Appendix A on page 127. With a coverage factor of $k = 2$, the obtained results were 0.3 dB, 0.3 dB, and 1.3 dB for the radiation pattern, directivity, and gain for the integrated antenna and 0.2 dB, 0.2 dB, and 1.3 dB for the horn antenna, see Table 4.2. Performing absolute gain measurements is more challenging than relative measurements, which is why the gain measurement has the highest uncertainty.

Horn-antenna measurements at 280 GHz yielded similar results. As no extended wafer probe was available in the WR3.4-frequency range, integrated antenna measurements were only analyzed at 160 GHz, but based on the horn-antenna measurements, a comparable performance is expected once dedicated probes are available.

5 Reflection Suppression in Post-Processing

As stated [109], reflections are often the dominating source of measurement errors. Two different types of reflections can be distinguished [109]. The first type occurs between the AUT and the probing antenna and its supporting structure. It is caused by insufficient absorber placement, non-ideal absorber characteristics, and backscattering of the antennas itself. As the probing antenna moves during a measurement, the impact of these reflections is angle-dependent. Their influence on the measurement result increases with a lower measurement distance and can also be problematic for high-gain antennas, when a large portion of the radiated power is directed at the probing antenna within a certain angular range. Type I reflections were largely removed through absorbers around the receiving antenna and the plastic chuck presented in Section 3.5.4. The second kind of reflection occurs from the walls of the measurement chamber and static objects within the measurement environment. Especially affected are lower gain antennas and antennas with strong side-lobes. One example of these Type II reflections are the wafer-probe reflections discussed in Section 3.6.

It was shown in Chapter 4 that high accuracy measurements of integrated antennas are possible despite the challenging conditions at mm-wave frequencies. This was achieved by optimizing all components of the setup for antenna measurements, the crucial component being the wafer probe which, due to its close proximity to the AUT, caused severe distortions in all analyzed antenna parameters. By modifying the probe design such that the separation between the AUT and the metallic probe body is maximized, probe reflections were minimized, which made it possible to obtain useful results in all measurement planes—a major advancement for integrated antennas.

However, special, custom-made probe designs are expensive to fabricate and were not obtainable for all frequency bands of interest. Furthermore, many research facilities already have standard probes available, but no access to dedicated antenna measurement probes. It would thus be beneficial, if possible, to obtain meaningful results using standard wafer probes despite the occurring reflections on the probe body. As the reflections cannot be avoided during a measurement, the only solution is to separate the desired from the unwanted

radiation in post-processing, filter any undesired, reflected radiation, and compute the final result based on the direct radiation from the AUT.

5.1 Post-Processing Techniques

In order to suppress the unwanted scattered signals from the final data, direct and scattered fields must be separated. This separation can be performed in three different domains:

- Time domain filtering
- Spatial filtering
- Modal filtering

The filtering in time domain is commonly used to distinguish signals with different travel times between transmitter and receiver by transforming the measured frequency domain data into the time domain [110–112]. In the time domain, unwanted signal components, which can be identified by their respective travel times, can be filtered before a back transformation into the frequency domain of the filtered signal. This selective removal of signal components is called gating [113]. For a sufficient resolution in time domain, the signal must be measured over a large bandwidth in frequency domain. The response resolution determines the ability to separate two close sources [113]. The required resolution for an integrated antenna measurement can be determined using (3.6.5) and the calculated reflection centers on the probe according to Table 3.1 on page 46 as the difference between the direct signal path length l_{direct} and the wafer-probe reflected path l_{refl}

$$\Delta l = l_{\mathrm{refl}} - l_{\mathrm{direct}} = 5.3\,\mathrm{mm} \tag{5.1.1}$$

for a measurement distance of 30 cm. According to [113], this would require a measurement bandwidth of approximately 110 GHz which is, despite the high frequency, not achievable with an integrated antenna. As the necessary transformations can be realized with a Fourier transform, gating has a low computational effort and does not require any information about the geometry of the setup. However, due to the limited bandwidth of integrated antennas, this approach does not offer a high enough resolution to distinguish between direct

radiation and probe reflections and is mainly suited to eliminate reflections that occur at larger distances [96].

Spatial filtering can be performed based on a single frequency measurement of both tangential field components E_ϕ and E_θ on a spherical measurement surface Σ_M. According to the equivalence principle, an arbitrary wavefront can be synthesized from equivalent magnetic or electric current densities on a closed surface Σ_R within the exterior measurement surface Σ_M [114]. The goal is to compute the equivalent current densities on Σ_R that yields a field equal to the measured field on Σ_M to substitute the real antenna [115] the so-called Inverse Radiation Problem. Love's equivalence sets the fields within Σ_R to zero, which is advantageous in numerical stability and the near-field to far-field transformation performance [116]. If the reconstruction is precisely fitted to the surface of the AUT and its support structure, Love's sources match the extreme near field of the AUT [117]. This spatial mapping of sources to the measurement geometry makes it possible to use the obtained source distribution for antenna diagnostics [115, 118–120], i.e. to identify unwanted sources or malfunctioning antennas and to perform near-field to far-field transformations as the knowledge of the equivalent sources makes it possible to compute the radiated field at any arbitrary location outside Σ_R [121]. Due to the spatial mapping, this field transformation does not need to include all relevant sources that constitute the far field of the total structure. Unwanted sources and scatterers that are spatially separated from the AUT can be set to zero and neglected for the far-field computation in order to obtain the radiation pattern of the isolated AUT [122, 123].

The benefits of this approach are that it makes it possible to identify unwanted scattering centers on the measurement geometry and that it does not pose any constraints on the measurement geometry. However, a detailed geometrical model of the setup is required for the source reconstruction method (SRM) and the computational effort in terms of required computer memory and calculation time of the Inverse Radiation Problem scales disproportionally with the number of equations [117], which in turn depends on the number of mesh cells of the discretized setup and the number of measurement positions [122].

A second approach is the so-called Microwave Holography, which is mainly used for antenna diagnostics [124], but can also be used for spatial filtering [125]. Similar to using the 2D-Fourier Transformation to calculate the far field of an antenna based on a near-field measurement [126], the Fourier Transformation can be used to backpropagate a measured field to the aperture plane of an

antenna [127]. Due to the Fourier relation between sources and radiated fields, this technique is much simpler to implement and easier to compute than the SRM. The backpropagation, however, is limited to canonical surfaces (planar, spherical, and cylindrical) and is therefore not suitable for the post-processing of measurements with more complicated structures like wafer probes [117].

Modal filtering is based on modal expansion, which can be applied to transform radiated fields into orthogonal basis functions in order to get a modal representation of the original field data. Modal expansion is the standard approach for near-field to far-field transformations as the calculated mode coefficients can be used to calculate the field at any given point in space. Based on the physical dimensions of the radiator, a certain number of modes is required to represent the radiated fields in the mode domain. All additional modes can be attributed to sources outside the minimum radius sphere (MRS) of the AUT, which is a sphere of minimum radius completely surrounding the antenna. By using only modes of lower degree, which are caused by radiation inside the MRS, to compute the far field and thus neglecting other unwanted sources, the undistorted far field can be obtained.

The advantages of modal filtering are the comparatively low computational costs and the limited prior knowledge required to perform the filtering. The only information needed is the physical size of the antenna and the location of its phase center. Furthermore, reflections from moving objects (Type I reflections) can be filtered. On the other hand, modal filtering only provides limited information about the locations of the reflection centers and can only be applied to canonical measurement surfaces.

As the resolution of time domain filtering is not sufficient to filter probe reflections with the available bandwidth, this section focuses on modal and spatial filtering. The strengths of modal filtering are the low computational effort and the minimal information required about the setup, while the SRM has superior diagnostic capabilities.

5.2 Source Reconstruction

For a spherical coordinate system as in Fig. 5.1a with a source at $\mathbf{r}'$, the fields radiated by electric or magnetic current densities can be calculated with the electric or magnetic field integral equations [128]

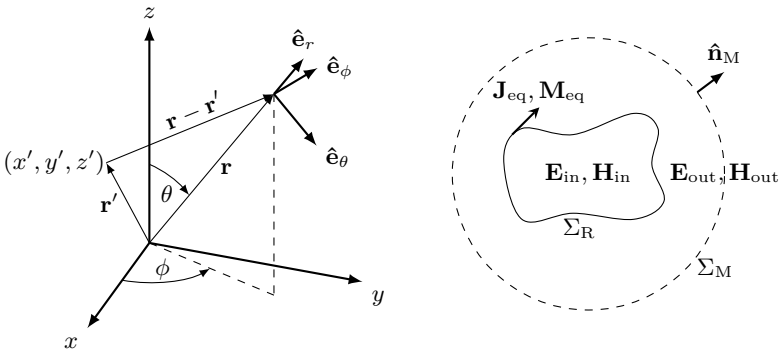

(a) Spherical coordinate system definitions with a source at $\mathbf{r}'$ and the observation point $\mathbf{r}$.

(b) Equivalence theorem.

Fig. 5.1: Field and angle definitions.

$$\mathbf{E}_\mathbf{J}(\mathbf{r}) = -\mathrm{j}k_0 \iint\limits_{S'} \left[\mathbf{J}_\mathrm{eq}(\mathbf{r}')g(\mathbf{r},\mathbf{r}') + \frac{1}{k_0^2} \nabla\cdot\nabla'\cdot\mathbf{J}_\mathrm{eq}(\mathbf{r}')g(\mathbf{r},\mathbf{r}') \right] \mathrm{d}S' \tag{5.2.1}$$

$$\mathbf{E}_\mathbf{M}(\mathbf{r}) = \iint\limits_{S'} \mathbf{M}_\mathrm{eq}(\mathbf{r}') \times \nabla g(\mathbf{r},\mathbf{r}')\mathrm{d}S' \,, \tag{5.2.2}$$

with the gradient ∇ (Nabla operator), the wave impedance in free space $\eta_0 = \sqrt{\mu_0/\varepsilon_0}$, and the Green's function for a three-dimensional radiator [128]

$$g(\mathbf{r},\mathbf{r}') = \frac{\mathrm{e}^{-\mathrm{j}k_0|\mathbf{r}-\mathbf{r}'|}}{4\pi\,|\mathbf{r}-\mathbf{r}'|} \,, \quad \mathbf{r} \notin \Sigma_R \,. \tag{5.2.3}$$

The resulting radiated field can be calculated as

$$\mathbf{E}(\mathbf{r}) = \mathbf{E}_\mathbf{J}(\mathbf{r}) + \mathbf{E}_\mathbf{M}(\mathbf{r}) \,. \tag{5.2.4}$$

The source reconstruction algorithm aims to solve the inverse scattering problem in order to calculate $\mathbf{J}_\mathrm{eq}$ and $\mathbf{M}_\mathrm{eq}$ based on the measurement of the tan-

gential field components on the measurement surface Σ_M. In accordance with the equivalence principle as shown in Fig. 5.1b, the currents are chosen such that the outside fields are identical to the field components radiated from the original sources

$$\mathbf{E}_\mathrm{out} = \mathbf{E}_\mathrm{out,orig}, \quad \mathbf{H}_\mathrm{out} = \mathbf{H}_\mathrm{out,orig}\,. \tag{5.2.5}$$

This means that the tangential component of the calculated E-field radiated from $\mathbf{J}_\mathrm{eq}$ and $\mathbf{M}_\mathrm{eq}$ according to (5.2.4) must match the measurement result on Σ_M

$$\hat{\mathbf{n}}_\mathrm{M} \times \mathbf{E}_\mathrm{meas}(\mathbf{r}) = \hat{\mathbf{n}}_\mathrm{M} \times \left[\mathbf{E}_\mathbf{J}(\mathbf{J}_\mathrm{eq}, \mathbf{r}) + \mathbf{E}_\mathbf{M}(\mathbf{M}_\mathrm{eq}, \mathbf{r})\right]\,, \quad \mathbf{r} \in \Sigma_\mathrm{M}\,, \tag{5.2.6}$$

with the outward normal $\hat{\mathbf{n}}_\mathrm{M}$ to Σ_M. By applying Love's equivalence, which enforces zero inner fields ($\mathbf{E}_\mathrm{in} = \mathbf{0}$, $\mathbf{H}_\mathrm{in} = \mathbf{0}$), current densities with the highest possible correlation to the true fields on Σ_R can be achieved [116, 129]. It requires the following boundary conditions on Σ_R [114, 123]:

$$\hat{\mathbf{n}}_\mathrm{R} \times \left[-\eta_0 \mathbf{E}_\mathbf{J}(\mathbf{J}_\mathrm{eq}^\mathrm{Love}, \mathbf{r}) + \mathbf{E}_\mathbf{M}(\mathbf{M}_\mathrm{eq}^\mathrm{Love}, \mathbf{r})\right] = -\frac{1}{2}\mathbf{M}_\mathrm{eq}^\mathrm{Love}(\mathbf{r}), \mathbf{r} \in \Sigma_\mathrm{R} \tag{5.2.7}$$

$$-\hat{\mathbf{n}}_\mathrm{R} \times \left[-\frac{1}{\eta_0}\mathbf{E}_\mathbf{J}(\mathbf{J}_\mathrm{eq}^\mathrm{Love}, \mathbf{r}) - \mathbf{E}_\mathbf{M}(\mathbf{M}_\mathrm{eq}^\mathrm{Love}, \mathbf{r})\right] = \frac{1}{2}\mathbf{J}_\mathrm{eq}^\mathrm{Love}(\mathbf{r})\,, \mathbf{r} \in \Sigma_\mathrm{R}\,. \tag{5.2.8}$$

In order to obtain a numerical solution for $\mathbf{J}_\mathrm{eq}$ and $\mathbf{M}_\mathrm{eq}$, the integral equation system of (5.2.6) and (5.2.1)–(5.2.4) must be discretized, which is commonly done using the method of moments (MoM) with Rao-Wilton-Glisson (RWG) basis functions [130] for the currents on each triangular facet on the discretized reconstruction surface Σ_R. This leads to a linear equation system in the form of

$$\begin{bmatrix} E_\theta \\ E_\phi \end{bmatrix} = \begin{bmatrix} Z_{\theta,J_u} & Z_{\theta,J_v} & Z_{\theta,M_u} & Z_{\theta,M_v} \\ Z_{\phi,J_u} & Z_{\phi,J_v} & Z_{\phi,M_u} & Z_{\phi,M_v} \end{bmatrix} \cdot \begin{bmatrix} J_u \\ J_v \\ M_u \\ M_v \end{bmatrix}\,. \tag{5.2.9}$$

As in [117], the normal field component E_r was neglected as it decays much faster compared to the tangential field components. This means that only the two tangential field components E_ϕ and E_θ have to be measured.

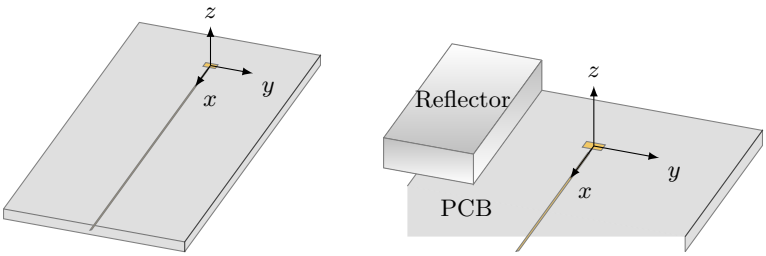

(a) Sole antenna without reflector.

(b) AUT with metallic reflector to introduce reflections. The reflector rests on the surface of the PCB.

Fig. 5.2: Patch antenna under test at 120 GHz.

Different approaches to solve this system of equations and some numerical solvers are explained in [117].

First attempts on using source reconstruction and spatial filtering for wafer-probe-fed antenna measurements have been made in [131] at 60 GHz, but detailed analysis on the reconstruction capabilities in measurement regions that are blocked by the setup (e.g. the shadow region behind the probe), locating the main scatter region, and determining the achievable reflection suppression have not yet been made.

One of the biggest challenges of the source reconstruction approach at mm-wave frequencies is matching the Σ_R with the true measurement geometry both with respect to the dimensions of the reconstruction surface and its alignment.

The procedure was therefore first tested with an easy-to-model structure at 120 GHz. The radiator was a patch antenna with patch dimensions of $a = 0.7\,\mathrm{mm}$ and $b = 1.15\,\mathrm{mm}$, supported by a rectangular metal plate as depicted in Fig. 5.2a. A waveguide-to-microstrip transition was used to feed the antenna.

The measurement was conducted on a spherical measurement surface with a maximum θ-angle of 70° and a ϕ and θ increment of 2° and 0.25°, respectively. Two consecutive measurements were taken in order to probe the E_ϕ- and the E_θ-fields. The source reconstruction calculation in this work were performed using the Microwave Vision Group (MVG) INSIGHT software.

Figure 5.3 shows the reconstructed equivalent currents on the structure based

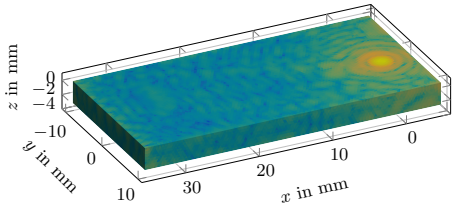

(a) Fine mesh with approximately 28,000 mesh cells.

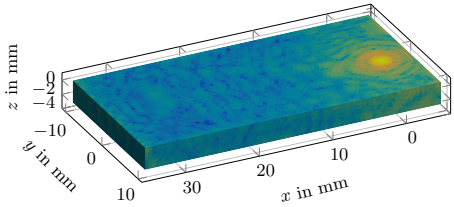

(b) Coarse mesh with approximately 12,000 mesh cells.

Fig. 5.3: Reconstructed equivalent surface currents based on a 120 GHz measurement of a patch antenna.

on the measured field components at 120 GHz. The origin of the measurement was in the center of the patch antenna as shown in Fig. 5.2b. Figure 5.3a was calculated with around 28,000 mesh cells, while Fig. 5.3b contains approximately 12,000 mesh cells and a maximum mesh cell edge length of $\lambda_0/4$. Both calculations yielded a similar surface current distribution that clearly show the maximum current on the patch radiator. Due to the increased number of mesh cells, the computation time in case of the finer mesh was increased to 2 hours and 5 minutes compared to 41 minutes with the larger mesh size. Given the small difference in the calculated current distribution and the significant computational time increase, the larger mesh was chosen for subsequent measurements.

The far-field measurement result, as well as the reconstructed far-field result, are shown in Fig. 5.4a. The agreement between the measured and reconstructed fields in both the E-plane and in the H-plane shows that the surface current calculation yields correct results and that the dimensions of the reconstruction surface Σ_R, as well as its position and orientation within the reconstruction

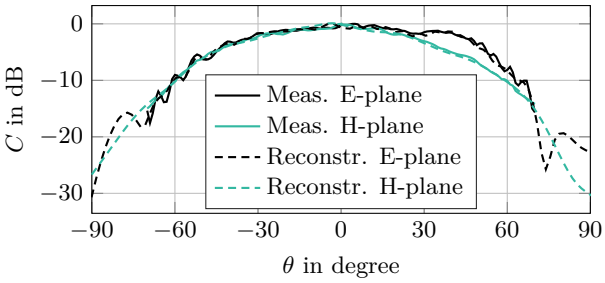

(a) Without reflector.

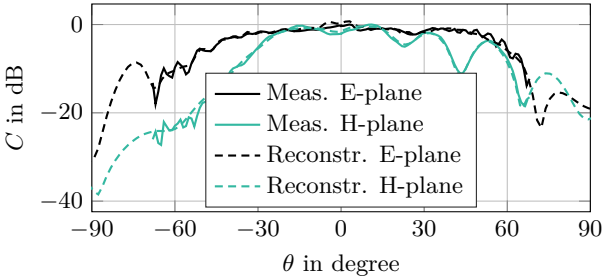

(b) Reflector next to the antenna.

Fig. 5.4: Measured and reconstructed far field of the patch antenna at 120 GHz.

coordinate system, matches the geometry and position of the physical antenna in the measurement coordinate system.

In order to assess the filter capabilities, a rectangular metal piece was placed next to the patch resonator to introduce a reflection center close to the AUT as shown in Fig. 5.2b. The measurement result in the E-plane and H-plane of the antenna are shown in Fig. 5.4b. While the E-plane has only minor ripples with an amplitude of around 1 dB and deviates by less than 1 dB from the measurement without a metal reflector, the reflector does introduce significant ripples for positive θ-angles in the H-plane. Due to blockage behind the reflector, the signal level drops for $\theta < -30°$.

The calculated surface currents are displayed in Fig. 5.5a. Despite the

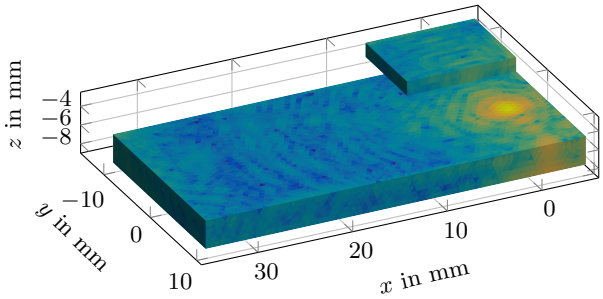

(a) Calculated surface currents.

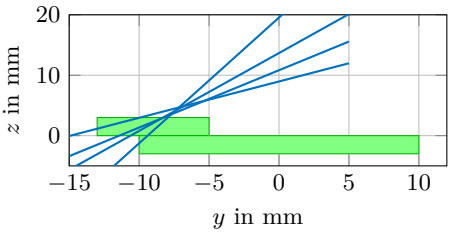

(b) Calculated reflection center based on the minima and maxima of the measured far-field pattern.

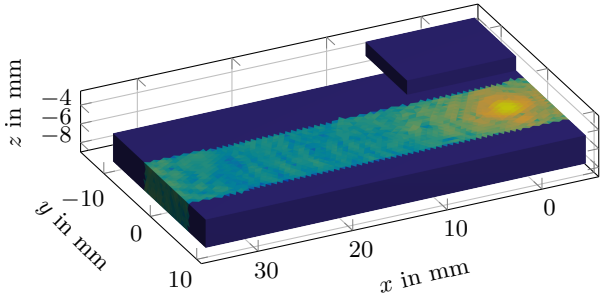

(c) Filtered surface currents to obtain undistorted far-field results.

Fig. 5.5: Surface currents and reflection points of the patch antenna at 120 GHz with a reflector on the PCB to introduce distortions.

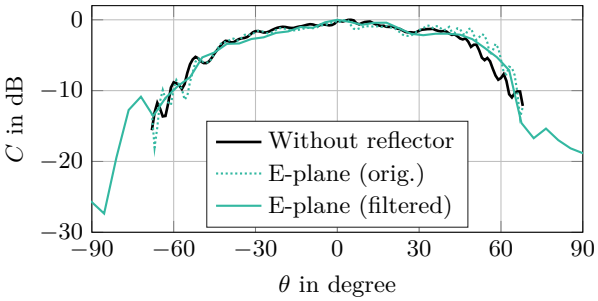

(a) E-plane.

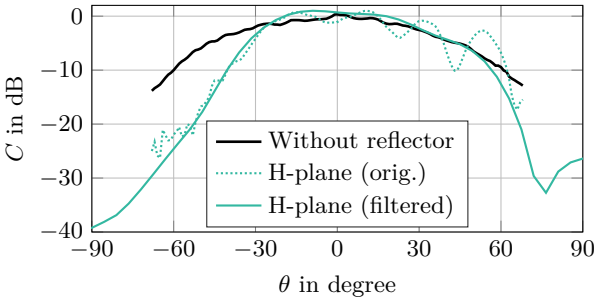

(b) H-plane.

Fig. 5.6: Measured and filtered far field of the patch antenna at 120 GHz.

matching reconstructed and measured far fields, the reconstructed currents do not show the expected increased current density at the reflector, but displays slightly higher surface currents at the carrier edge in positive y-direction. When calculating the point of reflection based on the minima and maxima location (see Section 3.6), however, the intersection of possible reflection centers indicates a reflection center on the surface of the metallic cube placed next to the antenna as shown in Fig. 5.5b. Possible reasons for the inaccurate surface current calculation could be minor misalignments between the physical antenna dimensions and its position in the measurement coordinate system and the model used for the reconstruction.

In order to test the filtering capabilities of the source reconstruction method,

all unwanted surface currents were filtered and only the ones close to the patch antenna were kept as shown in Fig. 5.5c. The filtered far field, shown in Fig. 5.6, was then calculated based on the filtered current distribution.

While the procedure only had a minor effect in the E-plane, where the impact of the reflector was limited, the ripples in positive θ-direction were successfully filtered. The distortion from the reflector had an ripple amplitude of up to 5 dB over the measurement angle θ, which was reduced to less than 0.5 dB through the source reconstruction procedure. The difference between the original measurement without reflector was also reduced in large parts of the pattern from over 5 dB to less than 1 dB for positive θ-values apart from the edge of the measurement plane at $\theta > 60°$.

However, the procedure did not yield meaningful results in the shadow region behind the reflector at $\theta < -30°$, where signal blockage occurred. The difficult realization of the source reconstruction method due to the necessity of an accurate 3D-model of the measurement setup, the high computational effort, and the complexity limit the benefit of this method. Antenna diagnostics to determine scattering centers are also challenging, illustrating scattering centers that do not align with the main reflectors in the setup (see Fig. 5.5a and [131]). This is especially challenging if small structures like bond wires were to be investigated, as the mesh cell size would have to be very limited in order to achieve a sufficient resolution, which would require high computational power and a long computing time.

For these reasons, modal filtering is used in the following section as a second method to mitigate the impact of the reflector on the radiation pattern of the 120 GHz patch antenna. Then the achievable performance of modal filtering is compared with the surface current approach.

5.3 MARS

Wave expansion techniques are commonly used in near-field to far-field conversions [132] and were first used to filter unwanted sources in antenna measurements in [133]. This Mathematical Absorber Reflection Suppression (MARS) technique uses wave expansion to separate direct and reflected radiation in post-processing, combined with a slightly modified measurement setup to increase the modal separation between the desired and the unwanted modal coefficients. This makes it possible to suppress unwanted radiation that was reflected from other objects in the measurement environment like mounting structures, feed-

ing devices, and imperfect absorbers, which is where the name stems from.

The only requirements for modal filtering are that the current distribution be limited in space and that reflectors be outside the MRS, which is a sphere of minimum radius surrounding the AUT. The method has been developed for different near-field measurement setups like spherical [134], cylindrical [135–137], planar [138], and more recently for far-field measurements [109, 139].

The diagram on page 80 shows the five main steps of the MARS technique using spherical wave expansion for a standard gain horn measurement at 160 GHz. The first step is to acquire the tangential field components of the radiated fields on a given measurement plane, e.g. E_ϕ and E_θ for a spherical antenna measurement. Unlike in standard antenna measurements, the AUT phase center is not located in the origin of the measurement coordinate system, but rather at an offset position. This off-center position of the AUT, aids the separation of wanted (direct) and unwanted (reflected) field components in the subsequent post-processing steps. In previous measurement setups for integrated antennas, different offsets were difficult to realize as it entails modifying the position of the integrated antenna and wafer probe. The presented setup, on the other hand, can easily accommodate different antenna displacement positions through GUI settings for various AUTs and angular resolutions.

In the second step, the phase of the measured fields is adjusted such that the offset position of the antenna is canceled out for direct radiation, i.e. the antenna is transformed back into the center of the measurement coordinate system. The translated fields are then used to compute the wave coefficients, which can be attributed to different source locations (step 3). Thus, sources in the center of the setup can be distinguished from reflections, which makes the filtering possible. After setting unwanted coefficients to zero (step 4), the undistorted far field can be determined through a back-transformation of the coefficients (step 5).

The robotic measurement setup facilitates convenient data acquisition with different settings (e.g. resolution, offset) for the spherical and cylindrical wave expansion. This makes it possible to analyze the impact of a certain setting on the filtered result and to verify subsequent steps against a reference measurement (e.g. back transformation, wave expansion results). In the following sections, the spherical and cylindrical wave expansions are explained to establish the connection between the out-of-center measurement capabilities of the setup (Section 5.3.3) and the final measurement results.

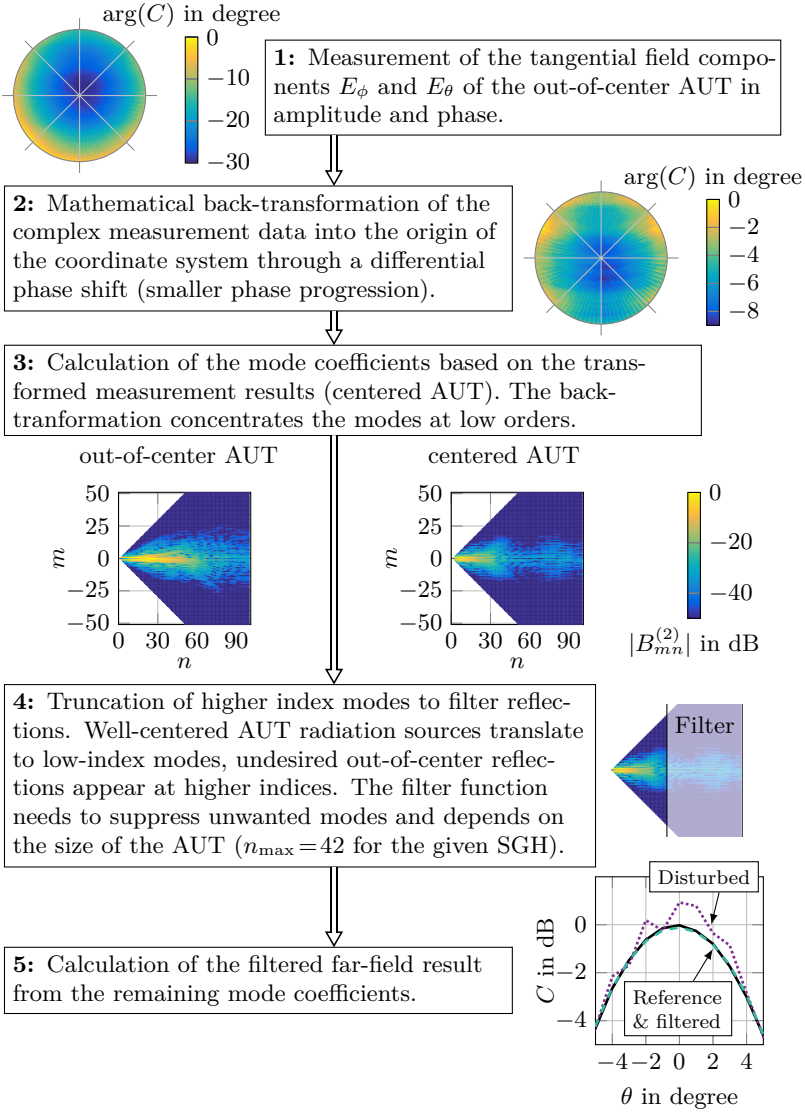

Fig. 5.7: Five main steps of the MARS algorithm.

5.3.1 Spherical Wave Expansion

The spherical wave expansion technique can be derived from the scalar wave equation. For a current-free and lossless space it is

$$\Delta\psi(\mathbf{r}) + k_0^2\psi(\mathbf{r}) = 0\,, \tag{5.3.1}$$

with the wave number k, the Laplace operator $\Delta = \nabla \cdot \nabla$ in spherical coordinates, and the scalar wave function $\boldsymbol{\psi}$, of which only the r-component ψ is taken into account. The ansatz is based on the assumption that the solution can be written as a product of functions that only depend on a single coordinate. For a coordinate system, as in Fig. 5.1a on page 71, the ansatz of the separation of variables approach is [140]

$$\psi(r,\theta,\phi) = R(r)\,\Theta(\theta)\,\Phi(\phi)\,. \tag{5.3.2}$$

As shown in [109, 141] a solution for the wave equation can be expressed as

$$\psi_{mn}^{(i)}(\mathbf{r}) = z_n^{(i)}(kr)\,P_n^{|m|}(\cos\theta)\,\mathrm{e}^{\,\mathrm{j}m\phi} \tag{5.3.3}$$

The ϕ-dependency is expressed through a complex exponential function and the behavior in r-direction, represented by $z_n^{(i)}(kr)$, can be described with one of the following functions, depending on the problem at hand:

1. First kind spherical Bessel function of order n
   $z_n^{(1)}(kr) = j_n(kr)$
2. Second kind spherical Bessel function of order n (Neumann function)
   $z_n^{(2)}(kr) = n_n(kr)$
3. First kind spherical Hankel function of order n
   $z_n^{(3)}(kr) = h_n^{(1)}(kr) = j_n(kr) + \mathrm{j}\,n_n(kr)$
4. Second kind spherical Hankel function of order n
   $z_n^{(4)}(kr) = h_n^{(2)}(kr) = j_n(kr) - \mathrm{j}\,n_n(kr)\,.$

The spherical Bessel functions of first and second kind ($i = 1, 2$) describe standing waves, while the Hankel functions ($i = 3, 4$) constitute traveling waves with different propagation direction. The case $i = 4$ describes outward-traveling waves in r-direction and the third solution $z_n^{(3)}(kr)$ inward-traveling waves.

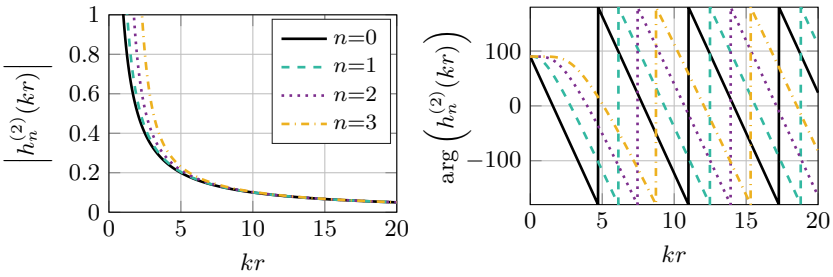

(a) Amplitude. **(b)** Phase.

Fig. 5.8: Spherical Hankel functions of the second kind for $n = 0, 1, 2$, and 3.

Additionally, the functions describe different source distributions. For a source-free region around the origin with a radius of r_0, the first solution $z_n^{(1)}(kr)$ is required as it has a finite value at the origin. For antenna measurements, however, all sources are usually limited within a sphere around the origin. This can be described with the solution $z_n^{(4)}(kr)$, which is the most suitable function for this case [132] and therefore

$$z_n^{(i)}(kr) \stackrel{!}{=} h_n^{(2)}(kr)\,. \tag{5.3.4}$$

Spherical Hankel Function

The Hankel function is defined as a linear combination of Bessel functions of the first and second kind

$$h_n^{(2)}(kr) = j_n(kr) - \mathrm{j}\, n_n(kr) = \sqrt{\frac{\pi}{2\,kr}}\left(J_{n+1/2}(kr) - \mathrm{j}\, Y_{n+1/2}(kr)\right)\,, \tag{5.3.5}$$

using the following relation between the ordinary Bessel functions of the first and second kind $J_n(kr)$ and $Y_n(kr)$ and their spherical counterparts $j_n(kr)$ and $n_n(kr)$:

$$j_n(kr) = \sqrt{\frac{\pi}{2\,kr}} J_{n+1/2}(kr)\,, \tag{5.3.6}$$

$$n_n(kr) = \sqrt{\frac{\pi}{2\,kr}} Y_{n+1/2}(kr)\,. \tag{5.3.7}$$

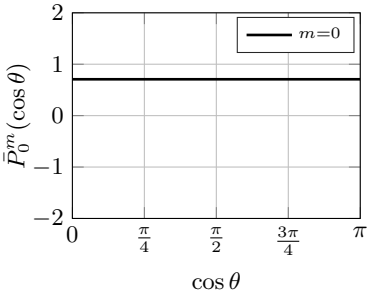

(a) Legendre function for n=0.

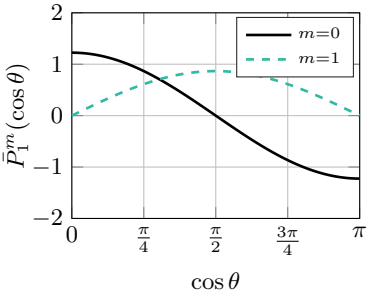

(b) Legendre function for n=1.

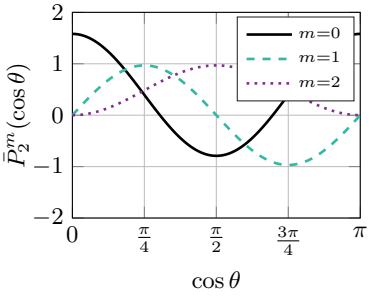

(c) Legendre function for n=2.

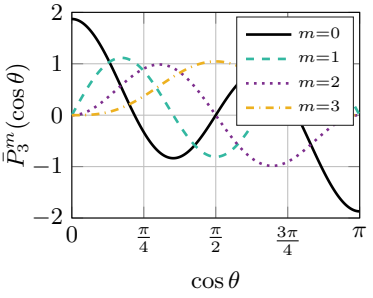

(d) Legendre function for n=3.

Fig. 5.9: Legendre function $\bar{P}_n^m(\cos\theta)$ for $n = 0, 1, 2, 3$ and their corresponding m

With the approximation of [132] for large arguments $kr \gg n$ for the spherical Hankel function $h_n^{(2)}(kr)$, the r-dependency of $\psi_{mn}^{(i)}(\mathbf{r})$ can be expressed as

$$h_n^{(2)}(kr) \overset{kr\to\infty}{\approx} \mathrm{j}^{n+1}\frac{\mathrm{e}^{-\mathrm{j}kr}}{kr}\,. \tag{5.3.8}$$

Figure 5.8 shows the amplitude and phase of the second spherical Hankel function to illustrate the r-dependency of $\psi_{mn}^{(i)}(\mathbf{r})$. The calculation of the wave function also requires the derivative of $h_n^{(2)}$, which can be approximated as

such [132]

$$\frac{1}{kr}\frac{\partial\left(kr\,h_n^{(2)}(kr)\right)}{\partial kr} = h_{n-1}^{(2)}(kr) - \frac{n}{kr}h_n^{(2)}(kr) \overset{kr\to\infty}{\approx} \mathrm{j}^n\frac{\mathrm{e}^{-\mathrm{j}kr}}{kr}\,. \tag{5.3.9}$$

Legendre Function

Lastly, the behavior in θ-direction of (5.3.3) constitutes an associated Legendre function with degree n and order m with the limits $0 \le n \le \infty$ and $-n \le m \le n$. It is defined like so

$$P_n^m(x) = \frac{(1-x^2)^{m/2}}{2^n n!}\frac{\mathrm{d}^{n+m}}{\mathrm{d}x^{n+m}}(x^2-1)^n\,. \tag{5.3.10}$$

The Legendre function can be normalized such that [109]

$$\int_{-1}^{1}\left(\bar{P}_n^m(x)\right)^2 dx = 1\,. \tag{5.3.11}$$

This normalization facilitates the radiated power calculation based on the mode coefficients. $\bar{P}_n^m(x)$ can be calculated with

$$\bar{P}_n^m(x) = \sqrt{\frac{2n+1}{2}\frac{(n-m)!}{(n+m)!}}\,P_n^m(x)\,. \tag{5.3.12}$$

Figure 5.9 shows the first 4 degree normalized Legendre functions $\bar{P}_n^m(x=\cos\theta)$ with their respective orders. Furthermore, Fig. 5.10 shows 3D-renderings of the Legendre functions as $|\bar{P}_n^m(x=\cos\theta)\,\mathrm{e}^{\mathrm{j}m\phi}|$ for a better spatial understanding of how far fields are constructed from a weighted sum of the individual functions. The final transformation into the modal domain on page 89 also requires the following two relations:

$$\frac{\partial\bar{P}_n^{|m|}(\cos\theta)}{\partial\theta} = \begin{cases} -\sqrt{\frac{2n+1}{2}}P_n^1(\cos\theta) & \text{if } m=0 \\ \frac{1}{2}\sqrt{\frac{2n+1}{2}\frac{(n-m)!}{(n+m)!}}\left\{(n-m+1)(n+m)P_n^{m-1}(\cos\theta)\right. & \\ \quad \left. - P_n^{m+1}(\cos\theta)\right\} & \text{if } m>0 \end{cases}$$

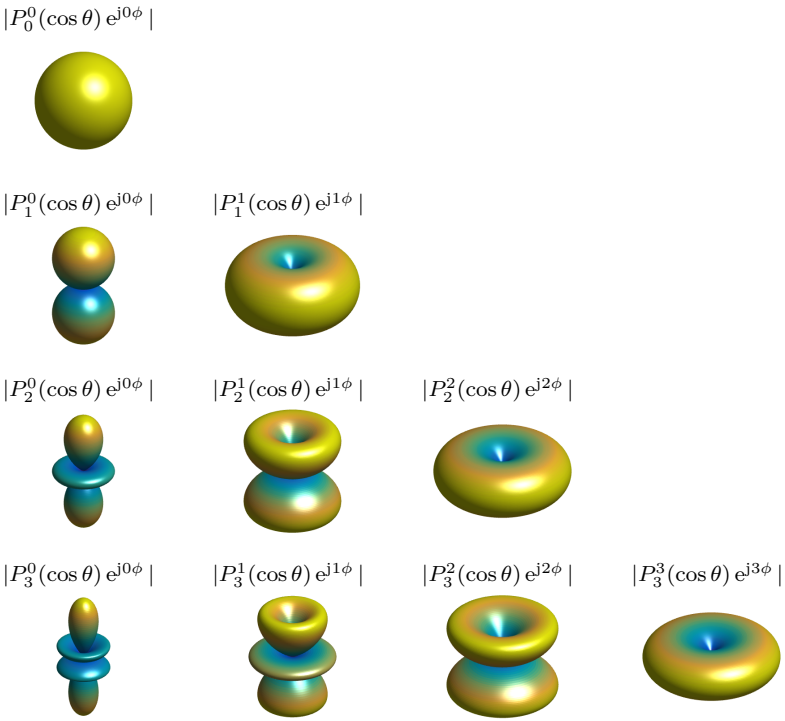

Fig. 5.10: Absolute value of the Legendre function for $m = 1 \ldots n$ and $n = 0, 1, 2, 3$.

$$\frac{m\bar{P}_n^{|m|}(\cos\theta)}{\sin\theta} = \begin{cases} 0 \qquad \text{if } m = 0 \\ \frac{1}{2}\cos\theta\sqrt{\frac{2n+1}{2}\frac{(n-m)!}{(n+m)!}}\left[\left\{(n-m+1)(n+m)P_n^{m-1}(\cos\theta)\right.\right. \\ \quad \left.\left. + \; P_n^{m+1}(\cos\theta)\right\} + m\sin\theta P_n^m(\cos\theta)\right] \qquad \text{if } m > 0\,. \end{cases}$$

Spherical Mode Coefficients

The solution of the wave equation $\psi_{mn}^{(i)}(\mathbf{r})$ (see (5.3.3)), can now be used to construct a vector field solution for the radiated E-field with a transverse electric (TE) and transverse magnetic (TM) component as shown in [109] for radiation in r-direction:

$$\mathbf{E}(\mathbf{r}) = \nabla \times r\,\hat{\mathbf{e}}_r\psi_{mn}^{(4)}(\mathbf{r}) + \frac{1}{k}\nabla \times \left(\nabla \times r\,\hat{\mathbf{e}}_r\psi_{mn}^{(4)}(\mathbf{r})\right). \tag{5.3.13}$$

The spherical wave functions $\mathbf{m}_{mn}^{(4)}$ and $\mathbf{n}_{mn}^{(4)}$ are defined as the TE and the TM components of E-field, respectively:

$$\mathbf{m}_{mn}^{(4)}(\mathbf{r}) = \nabla \times r\,\hat{\mathbf{e}}_r\psi_{mn}^{(4)}(\mathbf{r})\,, \tag{5.3.14}$$

$$\mathbf{n}_{mn}^{(4)}(\mathbf{r}) = \frac{1}{k}\nabla \times \left(\nabla \times r\,\hat{\mathbf{e}}_r\psi_{mn}^{(4)}(\mathbf{r})\right)\,. \tag{5.3.15}$$

As $\psi_{mn}^{(i)}$ is confined to its r-component, the curl operator (∇x) for spherical coordinates is

$$\nabla \times A_r\hat{\mathbf{e}}_r = \frac{1}{r}\left(\frac{1}{\sin\theta}\frac{\partial A_r}{\partial\phi}\right)\hat{\mathbf{e}}_\theta - \frac{1}{r}\left(\frac{\partial A_r}{\partial\theta}\right)\hat{\mathbf{e}}_\phi\,. \tag{5.3.16}$$

The spherical wave functions can be calculated by inserting (5.3.3) into (5.3.14) and (5.3.15):

$$\mathbf{m}_{mn}^{(4)}(\mathbf{r}) = h_n^{(2)}(kr)\,\mathrm{e}^{\mathrm{j}m\phi}\left[\frac{\mathrm{j}m}{\sin\theta}P_n^{|m|}(\cos\theta)\hat{\mathbf{e}}_\theta - \frac{\partial P_n^{|m|}(\cos\theta)}{\partial\theta}\hat{\mathbf{e}}_\phi\right] \tag{5.3.17}$$

$$\mathbf{n}_{mn}^{(4)}(\mathbf{r}) = \frac{n(n+1)}{kr}h_n^{(2)}(kr)P_n^{|m|}(\cos\theta)\mathrm{e}^{\mathrm{j}m\phi}\,\hat{\mathbf{e}}_r + \frac{1}{kr}\frac{\partial(kr\,h_n^{(2)}(kr))}{\partial kr}\,\mathrm{e}^{\mathrm{j}m\phi}$$

$$\left[\frac{\partial P_n^{|m|}(\cos\theta)}{\partial\theta}\hat{\mathbf{e}}_\theta + \frac{\mathrm{j}m}{\sin\theta}P_n^{|m|}(\cos\theta)\hat{\mathbf{e}}_\phi\right] \tag{5.3.18}$$

These equations show the attenuation observed by the tangential and the radial component of the spherical waves. As $h_n^{(2)}$ is proportional to $1/(kr)$ (see (5.3.8)), the radial component has a $1/(kr)^2$ dependency and the tangential components are attenuated with $1/(kr)$ for $kr \gg n$.

In order to obtain power values, the normalized spherical wave functions $\mathbf{M}_{mn}^{(4)}$ and $\mathbf{N}_{mn}^{(4)}$, a normalization factor is required, and the Legendre functions in (5.3.17) and (5.3.18) have to be substituted with the normalized Legendre function $\bar{P}_n^m$:

$$\begin{aligned}\mathbf{M}_{mn}^{(4)}(\mathbf{r}) &= A\mathbf{m}_{mn}^{(4)}(\mathbf{r})\,,\\ \mathbf{N}_{mn}^{(4)}(\mathbf{r}) &= A\mathbf{n}_{mn}^{(4)}(\mathbf{r})\,,\end{aligned} \tag{5.3.19}$$

with the normalization factor

$$A = \frac{1}{\sqrt{2\pi n(n+1)}}\cdot\begin{cases}1 & \text{if } m=0\\ \left(-\frac{m}{|m|}\right)^m & \text{otherwise}\,.\end{cases} \tag{5.3.20}$$

The radiated electric field can be expressed through a summation over all possible spherical wave functions, weighted with the complex spherical mode coefficients (SMCs) $B_{mn}^{(1)}$ and $B_{mn}^{(2)}$

$$\mathbf{E}(\mathbf{r}) = k\sqrt{\eta}\sum_{n=1}^{\infty}\sum_{m=-n}^{n}\left[B_{mn}^{(1)}\mathbf{M}_{mn}^{(4)}(\mathbf{r}) + B_{mn}^{(2)}\mathbf{N}_{mn}^{(4)}(\mathbf{r})\right]. \tag{5.3.21}$$

As the wave function itself is unitless, the factor $k\sqrt{\eta}$ determines the unit of the expression and sets it to $\sqrt{\text{Watt}}$. Together with the normalized Legendre functions $\bar{P}_n^m$ and the normalized spherical wave functions $\mathbf{M}_{mn}^{(4)}$ and $\mathbf{N}_{mn}^{(4)}$, this makes it possible to calculate the radiated power with a summation over all SMCs [132]

$$P = \frac{1}{2}\sum_{n=1}^{\infty}\sum_{m=-n}^{n}\left[\left|B_{mn}^{(1)}\right|^2 + \left|B_{mn}^{(2)}\right|^2\right]. \tag{5.3.22}$$

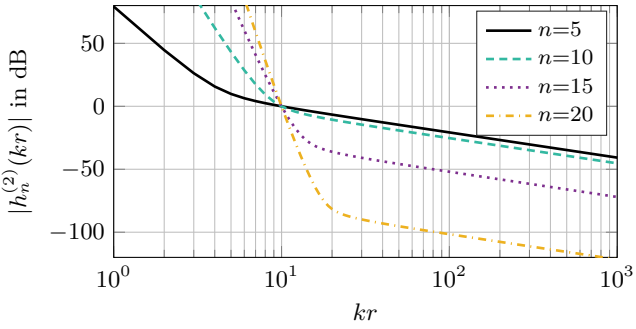

Fig. 5.11: Absolute value of the spherical Hankel function for different degrees n normalized such that $h_n^{(2)}(kr_0 = 10) = 0\,\text{dB}$

The wave coefficients allow the calculation of the radiated field at any given point in space outside of the MRS, which is a sphere around the origin of the coordinate system of minimum radius fully enclosing the source. Therefore, it is defined through its radius, i.e. the maximum radial extend (MRE) of the source.

In order to determine the SMCs for a certain field distribution, (5.3.21) must be solved for $B_{mn}^{(1)}$ and $B_{mn}^{(2)}$, which means that the number of required SMCs must be limited from a theoretically infinite number (see (5.3.21)) to a finite amount. This can be achieved by evaluating the influence of individual modes depending on the distance, which is determined by the spherical Hankel function. Assuming that all modes have a similar magnitude on the surface of the MRS as in [132], higher order wave functions are attenuated significantly outside of the sphere as shown in Fig. 5.11. Modes of degree $n > kr_0$ can therefore be neglected in the modal far-field representation of a radiation pattern, and only the first N modes have to be taken into account in the equations (5.3.21) and (5.3.22) with

$$N = \lfloor kr_0 \rfloor + n_1 = \left\lfloor \frac{2\pi r_0}{\lambda_0} \right\rfloor + n_1 \,. \tag{5.3.23}$$

The operator $\lfloor x \rfloor$ denotes the floor function and n_1 is a safety margin to ensure that none of the relevant modes are neglected in the calculations. It shows that

the number of modes solely depends on the radial expansion of the AUT and the chosen security margin and does not require any further knowledge of the antenna. Equation (5.3.21) can now be truncated for modes of a degree higher than N:

$$\mathbf{E}(\mathbf{r}) = k\sqrt{\eta}\sum_{n=1}^{N}\sum_{m=-n}^{n}\left[B_{mn}^{(1)}\mathbf{M}_{mn}^{(4)}(\mathbf{r}) + B_{mn}^{(2)}\mathbf{N}_{mn}^{(4)}(\mathbf{r})\right]. \tag{5.3.24}$$

For a spherical measurement setup that samples the radiated fields in ϕ- and θ-direction at a distance r_1, this expression can be split into the two relevant orthogonal components [109]

$$E_\theta(\mathbf{r}_1) = k\sqrt{\eta}\sum_{n=1}^{N}\sum_{m=-n}^{n}\left[B_{mn}^{(1)}\mathbf{M}_{mn}^{(4)}(\mathbf{r}_1) + B_{mn}^{(2)}\mathbf{N}_{mn}^{(4)}(\mathbf{r}_1)\right]\hat{\mathbf{e}}_\theta\,, \tag{5.3.25}$$

$$E_\phi(\mathbf{r}_1) = k\sqrt{\eta}\sum_{n=1}^{N}\sum_{m=-n}^{n}\left[B_{mn}^{(1)}\mathbf{M}_{mn}^{(4)}(\mathbf{r}_1) + B_{mn}^{(2)}\mathbf{N}_{mn}^{(4)}(\mathbf{r}_1)\right]\hat{\mathbf{e}}_\phi\,. \tag{5.3.26}$$

The parameter $\mathbf{r}_1$ specifies a point on the spherical measurement surface of radius r_1. Using the orthogonality of the SMC as shown in [109], the equations can be solved for $B_{mn}^{(1)}$ and $B_{mn}^{(2)}$. The final expressions are

$$\begin{aligned} B_{mn}^{(1)} = {} & \frac{(-1)^m}{k\sqrt{\eta}h_n^{(2)}(kr_1)}\frac{1}{\sqrt{2\pi n(n+1)}}\left(-\frac{m}{|m|}\right)^m \cdot \\ & \int_{\phi=0}^{2\pi}\int_{\theta=0}^{\pi}\left[E_\theta(\mathbf{r}_1)\left(-\frac{\mathrm{j}m}{\sin\theta}\bar{P}_n^{|m|}(\cos\theta)\right) + \right. \\ & \left. E_\phi(\mathbf{r}_1)\left(-\frac{\partial\bar{P}_n^{|m|}(\cos\theta)}{\partial\theta}\right)\right]\mathrm{e}^{-\mathrm{j}m\phi}\sin\theta\,\mathrm{d}\theta\,\mathrm{d}\phi \end{aligned} \tag{5.3.27}$$

and

$$B_{mn}^{(2)} = \frac{(-1)^m}{k\sqrt{\eta}\left[\frac{1}{kr_1}\frac{\partial(kr_1\,h_n^{(2)}(kr_1))}{\partial kr_1}\right]}\frac{1}{\sqrt{2\pi n(n+1)}}\left(-\frac{m}{|m|}\right)^m \cdot$$

$$\int_{\phi=0}^{2\pi}\int_{\theta=0}^{\pi}\left[E_\theta(\mathbf{r}_1)\left(\frac{\partial\bar{P}_n^{|m|}(\cos\theta)}{\partial\theta}\right)+ E_\phi(\mathbf{r}_1)\left(-\frac{\mathrm{j}m}{\sin\theta}\bar{P}_n^{|m|}(\cos\theta)\right)\right]\mathrm{e}^{-\mathrm{j}m\phi}\sin\theta\,\mathrm{d}\theta\,\mathrm{d}\phi\,, \tag{5.3.28}$$

These equations allow for calculating the spherical mode coefficients based on a spherical E-field measurement in ϕ- and θ-direction, and the spherical Hankel and Legendre functions. The angular resolution of the measurement can be determined based on the maximum degree N of modes that are required to represent the field distribution [132]

$$\frac{\Delta\theta}{\phi} < \frac{360^\circ}{2N+1}\,. \tag{5.3.29}$$

Far-field Calculation

The far field can be calculated based on (5.3.24) with (5.3.8) and (5.3.12), which yields the following formulas for the E-field at the position $\mathbf{r}=(r,\phi,\theta)$:

$$\begin{aligned}E_\theta(\mathbf{r}) &= k\sqrt{\eta}\sum_{n=1}^{\infty}\sum_{m=-n}^{n}A\,\mathrm{e}^{\mathrm{j}m\phi}\left[B_{mn}^{(1)}h_n^{(2)}(kr)\frac{\mathrm{j}m}{\sin\theta}\bar{P}_n^{|m|}(\cos\theta)\right.\\ &\quad\left.+\;B_{mn}^{(2)}\frac{1}{kr}\frac{\partial(kr\,h_n^{(2)}(kr))}{\partial kr}\frac{\partial\bar{P}_n^{|m|}(\cos\theta)}{\partial\theta}\right]\\ &= k\sqrt{\eta}\sum_{n=1}^{\infty}\sum_{m=-n}^{n}A\,\mathrm{e}^{\mathrm{j}m\phi}\left[-B_{mn}^{(1)}\frac{m}{\sin\theta}\bar{P}_n^{|m|}(\cos\theta)\right.\\ &\quad\left.+\;B_{mn}^{(2)}\frac{\partial\bar{P}_n^{|m|}(\cos\theta)}{\partial\theta}\right]\mathrm{j}^n\frac{\mathrm{e}^{-\mathrm{j}kr}}{kr}\end{aligned}$$

$$\begin{aligned}E_\phi(\mathbf{r}) &= k\sqrt{\eta}\sum_{n=1}^{\infty}\sum_{m=-n}^{n}A\,\mathrm{e}^{\mathrm{j}m\phi}\left[-B_{mn}^{(1)}h_n^{(2)}(kr)\frac{\partial\bar{P}_n^{|m|}(\cos\theta)}{\partial\theta}\right.\\ &\quad\left.+\;B_{mn}^{(2)}\frac{1}{kr}\frac{\partial(kr\,h_n^{(2)}(kr))}{\partial kr}\frac{\mathrm{j}m}{\sin\theta}\bar{P}_n^{|m|}(\cos\theta)\right]\end{aligned}$$

$$= k\sqrt{\eta}\sum_{n=1}^{\infty}\sum_{m=-n}^{n} A\,\mathrm{e}^{\mathrm{j}m\phi}\left[-\mathrm{j}\,B_{mn}^{(1)}\frac{\partial\bar{P}_n^{|m|}(\cos\theta)}{\partial\theta}\right.$$
$$\left. +\; B_{mn}^{(2)}\frac{\mathrm{j}m}{\sin\theta}\bar{P}_n^{|m|}(\cos\theta)\right]\mathrm{j}^n\frac{\mathrm{e}^{-\mathrm{j}kr}}{kr}\,.$$

5.3.2 Cylindrical Wave Expansion

Similar to the derivation of the spherical wave expansion, the cylindrical wave expansion also originates from the solution of the scalar wave equation. For a cylindrical coordinate system, as shown in Fig. 5.12a, the separation of variables ansatz is

$$\psi(r,\phi,z) = R(r)\,\Phi(\phi)\,Z(z)\,. \tag{5.3.30}$$

The solution can be found by plugging (5.3.30) into the scalar wave equation in cylindrical coordinates and according to [109] it can be written like so

$$\psi^{(i)}(r,\phi,z) = \sum_{m=-\infty}^{\infty}\int_{-\infty}^{\infty} B_m(k_z)Z_m^{(i)}(k_r r)\,\mathrm{e}^{-\mathrm{j}m\phi}\,\mathrm{e}^{-\mathrm{j}k_z z}\,\mathrm{d}k_z\,, \tag{5.3.31}$$

with the complex weighting factor $B_m(k_z)$. Depending on the problem, $Z_m^{(i)}$ can take different forms

$$\begin{aligned}
Z_m^{(1)}(k_r r) &= J_m(k_r r)\,, && \text{(First Bessel function of order } m)\\
Z_m^{(2)}(k_r r) &= Y_m(k_r r)\,, && \text{(Second Bessel function of order } m)\\
Z_m^{(3)}(k_r r) &= H_m^{(1)}(k_r r)\,, && \text{(First Hankel function of order } m)\\
Z_m^{(4)}(k_r r) &= H_m^{(2)}(k_r r)\,. && \text{(Second Hankel function of order } m)
\end{aligned}$$

While $Z_m^{(1)}$ and $Z_m^{(2)}$ denote standing waves, $Z_m^{(3)}$ and $Z_m^{(4)}$ describe inward- and outward-traveling waves respectively. Therefore, solution 4 is used for the cylindrical wave expansion:

$$Z_m^{(i)}(k_r r) \stackrel{!}{=} H_m^{(2)}(k_r r)\,. \tag{5.3.32}$$

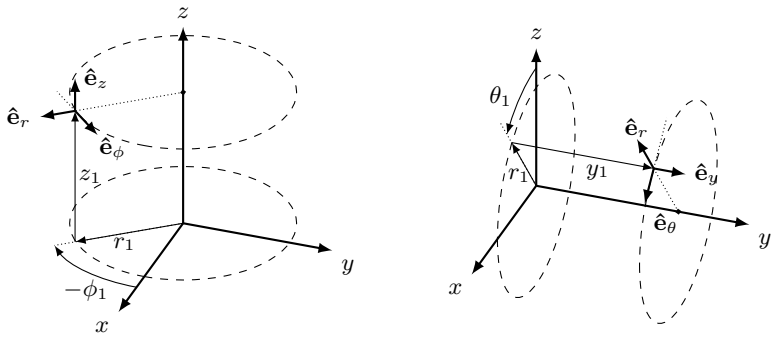

(a) Standard cylindrical coordinate system with the unit vectors displayed at (r_1, ϕ_1, y_1).

(b) Modified cylindrical coordinate system for the far-field MARS with the unit vectors at (r_1, θ_1, y_1).

Fig. 5.12: Cylindrical coordinate system definitions.

The Hankel function of the second kind is defined like so

$$H_m^{(2)}(x) = J_m(x) - \mathrm{j}Y_m(x)\,, \tag{5.3.33}$$

$$H_{-m}^{(2)}(x) = \mathrm{e}^{-\mathrm{j}\pi|m|}\, H_{|m|}^{(2)}(x)\,, \tag{5.3.34}$$

based on the Bessel functions of the first and second kind

$$J_m(x) = \sum_{n=0}^{\infty} \frac{(-1)^n}{n!(n+m)!}\left(\frac{x}{2}\right)^{2n+m}, \tag{5.3.35}$$

$$J_{-m}(x) = (-1)^m J_m(x)\,, \tag{5.3.36}$$

$$Y_m(x) = \frac{J_m(x)\cos(m\pi) - J_{-m}(x)}{\sin(m\pi)}\,. \tag{5.3.37}$$

Similar to the spherical wave expansion, the vector field representation of the fields can be obtained by splitting (5.3.31) into a TE and TM component relative to the z-axis. These components are represented by the vector wave functions $\mathbf{M}_{mk_z}^{(2)}$ and $\mathbf{N}_{mk_z}^{(2)}$. This eventually yields the following vector wave

function representation of the E-field at $\mathbf{r} = (r, \phi, z)$ [109]:

$$\mathbf{E}(\mathbf{r}) = \sum_{m=-\infty}^{\infty} \int_{-\infty}^{\infty} \left[B_m^{(1)}(k_z) \mathbf{M}_{mk_z}^{(2)}(\mathbf{r}) + B_m^{(2)}(k_z) \mathbf{N}_{mk_z}^{(2)}(\mathbf{r}) \right] \mathrm{d}k_z \,, \quad (5.3.38)$$

with the cylindrical mode coefficients (CMCs) $B_m^{(1)}$ and $B_m^{(2)}$, the following definitions for the vector wave functions

$$\mathbf{M}_{mk_z}^{(2)} = \left[\frac{\mathrm{j}m}{r} H_m^{(2)}(k_r r) \hat{\mathbf{e}}_r - \frac{\partial H_m^{(2)}(k_r r)}{\partial r} \hat{\mathbf{e}}_\phi \right] \mathrm{e}^{\mathrm{j}m\phi} \, \mathrm{e}^{-\mathrm{j}k_z z} \,, \quad (5.3.39)$$

$$\mathbf{N}_{mk_z}^{(2)} = \frac{1}{k} \left(-\mathrm{j}k_z k_r \frac{\partial H_m^{(2)}(k_r r)}{\partial r} \hat{\mathbf{e}}_r + \frac{mk_z}{r} H_m^{(2)}(k_r r) \hat{\mathbf{e}}_\phi + k_r^2 H_m^{(2)}(k_r r) \hat{\mathbf{e}}_z \right) \mathrm{e}^{\mathrm{j}m\phi} \, \mathrm{e}^{-\mathrm{j}k_z z} \,, \quad (5.3.40)$$

and the derivative of the Hankel function

$$\frac{\partial H_m^{(2)}(k_r r)}{\partial r} = k_r \left(H_{m-1}^{(2)}(k_r r) - \frac{m}{k_r r} H_m^{(2)}(k_r r) \right) . \quad (5.3.41)$$

Solving (5.3.38) for the CMCs as shown in [109] yields the following expressions to calculate $B_m^{(1)}$ and $B_m^{(2)}$:

$$B_m^{(1)}(k_z) = \frac{-1}{4\pi^2 k_r^3 \frac{\partial H_m^{(2)}(k_r r)}{\partial r}} \int_{-\infty}^{\infty} \int_0^{2\pi} \left(\frac{mk_z}{r} E_z(r, \phi, z) + k^2 E_\phi(r, \phi, z) \right) \mathrm{e}^{-\mathrm{j}m\phi} \, \mathrm{e}^{\mathrm{j}k_z z} \, \mathrm{d}\phi \mathrm{d}z \quad (5.3.42)$$

$$B_m^{(2)}(k_z) = \frac{-1}{4\pi^2 k_r^2 H_m^{(2)}(k_r r)} \int_{-\infty}^{\infty} \int_0^{2\pi} E_z(r, \phi, z) \mathrm{e}^{-\mathrm{j}m\phi} \mathrm{e}^{\mathrm{j}k_z z} \, \mathrm{d}\phi \mathrm{d}z \quad (5.3.43)$$

Far-field Calculation

For large arguments (i.e. in the far field), the Hankel function and its derivative can be approximated with [109]:

$$H_m^{(2)}(x) \approx \mathrm{j}^m \sqrt{\frac{2}{\pi x}}\, \mathrm{e}^{-\mathrm{j}-\frac{\pi}{4}}\,, \tag{5.3.44}$$

$$\frac{\partial H_m^{(2)}(ax)}{\partial x} \approx -\mathrm{j}aH_m^{(2)}(ax)\,. \tag{5.3.45}$$

By using these relations, (5.3.38) can be simplified, and the following expressions used to calculate the electrical field components E_ϕ and E_θ in the spherical far field based on the cylindrical mode coefficients can be derived, as shown in [109]:

$$E_\theta(r\to\infty,\phi,\theta) = -\mathrm{j}2k\sin\theta \sum_{m=-\infty}^{\infty} \mathrm{j}^m B_m^{(2)}(k\cos\theta)\,\mathrm{e}^{\mathrm{j}m\phi} \tag{5.3.46}$$

$$E_\phi(r\to\infty,\phi,\theta) = -2k\sin\theta \sum_{m=-\infty}^{\infty} \mathrm{j}^m B_m^{(1)}(k\cos\theta)\,\mathrm{e}^{\mathrm{j}m\phi}\,. \tag{5.3.47}$$

With these approximations, the calculation of the CMCs can also be simplified and calculated based on a spherical far-field measurement:

$$B_m^{(1)}(k\cos\theta) = \frac{\mathrm{j}^{-m}}{4\pi k\sin\theta}\int_0^{2\pi} E_\phi(r\to\infty,\phi,\theta)\,\mathrm{e}^{\mathrm{j}m\phi}\,\mathrm{d}\phi \tag{5.3.48}$$

$$B_m^{(2)}(k\cos\theta) = \frac{\mathrm{j}^{-m}}{4\pi k\sin\theta}\int_0^{2\pi} E_\theta(r\to\infty,\phi,\theta)\,\mathrm{e}^{\mathrm{j}m\phi}\,\mathrm{d}\phi\,. \tag{5.3.49}$$

The equations show that the cylindrical wave expansion can be performed on a 1D far-field cut in ϕ-direction for a fixed θ-value (e.g. in the x-y-plane, for a θ-value of $\theta = 90°$), and as the θ- and ϕ-component are decoupled in the equations, the co-polarized field component can be sufficient for the coefficient calculation of polarization pure antennas. This marks an important difference from the spherical wave expansion described in Section 5.3.1, which requires full 2D spherical measurements of both the E_ϕ and E_θ field components to perform reflection reduction in post-processing. Single-cut measurements can reduce the measurement time and effort significantly, when the analysis of a

few characteristic cuts (e.g. the E-plane and H-plane) is sufficient. Furthermore, depending on the measurement setup, the achievable angular coverage can be increased for a single cut compared to a 2D coverage.

For an antenna radiating in positive z-direction, the definition of the cylindrical coordinate system can be adjusted as shown in Fig. 5.12b such that spherical far-field measurements of constant ϕ can be processed. Thus, for a 1D E-field measurement at $\phi = \phi_1$, the CMCs can be calculated with

$$B_m^{(1)}(k\cos\phi_1) = \frac{\mathrm{j}^{-m}}{4\pi k \sin\phi_1} \int_0^{2\pi} E_\phi(r\to\infty, \phi_1, \theta)\, \mathrm{e}^{\mathrm{j}m\theta}\, \mathrm{d}\theta\,, \tag{5.3.50}$$

$$B_m^{(2)}(k\cos\phi_1) = \frac{\mathrm{j}^{-m}}{4\pi k \sin\phi_1} \int_0^{2\pi} E_\theta(r\to\infty, \phi_1, \theta)\, \mathrm{e}^{\mathrm{j}m\theta}\, \mathrm{d}\theta\,, \tag{5.3.51}$$

and the field components can then be calculated by interchanging the ϕ- and θ-dependency in (5.3.46) and (5.3.47).

Similar to the spherical wave expansion, higher order modes are attenuated and can be neglected for the far-field calculation because they have a comparatively small impact on the field components. The number of relevant modes is limited in $k\cos\phi$- and in m-direction and can be confined using the radius of the minimum radius cylinder (MRC) that encapsulates the AUT r_t and the wave number k

$$M^2 = (kr_t + m_1)^2 = m^2 + (k\cos\phi)^2\,, \tag{5.3.52}$$

with the safety margin m_1. For single-cut far-field measurements, the definition of the coordinate systems can be adjusted such that $\cos\phi = 0$ for the desired cut, which means that only modes in m-direction have to be taken into account.

5.3.3 Antenna Displacement

The MARS-technique is based on the wave expansion techniques described in Sections 5.3.1 and 5.3.2 combined with a measurement setup modification to enhance the filtering capability between desired and unwanted field components. An antenna with a certain MRS can be described fully by a finite number of spherical or cylindrical wave coefficients as stated in (5.3.23) and (5.3.52). Sources outside of the MRS/MRC of the antenna must therefore be represented by higher order modes. If these higher order modes are suppressed in the far-field calculation ((5.3.25) and (5.3.26) for the spherical case and (5.3.46)

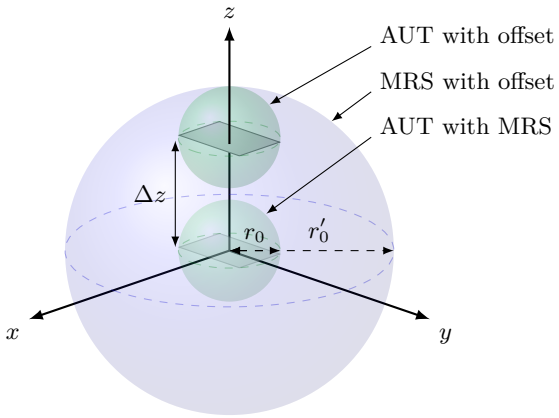

Fig. 5.13: Offset position of AUT increases the maximum radial extend and the size of the MRS [82], ©2017 IEEE.

and (5.3.47) for the cylindrical approach), the impact of scatterers and other unwanted sources can be suppressed:

$$B_{mn}^{(s)}(n>N) = 0\,, \quad s = 1,2 \qquad \text{(spherical)}\,,$$
$$B_{m}^{(s)}(m>M) = 0\,, \quad s = 1,2 \qquad \text{(cylindrical)}\,.$$

The larger the modal difference between direct and reflected radiation, the better the filtering that can be achieved, which is why MARS aims to maximize the modal distance through an out-of-center AUT measurement. By displacing the AUT by Δz as shown in Fig. 5.13, the maximum radial extend of the antenna is increased and therefore, the size of the MRS is enlarged, which means that the power is spread over a larger region in the modal representation of the radiation pattern. Knowing the offset Δz between the phase center of the AUT and the center of the measurement coordinate system around which the measurement is conducted, the AUT radiation can be transformed back into the origin of the measurement through a phase and amplitude transformation of the measured complex field data. This transformation must cancel out the phase and amplitude error that was introduced by the antenna displacement. As indicated in Fig. 5.14, the path difference between the modified antenna

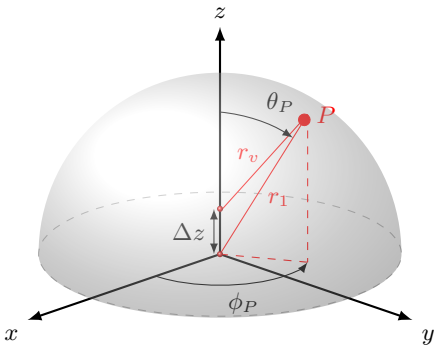

Fig. 5.14: Spherical coordinate system with propagation paths from origin and from the displaced antenna position to the observation point P for an offset of Δz [82], ©2017 IEEE.

position and a centered antenna to an observation point $P(r_1, \theta_P, \phi_P)$ is

$$\Delta r(\theta, \phi) = |\mathbf{r}_1(\theta, \phi)| - |\mathbf{r}_v(\theta, \phi)| = r_1 - r_v(\theta, \phi)\,, \tag{5.3.53}$$

with the measurement radius r_1. The path difference can then be used for the back transformation of the complex E-field

$$\mathbf{E}(\theta, \phi) = \left(\frac{r_v(\theta, \phi)}{r_1}\right)^2 \mathbf{E}_v(\theta, \phi) \mathrm{e}^{-\mathrm{j}k\,\Delta r(\theta,\phi)}\,. \tag{5.3.54}$$

As this transforms the AUT back into the origin of the measurement sphere, it should ideally cancel out any phase changes of the spherical measurement surface for radiation that originates from the phase center of the antenna (i.e. concentrating their power at lower degree modes in the modal domain), while introducing further phase changes for radiation from other sources or reflections and thus spreading them over a larger area in the mode spectrum. This increases the separation between desired and undesired field components and thus, improves the modal filter capacity. The sole requirement for this technique to be applicable is that the AUT and the reflectors be spatially separated and a displacement of $\Delta z > 2r_0$ be employed.

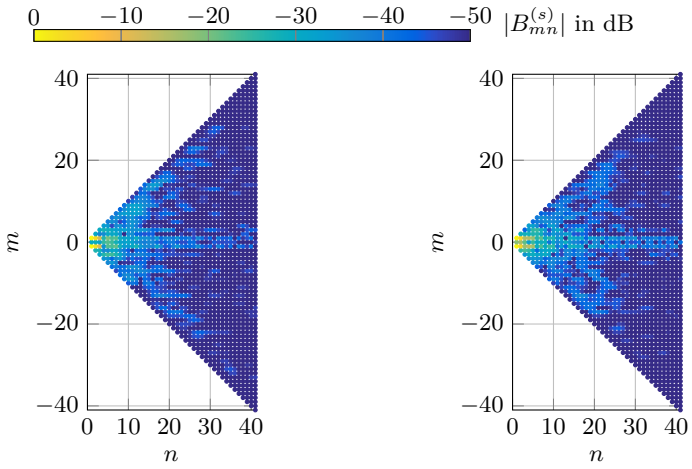

(a) $B_{mn}^{(1)}$.

(b) $B_{mn}^{(2)}$.

Fig. 5.15: Spherical mode spectrum of the patch antenna at 120 GHz.

5.3.4 Patch Antenna at 120 GHz

Until now the MARS technique has only been applied to antenna measurements below 100 GHz, which is why the functionality was first validated using the 120-GHz-patch antenna shown in Fig. 5.2.

In order to avoid truncation effects at the edges of the measurement surface, the maximum θ-angle should be as large as possible; however, as pointed out in Section 3.5.3, the movements of the robot—and thus the coverable measurement surface—are limited. The reach of the robot mainly depends on the measurement distance and increases with decreasing distance. In this case, the necessary far-field distance is $d = 2(2r_0)^2/\lambda = 1.6\,\text{mm}$, but a higher measurement distance of 150 mm was chosen in order to avoid collisions with the support structure of the AUT. The maximum achievable coverage was $\theta_{\max} = 70°$.

The maximum degree of modes necessary to represent the far field is

$$N/M = \lfloor kr_0 \rfloor + 10 = 11 \tag{5.3.55}$$

and the required angular resolution in ϕ- and θ-direction is

$$\Delta\theta/\phi < 360^\circ/(2N_1) = 15^\circ\,. \tag{5.3.56}$$

For an offset measurement with $\Delta z = 5\,\text{mm}$, the number of required modes increases to $N_o/M_o = 24$ and the angular resolution is $\Delta\theta_o/\phi_o = 7^\circ$ for the spherical and cylindrical case.

Figure 5.15 shows the calculated SMCs for a measurement of the patch antenna at 120 GHz. As expected, higher order modes have a relatively low amplitude, and modes of degree $n > 10$ are attenuated by at least 30 dB. The remaining power of these higher degree modes mainly stems from the limited scanning surface, contributions from the microstrip feeding line, and minor reflections from the measurement environment. When measuring the same antenna with the metallic reflector placed as shown in Fig. 5.2b with an antenna offset of $\Delta z = 5\,\text{mm}$, the MRS size is increased and thus, the power is spread over a larger area in the modal domain, as shown in Fig. 5.16. The impact of the reflector can primarily be seen in the $B_{mn}^{(1)}$ mode spectrum, while the displacement of the AUT is also visible in the $B_{mn}^{(2)}$ spectrum, where significant amplitudes can be seen up to a degree of around 20, which agrees with the expected $M_o = 24$. Due to the expansion of the reflector, the power distribution in the $B_{mn}^{(1)}$ spectrum is even more widespread and the power only decreases below $-20\,\text{dB}$ for degrees of $n > 35$.

The measured far-field data can now be transposed back into the origin of the measurement sphere as per (5.3.54) in order to cancel out the spectrum spread caused by the offset position. Figure 5.17 shows the calculated modes after the far-field transformation. The $B_{mn}^{(2)}$ modes are much more concentrated at lower degree modes compared to the spectrum shown in Fig. 5.16 and show a high agreement with the mode spectrum of the centered measurement shown in Fig. 5.15b. This indicates that the back-transformation has the desired effect of reversing the power spreading in the modal domain for the direct radiation of the AUT. The $B_{mn}^{(1)}$ mode spectrum is also shifted towards lower modes due to the transposition of the field. When comparing the spectrum to Fig. 5.15a the contribution of the reflector can clearly be seen, which mainly manifests itself in the range $10 < n < 20$. In this case, the reflector position is quite close to the antenna, which is why the modes that correspond to the reflector are still quite concentrated in the range $10 < n < 20$. For a bigger clearance between origin and reflector, this spreading of the unwanted modes increases.

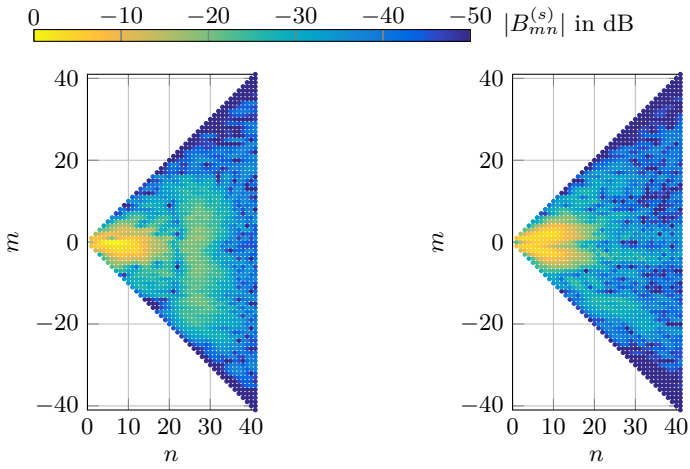

(a) $B_{mn}^{(1)}$ **(b)** $B_{mn}^{(2)}$

Fig. 5.16: Mode spectrum of an out-of-center measurement ($\Delta z = 5\,\text{mm}$) with reflector at $y = -5\,\text{mm}$.

When analyzing the same measurement using the cylindrical wave expansion in the E- and H-plane, a 1D-$B_m^{(1)}$ and 1D-$B_m^{(2)}$ mode representation for each cut is obtained, as shown in Fig. 5.18a, for the centered measurement without the reflector. As in the spherical case, the modes of degree $m > 10$ are attenuated by around 30 dB compared to the higher power modes. According to (5.3.50) and (5.3.51), the $B_m^{(1)}$ and $B_m^{(2)}$ modes correspond to either the co- or cross-polarization depending on the measurement plane. In this case, the $B_m^{(1)}$ coefficients represent the co-polarization in the $\phi = 0°$-plane and the $B_m^{(2)}$ coefficient in the $\phi = 90°$-plane. Therefore, when placing a resonator in $-y$-direction (i.e. $\phi = 90°$), as indicated in Fig. 5.2b, the $B_m^{(2)}$ component is affected, as shown in Fig. 5.18b. The main sidelobe of the mode spectrum can be observed at $m = -15$. With $r = n/k$ this corresponds to a reflector distance of around 6 mm, which coincides well with the distance of 5 mm between reflector and antenna. Accordingly, reflection points in x-direction would manifest themselves in the $B_m^{(2)}$ spectrum of the $\phi = 0°$-plane, which means that the mode representation makes it possible to estimate the location of scatterers

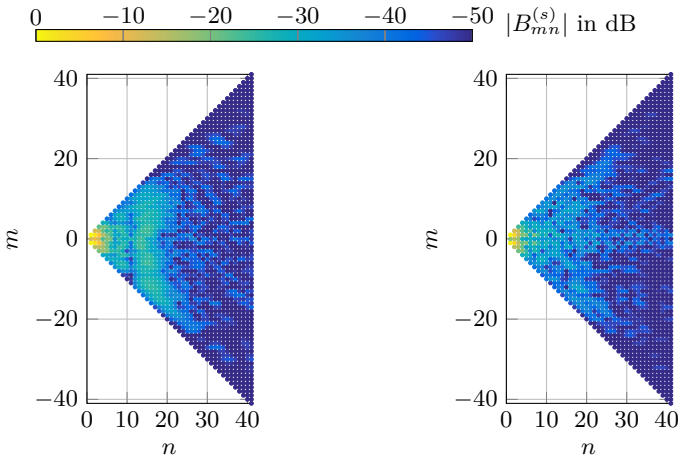

(a) $B_{mn}^{(1)}$ **(b)** $B_{mn}^{(2)}$

Fig. 5.17: Mode spectrum of an out-of-center measurement ($\Delta z = 5\,\text{mm}$) with reflector after the phase transformation into the origin of the measurement coordinate system.

in the measurement environment. A similar observation was made with the spherical mode coefficients. Reflections in x-direction appeared in the $B_{mn}^{(2)}$ mode spectrum and reflections in y-direction in the $B_{mn}^{(1)}$ spectrum, as shown in Fig. 5.17a, where the accumulation of modes in the area around $n = 15$ also indicates the correct reflector distance of approximately 5 mm.

By calculating the radiated fields using only the lower degree modes, the far field of the AUT—without interference from scatterers—can now be deter-

n_1	0	2	**4**	6	8	10	12	14
$\lvert\bar{\Delta}\rvert_{\phi=0°}$ in dB	3,8	1,0	**0,6**	0,7	1,0	1,2	1,3	1,7
$\lvert\bar{\Delta}\rvert_{\phi=90°}^{+}$ in dB	2,8	0,6	**0,3**	0,5	0,5	0,7	0,7	1,4

Tab. 5.1: Deviation between reference measurement without reflector and disturbed measurement after MARS post-processing.

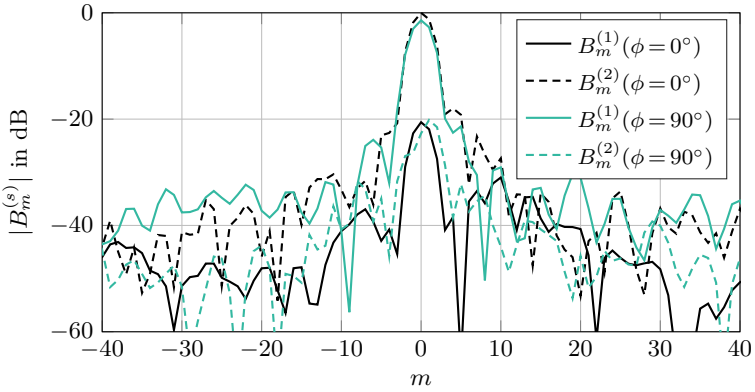

(a) Centered patch antenna without reflector.

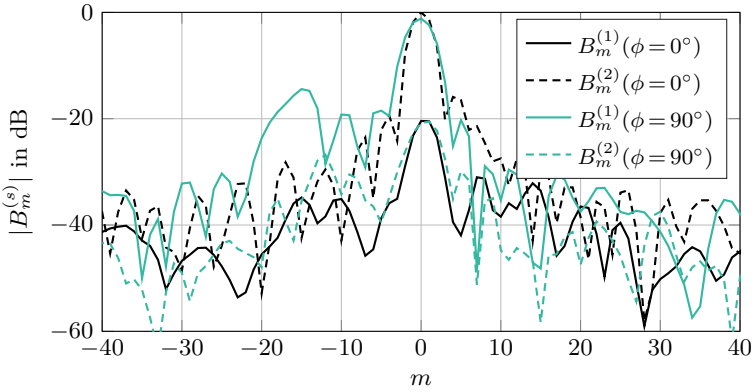

(b) Cylindrical mode representation of an AUT with reflector measured with an offset position of $\Delta z = 3\,\text{mm}$ after phase transformation into the origin.

Fig. 5.18: Normalized amplitude of the cylindrical mode coefficients for the patch antenna.

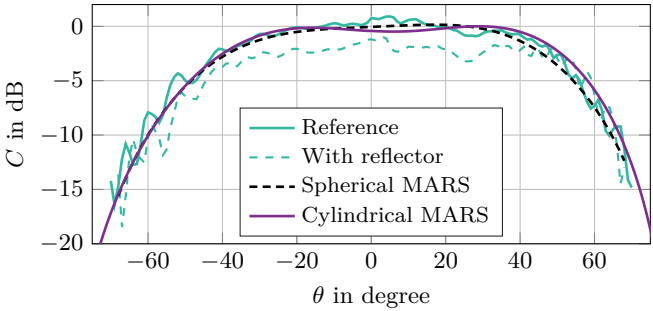

(a) E-plane ($\phi = 0°$).

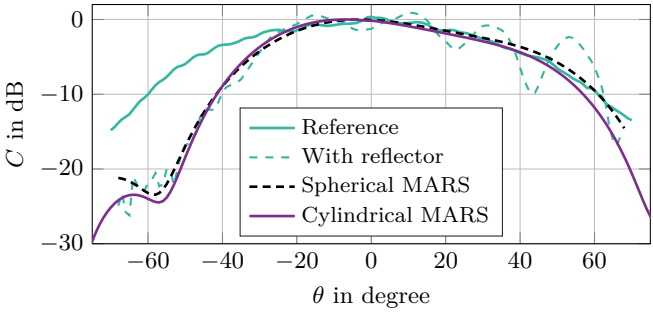

(b) H-plane ($\phi = 90°$).

Fig. 5.19: Reference without reflector, disturbed measurement, and MARS result for $N = 5$ of the patch antenna at 120 GHz.

mined. In the back transformation of the isolated AUT, the selection of the safety margin n_1 is important. When nearby scatterers are present, a smaller n_1 should be chosen to increase the filtering effect; when the measurement surface is restricted, n_1 should be increased to lessen the truncation effect at the edges of the measurement plane. Table 5.1 shows the mean deviation $|\bar{\Delta}|$ between a reference measurement without reflector and the filtered MARS measurement with reflector for different safety margins. As the reflector blocks the signal in $-\theta$-direction, only positive θ-values were taken into account in the $\phi = 90°$-plane. In this case, a safety margin of $n_1 = 4$ (bold numbers in

Table 5.1) yields the smallest deviation between original antenna and filtered result. Smaller margins neglect relevant antenna modes, while larger margins include more scattered power into the far-field transformation.

A comparison between the undisturbed reference measurement and the filtered results of spherical and cylindrical MARS results is shown in Fig. 5.19 for the E- and H-plane. All plots were normalized to the maximum value of the MARS filter result. Both the spherical and the cylindrical results show a much higher agreement with the undisturbed reference measurement than the unfiltered result in the E- and H-plane and deviate by less than 1 dB from each other. In the E-plane, the disturbed measurement is around 2 dB lower due to destructive interference with reflected radiation in the x-y-plane. In the H-plane, the scattered fields cause ripples with an amplitude of up to 5 dB for positive θ-values. Both these reflection effects can be successfully suppressed with the two MARS methods. Only the shadowing effect behind the reflector for $\theta < -20^\circ$ cannot be corrected.

In comparison to the results achieved with the source construction method shown in Fig. 5.4, both methods show a similar performance in the shadow region behind the reflector, but the MARS algorithm achieves smaller deviations between the measurement without reflector and the filtered results in the H-plane for positive θ-values, and it also shows a better interference suppression in the E-plane, where the filtered results exhibit fewer ripples. Due to the slightly better performance and the significantly lower requirements on the measurement setup, post-processing, and measurement effort, only the MARS method was considered for further analyses.

5.3.5 Passive Integrated Antenna Measurements

The following analysis were performed at 160 GHz using the integrated resonator antenna shown in Fig. 3.1 on page 20. In this section, the impact of a limited scanning surface and of an imperfect phase center are evaluated before the results for the radiation pattern and directivity of the antenna are shown [82]. The antenna was fed using wafer probes as opposed to the active antenna measurements in the next section, where the signals were generated by active integrated circuitry on the chip itself.

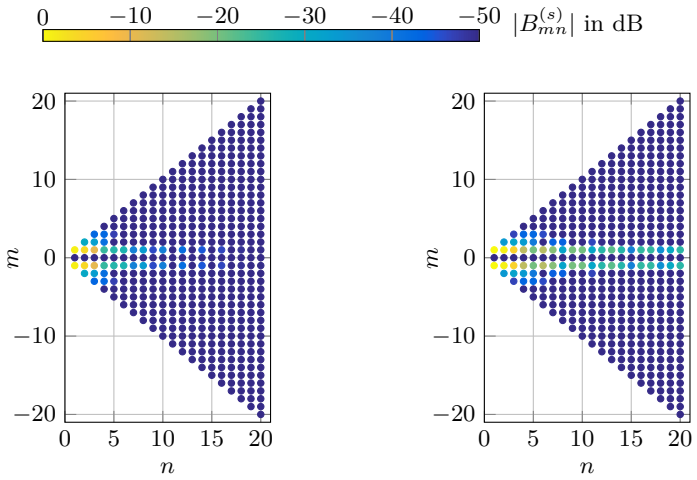

(a) $\theta_{\max} = 90°$.

(b) $\theta_{\max} = 50°$.

Fig. 5.20: Mode spectrum $B_{mn}^{(1)}$ of the simulated AUT at 160 GHz for different maximum scanning angles $\theta_{\max}$.

Limited Scanning Surface

The field truncation effect at the edges of the measurement surface as a result of the limited scanning area causes deviations in post-processing because the MARS algorithm tries to reproduce this non-linearity in the mode representation of the field. This turned out to be a minor issue when measuring the patch antenna in the previous section, because the maximum achievable θ-angle was 70° where the field was already attenuated by around 15 dB compared to the maximum. For the integrated antenna, the maximum angle is more restricted due to the feeding fixture of the wafer probe and the connected frequency extension module, which are located above the antenna surface (in positive z-direction). Therefore, the maximum measurement angle is limited to $\theta_{\max} < 50°$ for spherical measurements.

Figure 5.20 shows the calculated spherical mode coefficients based on a simulation of the integrated antenna for different coverage areas, i.e. $\theta_{\max}$-angles.

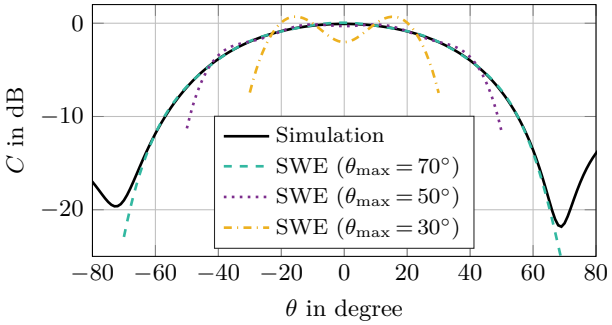

Fig. 5.21: Impact of a limited scanning surface on the calculated far field in the E-plane based on spherical wave coefficients of degree $n \leq 13$.

When taking the complete upper hemisphere into account, the spherical mode coefficients are decayed for $n > 3$ (see Fig. 5.20a), which agrees with the expected minimum number of required mode coefficients for the antenna dimensions. When limiting the maximum angle to $\theta_{\max} = 50°$, more power is assigned to higher order modes, especially of order $|m| = 1$ as shown in Fig. 5.20b. The impact on the far field calculated from these spherical modes is shown in Fig. 5.21 for $N = 13$. As the algorithm tries to replicate the truncation, the radiation pattern shows too low values at the edges of the scanning surface after the retransformation into the far field. Additionally, the pattern is superimposed with a wave shape that becomes more pronounced for smaller scanning surfaces. Besides the scanning area, the value of the safety margin also effects the form and amplitude of this wave pattern. Figure 5.22a shows the calculated far field for a $\theta_{\max} = 50°$-simulation for different N and illustrates that a larger safety margin reduces the deviation between the original result and the post-processed MARS radiation pattern. The value of the safety margin must therefore be chosen as a trade-off between filter performance and minimal impact of the measurement surface truncation. For the present integrated antenna and $\theta_{\max} = 50°$, $n_1 = 10$ proved to be a well-suited compromise and is used for all passive integrated antenna measurements.

Figure 5.22b shows the subtraction of the post-processed result from the original radiation pattern (i.e. the transformation error). As this error is deter-

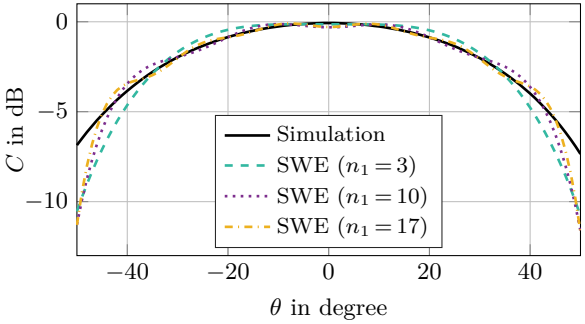

(a) Radiation pattern comparison.

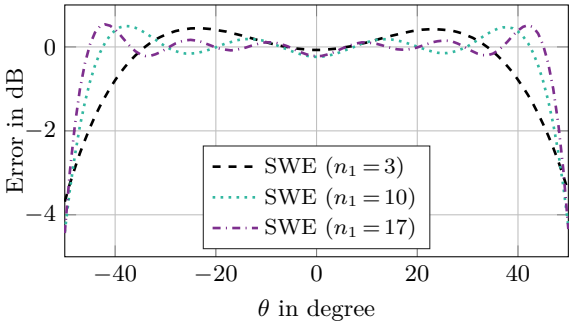

(b) Difference between simulation and calculation.

Fig. 5.22: Comparison of the calculated far-field pattern in the E-plane for different amounts of considered modes $N = 3 + n_1$ ($\theta_{\max} = 50^\circ$) [82], © 2017 IEEE.

ministic for a given radiation pattern, the theoretical error can be subtracted from a transformed measurement result to reduce the impact of a limited scanning surface.

Phase Center

For the translation of the measured off-center far field back into the center of the measurement coordinate system, the exact location of the phase center of the AUT is required. A higher phase-center accuracy decreases the power spread in the modal domain and yields a more focused mode spectrum, which reduces the necessary amount of modes for the back-transformation and thus, ultimately increases the filter performance of the procedure. With wave lengths of around 2 mm and antenna sizes of less than 1 mm, the accuracy of the used laser range finder was not sufficient to determine the antenna location and to achieve the desired mode concentration effect. The far-field-based phase-center determination method shown in Section 3.3 works well for undistorted measurements, but can be affected by reflections that alter the phase on the measurement surface since the method is based on the measured phase. A different method is the previously mentioned flip-test shown in [91, 92] which also calculates the phase center based on a far-field measurement, but was only used for corrections in one plane and requires multiple measurements.

In order to get a higher phase-center location accuracy in the presence of strong reflectors (e.g. wafer probes), a new method based on the spherical mode coefficients was developed. As the power in the modal domain is focused in lower degree modes for a well-centered AUT, the power distribution can

Tab. 5.2: Calculated offsets δx, δy, and δz from the phase center of the AUT.

	δx in mm		δy in mm		δz in mm	
Wafer probe	A	B	A	B	A	B
Far-field method						
$\Delta z = 0\,\text{mm}$	2.7	3.0	0.5	0.2	2.6	1.6
$\Delta z = 6\,\text{mm}$	2.6	2.9	0.5	0.3	8.7	7.6
Mode method						
$\Delta z = 0\,\text{mm}$	3.1	3.1	0.3	0.3	2.2	2.3
$\Delta z = 6\,\text{mm}$	3.0	3.0	0.2	0.3	7.8	8.3

be used as a quality criterion of the phase-center accuracy. If the AUT is in the correct phase center, the MRS is minimal, which yields the minimum number of relevant modes. Based on this, a phase-center optimization can be performed. In this case, the number of modes with a relative magnitude of over $-5\,\mathrm{dB}$ was minimized using the Nelder-Mead optimization method [142]. As this optimization is quite sensitive to the starting value, an initial far-field phase-center determination was performed, and the obtained phase center was used as the starting point for the subsequent SMCs optimization.

In order to evaluate the performance of the far-field method compared to the mode method, an integrated antenna was measured twice in the exact same position with two different wafer probes (the standard and custom wafer probe shown in Section 3.6) and offset positions. Ideally, the calculated phase-center offset positions of the AUT should not depend on the used wafer probe and offset position, except for the offset in z-direction, which increases with the deliberate offset Δz. The calculated offsets are shown in Table 5.2. While the phase-center position deviates by around $300\,\mu\mathrm{m}$ in the x- or y-plane between the two wafer probes (A, B) when using the far-field method, the offsets calculated with the mode method are hardly affected by different offset positions or wafer probes, which shows that the mode method is more robust and less susceptible to distortions. The position of the phase center changes with the frequency and observation point with the largest variations in z-direction, which is why the biggest deviations in Table 5.2 occur along the z-axis.

Radiation Pattern

The radiation pattern was analyzed with both the standard and the custom wafer probe and compared to a simulation of the antenna without the wafer probe for an undistorted reference.

Figure 5.23 shows the $B_{mn}^{(2)}$ mode spectrum of the integrated antenna based on simulation results as well as measurement results obtained from extended and standard probe measurements. The figures clearly show the added reflections when measuring with the extended or standard probe compared to the simulation result. The reason for the slow decrease of the mode amplitude of order $|m| = 1$ is the limited scanning surface, which was restricted to $\theta_{\max} = 50°$. The majority of reflections occur within a distance of $20\,\mathrm{mm}$ when measuring with the standard probe, which corresponds to $n \approx 65$ and thus higher degree modes can be neglected in the mode spectrum.

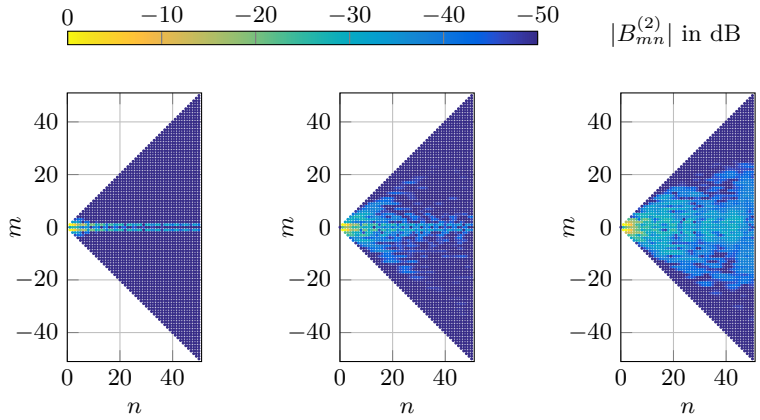

(a) Simulation. **(b)** Extended probe. **(c)** Standard probe.

Fig. 5.23: $B_{mn}^{(2)}$ spherical mode coefficients simulation and measurement results measured with the extended probe and the standard wafer probe.

The cylindrical mode coefficients for the same antenna measured with the standard probe are shown in Fig. 5.24. As expected, the probe reflections from the standard probe in the E-plane cause the power to spread over a wider range in the spectrum compared to the H-plane mode representation, where modes of the order $|m| > 3$ are already attenuated by over 20 dB.

The calculated spherical or cylindrical mode coefficients can again be used to estimate the main points of reflection, which can be used to check and validate the reflection centers calculated based on the far-field interference pattern shown in Fig. 3.20a. Figures 5.23c and 5.24 indicate that the main reflections occur between modes of degree 18 and 48, which translates to 5.4 mm and 14.3 mm respectively (see Fig. 5.25), according to $r = n/k$.

The filtered results of both the spherical and cylindrical mode expansion are depicted in Fig. 5.26. In order to maintain the correct relative amplitudes between the different radiation patterns, the power of the filtered modes was transferred to the lower degree modes and all fields were then normalized to the same value. The measurement of the antenna using the extended wafer probe serves as a reference to assess the performance of the algorithms. The robot

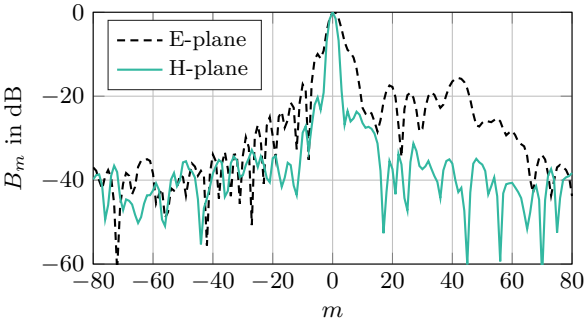

Fig. 5.24: Cylindrical mode coefficients of the integrated antenna measured at 160 GHz.

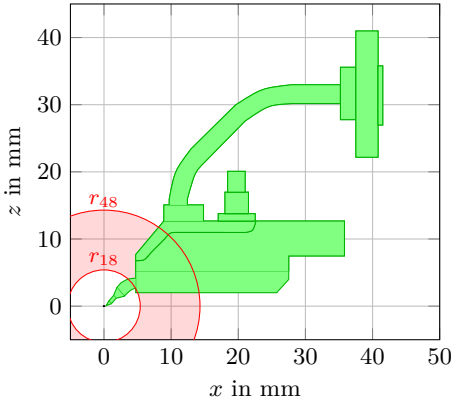

Fig. 5.25: Main reflection area based on the spherical or cylindrical mode distribution.

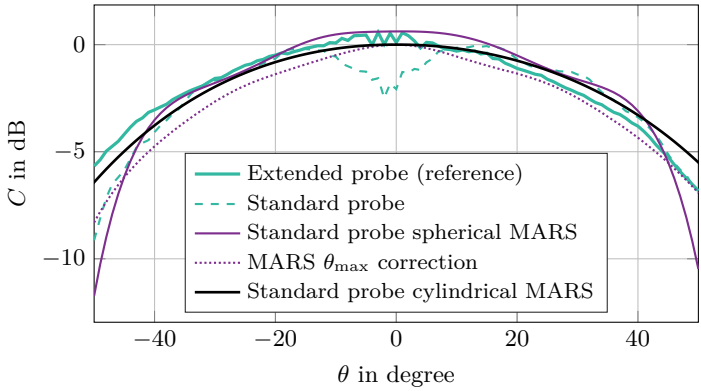

(a) H-plane ($\phi = 90°$).

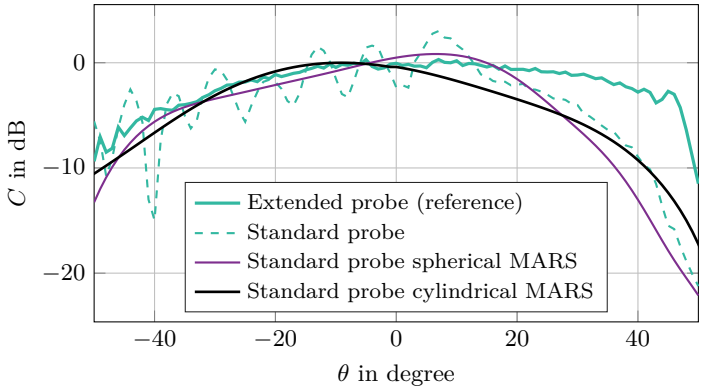

(b) E-plane ($\phi = 0°$).

Fig. 5.26: Comparison of measurement and post-processed radiation pattern of the integrated antenna at 160 GHz. The extended probe measurement was used as a reference and the standard probe measurement was filtered using spherical and cylindrical MARS.

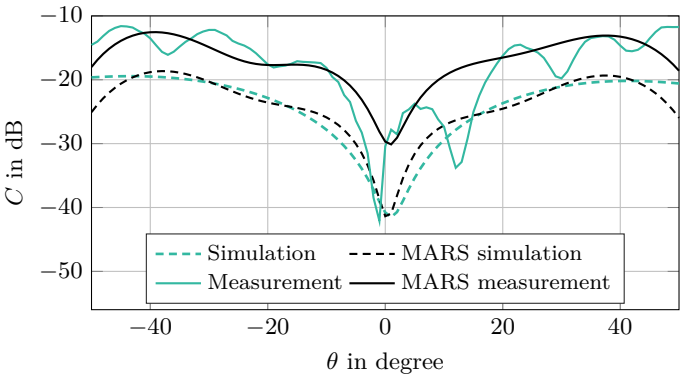

Fig. 5.27: Comparison between measured and simulated cross-polarization in the H-plane at 160 GHz before and after post-processing [82], © 2017 IEEE.

movement was mainly limited to the feeding structure of the wafer probes, located in the E-plane of the antenna. As the cylindrical wave expansion allows a separate evaluation of the different cuts, the measurement taken in the H-plane can be performed for a larger θ-range, which lessens the impact of the truncation at the edge of the scanning surface. While eliminating the notch around $\theta = 0°$, the spherical MARS result in Fig. 5.26a yields too low amplitudes close to the edges. This error can be corrected for well-defined radiation patterns based on the deviation of a processed reference result. The corrected result is shown by the dotted line in the figure (MARS $\theta_{\max}$ correction) and lessens the edge deviations. The best result in the H-plane, however, can be achieved using the cylindrical MARS, based on a measurement with $\theta \leq 90°$. The cylindrical MARS does not only successfully remove the interference around $\theta = 0°$, but the result also deviates by less than 1.2 dB from the reference measurement over the entire evaluation region.

In the E-plane, both MARS methods filter out the strong interference from the wafer probe and eliminate the interference pattern observed when measuring with the standard probe. In negative θ-direction, the filtered results show a high agreement with the reference measurement, reducing the maximum deviations from up to 10 dB to 2 dB.

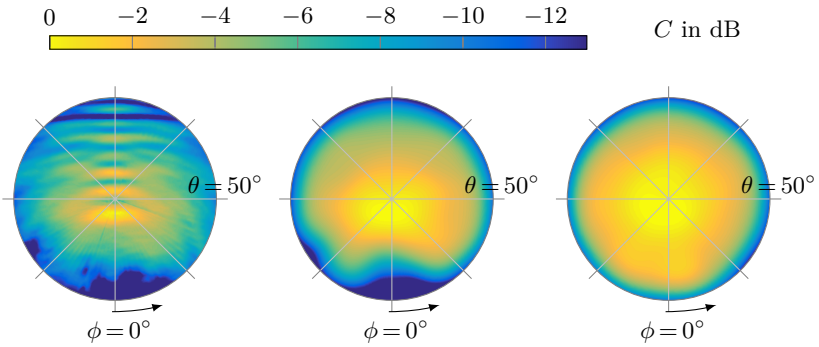

(a) Measurement with standard probe.

(b) MARS with standard probe.

(c) Measurement with extended probe.

Fig. 5.28: 3D-radiation pattern of the integrated antenna at 160 GHz. The probe is located at $\phi = 0^\circ$ [100], ©2017 IEEE.

The technique can also be applied to filter out unwanted reflections in the cross-polarization since the back-transformation yields the complex E_ϕ- and E_θ-fields. Figure 5.27 shows the cross-polarization result of the integrated antenna. The filtered result shows the same progression as the simulated result. The offset of around 7 dB between simulation and measurement is caused by the manual positioning of the dielectric resonator on the chip, which has a significant effect on the cross-polarization behavior of the antenna.

Directivity

In the presence of strong wafer-probe reflections, the calculation of the directivity of integrated antennas is unreliable, and the results are affected by the interference between the different propagation paths from AUT to the probing antenna. The directivity is usually overestimated due to constructive interference between direct and reflected fields, which makes the antenna seem more focused in the direction of the constructive interference.

The extent of the standard wafer-probe distortions on a spherical radiation

pattern measurement is shown in Fig. 5.28a for $0° \leq \phi < 360°$ and $0° \leq \theta \leq 50°$. The obtained radiation pattern bears no resemblance to the reference measurement taken with the extended wafer probe shown in Fig. 5.28c, which shows the smooth pattern expected from simulation results. Only after the distortions of the standard probe were filtered, using the spherical MARS algorithm, does the pattern constitute a meaningful rendering of the actual antenna pattern (Fig. 5.28b). The only remaining differences to the reference measurement are due to the blockage of the probe in $\phi = 0°$-direction and due to the truncation of the measured fields at $\theta = 50°$. After the wafer-probe distortions have been removed from the radiation pattern, the directivity can be determined reliably.

The directivity was calculated by integrating over the pattern measured on a spherical surface around the antenna using (3.4.5). Table 5.3 shows the obtained results for simulation and the measurements with the two different wafer probes before and after post-processing. The post-processing has only a minor effect on the simulation results of 9.6 dB, but improves the measurement results considerably. When measuring with the extended probe, the difference to the simulation results is reduced from 0.9 dB to 0.1 dB. The measurement result with the standard probe suffered the largest deviations with a difference of 2.2 dB compared to the simulation results, which is due to the constructive interference of the propagation paths. Through the MARS procedure the deviations were reduced to 1.1 dB.

Gain

As stated in Section 3.7.2 on page 53, the phase difference between direct and reflected radiation at the measurement location, and the resulting constructive or destructive interference, distorts standard probe gain measurements significantly. During the post-processing, the power is transferred from filtered modes to the modes of interest. Therefore, the absolute power information is

Tab. 5.3: Measured directivity of the integrated antenna at 160 GHz.

	Simulation in dB	Extended probe in dB	Standard probe in dB
No post-processing	9.6	8.7	11.8
MARS	9.5	9.4	10.7

maintained and thus the gain comparison method can still be used. After the interference ripples of the far field have been removed, the previous difference of around 2 dB between the extended and standard probe gain result at 160 GHz shown in Section 3.7.2 is reduced to less than 0.5 dB, which marks a notable improvement achieved through post-processing.

5.3.6 Active Integrated Antenna Measurements

For antenna prototyping, passive antenna measurements, with external frequency generation and feeding equipment, offer a quick and comparatively cheap method to characterize the AUT. However, this is not a workable approach when measuring an antenna integrated on a chip together with the required frequency-generating circuitry, because the limited chip space might not allow connecting external components with the AUT. Furthermore, the use of wafer probes is not desired when measuring an antenna within a system in order to analyze its interaction with the surrounding circuitry, to validate the its characteristics within the final setup, and for diagnostics of a faulty circuit. Even in the absence of wafer probes, these measurements can suffer from distortions from objects in the measurement environment like the edges of the MMIC, the connecting bond wires, or the PCB.

Figure 5.29 shows the setup for an active antenna measurement using the transmitter path of an integrated radar chip [11, 12]. As the radio frequency signal is generated on the chip, the signal at the input of the AUT cannot be accessed and the time dependency of the transmitted phase cannot be canceled out at the receiver. This time dependency has to be removed from the measurement data, since the MARS algorithm requires the measurement-location-dependent phase information. In order to measure the time-dependent phase of the AUT input signal, an additional receiving antenna was used (reference antenna in Fig. 5.30). If this phase reference antenna remains at a fixed location during the measurement, the measured phase solely depends on the time drift of the AUT signal, and therefore, the signal can be used to remove the time dependency from the measurement signal for further processing by subtracting the time dependency. The remaining time dependency of the phase, measured with a static Rx antenna, was less than 1° over a 20 min period. A horn antenna was used for the phase reference antenna as its high gain makes it possible to locate it outside the main radiation direction of the AUT to minimize its interference with the measurement.

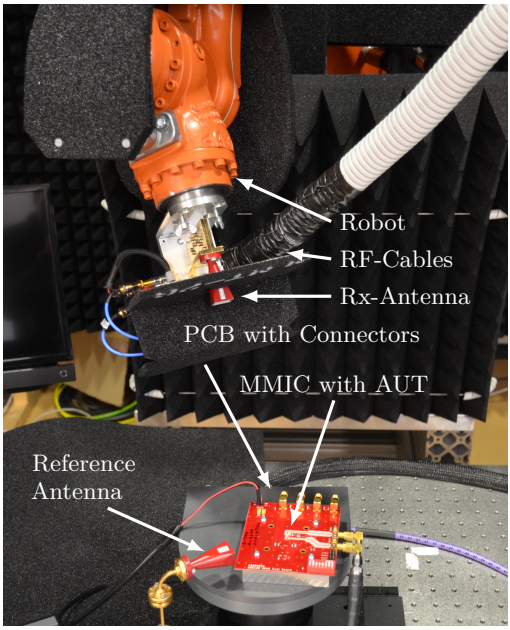

Fig. 5.29: Measurement setup for active measurements of an integrated antenna at 160 GHz. A static reference antenna is used to cancel out the time dependency of the phase in the measured signal [100], © 2017 IEEE.

Figures 5.31 and 5.32 show the post-processed radiation patterns and reflection centers for different N. The larger the N, the more reflections are taken into account for the far-field calculation and the more ripples can be seen in the calculated patterns. If the point of reflection is calculated based on these far-field ripples, it gradually moves closer to the AUT as N is decreased. For $N = 18$, the main point of reflection occurs at a distance of around 5.1 mm. This reflection can be filtered, if N is decreased; however, closer reflections still occur, which indicates that the PCB does not have one major reflection center, but rather many smaller ones at different distances. While the main reflections occurs at a distance of 10 mm to 20 mm for standard wafer-probe

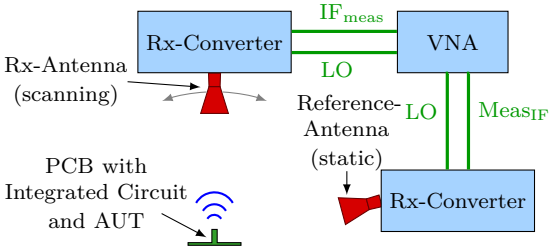

Fig. 5.30: Block diagram of the active antenna measurement setup with the phase reference antenna [100], © 2017 IEEE.

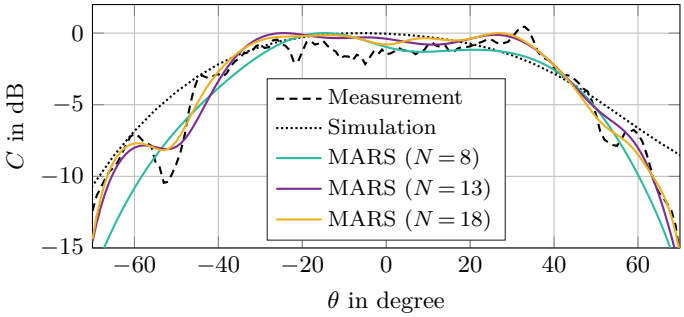

Fig. 5.31: Comparison of MARS result for different numbers of considered modes [100], © 2017 IEEE.

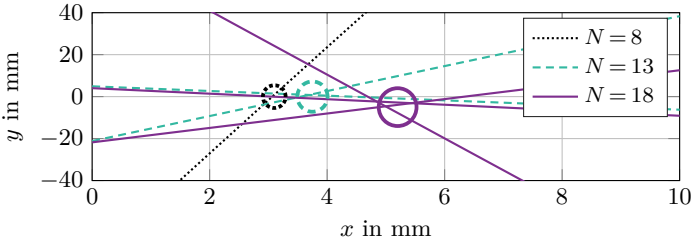

Fig. 5.32: Location of scattering centers for different N. Scattering occurs where the lines intersect with the PCB surface ($y = 0$). The AUT is located at (0,0) [100], © 2017 IEEE.

measurements, the active antenna measurement setup has a gradual transition between desired and unwanted sources, which is why the chosen safety margin n_1 has to be smaller in order to achieve a sufficient filtering effect in the presence of close reflectors (e.g. bond wires). On the other hand, a small safety margin increases the truncation effect at the edges of the measurement surface. However, without the restrictions that come with the positioning requirements of wafer probes, the measurement area could be increased to $0° \leq \theta \leq 70°$, which means that the non-linearity at the boundary region is decreased and thus a smaller n_1 is sufficient. The size of the region of interest, and therefore the MRS, depends on the type of antenna measurement. If the radiation characteristic of the final chip is of interest, N should be chosen such that the radius $r = N/k$ encloses the entire chip; if the functionality of the isolated antenna is investigated, $r = N/k_0$ should only enclose the antenna itself.

Radiation Pattern

Figures 5.33a and 5.33b show the post-processed radiation patterns of the isolated antenna. In order to successfully filter the impact of the PCB and chip from the measured far-field result, the MRS should only contain the AUT, which means that the safety margin should be set to $n_1 = 0$. This yields $N = 3$ with the given antenna dimensions. The region taken into account is indicated by the red circle around the Tx-antenna of the bistatic radar chip. Besides the measured and the post-processed radiation pattern, the figures show the simulation result and—as the resonator was glued manually onto the chip surface—the plots also indicate a region of possible radiation pattern based on an estimated positional resonator accuracy of 40 µm (simulation spread).

The measurement result shows strong distortions from the surrounding components when compared to the smoothness of the simulated radiation pattern in both the E- and H-plane. The MARS filtering, however, reduced the deviations in the E-plane from over 2 dB to less than 0.2 dB within 60° of the main lobe. A similar performance has been achieved for negative θ-angles in the H-plane, but bigger deviations remain for positive θ-angles. This could be due to a bond wire that is located within the MRS next to the AUT in the H-plane and which is too close to be filtered.

Figure 5.34 shows a radiation pattern analysis for the complete chip. In order to take the far-field contributions of the entire chip into account, while filtering out surrounding circuitry, the MRS was moved to the center of the

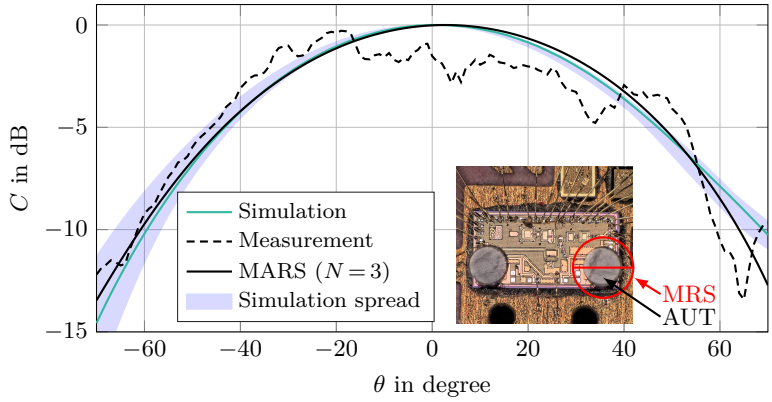

(a) E-plane.

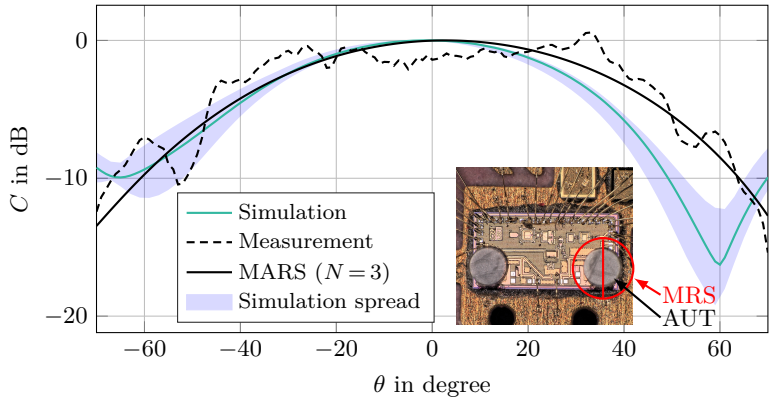

(b) H-plane.

Fig. 5.33: Measurement, simulation, and post-processed radiation patterns of the isolated chip-fed integrated antenna at 160 GHz. The highlighted area indicates the simulation results for different resonator positions (40 µm variation). The simulation model only contains the AUT. With $N = 3$, chip radiation is filtered [100], ©2017 IEEE.

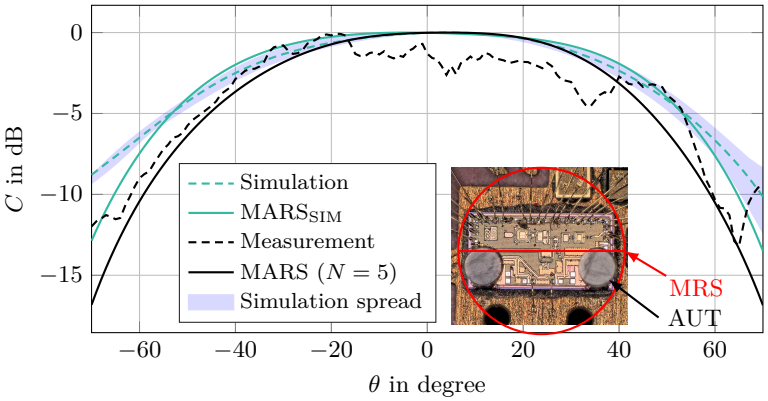

(a) E-plane.

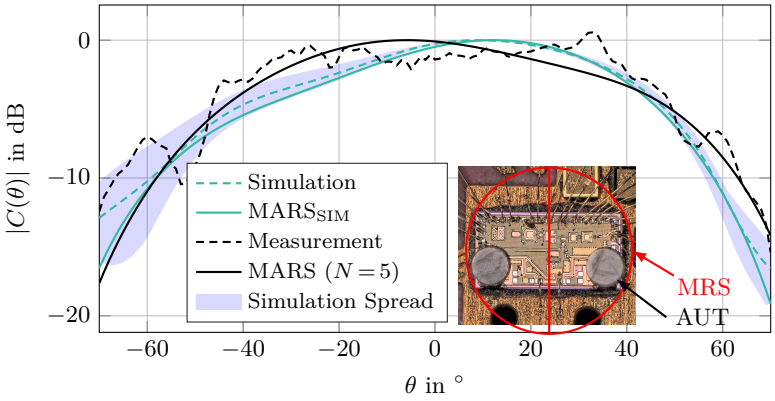

(b) H-plane.

Fig. 5.34: Comparison of measurement, simulation, and post-processed radiation patterns of the chip-fed integrated antenna at 160 GHz. In this case $N = 5$ was chosen such that the entire chip is taken into account. The simulation model includes the AUT and the chip [100], © 2017 IEEE.

chip instead of the phase center of the AUT, and N was increased to 5. The simulation result was obtained from a model containing the chip, but without bond wires and PCB. Due to the spherical MRS surface, the border region of the filtering cannot be perfectly aligned with the outline of the chip. Therefore, some bond-wire effects and PCB contributions cannot be removed (see circular red boundary region in Fig. 5.34a) and cause discrepancies to the simulation model. Additionally, the wide beam pattern increases the truncation effect at the edges, which can be seen when the simulation result is compared with the post-processed one. While these discrepancies increase the deviations between simulation and MARS result, the post-processing still filtered PCB-distortions, yielding a much smoother pattern.

Directivity

Using (3.4.5) on page 30, the directivity can be calculated based on measurement and post-processed results. Table 5.4 shows the results of the directivity simulation and measurement results for the isolated AUT and for the AUT with the surrounding chip. The unprocessed measurement result yields directivities that were 0.6 dB (isolated antenna) and 1.1 dB (antenna with chip) higher than the simulated values. These deviations could be decreased to 0.1 dB and 0.3 dB through MARS post-processing. The results clearly show that active integrated antenna measurements can also benefit from MARS post-processing.

Tab. 5.4: Directivity of the active integrated antenna measurement at 160 GHz.

Directivity in dB	Measurement in dB	MARS in dB	Simulation in dB
Isolated AUT	9.8	9.1	9.2
Chip with AUT	9.8	9.0	8.7

6 Conclusion

The ever-increasing demand for higher data rates requires new solutions for wireless data transmission and high accuracy remote sensing. However, at frequencies below 100 GHz, the channel capacity is limited due to strict bandwidth and transmit-power regulations. One approach to increase the channel capacity is to move to frequencies where higher bandwidths are available.

The ongoing progress in semiconductor fabrication processes now makes it possible to produce efficient integrated mm-wave circuits at frequencies above 100 GHz where bandwidths of many GHz can be realized. This makes the usage of mm-wave frequencies an interesting and promising solution to meet the demands of future high data-rate applications—even more so if this can be achieved with a small form factor and at low production costs by integrating the system into a single MMIC, using well-developed IC-production processes.

One important component for such systems is the antenna, because it is the junction between the guided and free-space propagation of the electromagnetic wave and thus constitutes the link of the chip to the outside world. Guaranteeing the required antenna characteristics is therefore a pivotal step in the development process.

Albeit a fairly new area of study, research in mm-wave antenna measurements has increased significantly in recent years, and established antenna-measurement companies are expanding their product portfolio to include systems that meet the stringent requirements of mm-waves. Research institutes are also intensifying their efforts to increase the achievable measurement accuracy and to overcome the challenges of small wavelengths and measurement setup interactions.

Different measurement setups have been proposed and improvements have been made in their mechanical setups. However, the measurement results of integrated mm-wave antennas that have been presented to date have lacked a specification of the measurement accuracy, without which the validity of a result cannot be guaranteed. This research project has made an important step towards justifying the validity of mm-wave antenna measurements—in spite of the various error sources—by quantifying, for the first time, the overall

measurement error at frequencies above 100 GHz. The main achievements for integrated mm-wave antenna measurements of this study are evident in the following:

- The realization of a dedicated, automated antenna measurement system with optimized components.
- A detailed analysis of measurement error mechanisms of integrated antenna measurements to quantify their individual impact on the result and to determine the overall accuracy of the measurement system at mm-wave frequencies.
- The successful application of post-processing algorithms to improve heavily distorted measurement results for isolated antennas (passive) and antennas within a system (active).

Chapter 3 introduces a novel measurement setup for mm-wave integrated antenna measurements. A robotic arm is used for maximum positional accuracy and flexibility in terms of scanning geometry, AUT specifications, and measurand. The impact of different components on the measurement result was analyzed in detail, in order to identify error sources and mitigate disturbances through component modifications. Several measurement configurations and methods (e.g. far-field, near-field, phase-center, and extrapolation measurements) were realized to allow for a thorough analysis of different antenna parameters. New approaches to identify reflection centers within the measurement environment (e.g. on the wafer probe) were presented and verified. This knowledge about problematic scattering centers can now be used to design components that are better suited for antenna measurements and cause less disturbances.

The flexibility of the setup is a key factor of the setup and lays the foundation for the error analysis performed in Chapter 4, as it makes it possible to analyze different error sources independently. Similarly, the setup was crucial to perform the post-processing in Chapter 5, which requires off-center measurement positions and an accurate knowledge of the phase center.

Following the optimization of the measurement setup, a comprehensive measurement accuracy analysis was performed for radiation pattern, directivity, and gain measurements of integrated antennas at frequencies over 100 GHz. Since integrated antenna measurements are not yet addressed in existing IEEE

antenna-measurement guidelines, 29 possible error terms were identified and analyzed for their impact on the measured quantity, before an overall measurement uncertainty for an integrated and a horn antenna was calculated.

While distortions can be reduced significantly with custom wafer probes, standard probes are much cheaper and readily available. Therefore, in Chapter 5, post-processing algorithms were examined to investigate whether the heavy distortions of standard probes can be removed. First, a new phase-center determination approach, based on the calculated spherical mode spectrum, was introduced which allows for sufficient accuracy in the presence of strong reflections to facilitate the required field translations for the MARS algorithm. By successfully applying the MARS algorithm to integrated antenna measurements at mm-wave frequencies, it was demonstrated that standard probes can achieve comparable results to dedicated custom-made probes, which marks a significant improvement on previous measurements that were dominated by the wafer probe distortions.

Lastly, it was shown that the post-processing technique can not only be used to filter probe reflections in passive measurements, but also to filter out surrounding circuitry of an antenna in a system (e.g. a radar chip). In this way, the characteristics of the isolated antenna can be obtained without access to the input signals of the AUT. The knowledge about the parameters of the isolated antenna can provide valuable information for diagnostics and the performance of the system in general.

The findings make it clear that the right measurement setup, combined with a careful component design and an appropriate post-processing method, make accurate and meaningful measurement results of integrated mm-wave antennas possible. This is a decisive result in the development of future transceiver MMICs, as it facilitates the design process of integrated antennas in the prototyping and system-design stages to realize reliable, well-designed, high-performance components.

A Appendix

Uncertainty Analysis of a Horn Antenna at 160 GHz

Table A.1 [108], ©2016 IEEE, shows the obtained results for the uncertainty analysis of a horn antenna at 160 GHz. The gain was not analyzed for the lack of a different reference antenna.

Tab. A.1: Uncertainty Budgets

#	Source of Uncertainty x_i	Affected Measurements	Uncertainty ($\pm$) $u(x_i)$	Radiation Pattern c_i	Radiation Pattern s_{x_i}	Directivity c_i	Directivity s_{x_i}
1	AUT pos x	RP/D/G	1.5 mm	0.024 dB/mm	0.5 mm	0.004 dB/mm	0.5 mm
2	AUT pos y	RP/D/G	1.5 mm	0.248 dB/mm	0.5 mm	0.008 dB/mm	0.5 mm
3	AUT pos z	RP/D/G	2 mm	0.041 dB/mm	0.67 mm	0.003 dB/mm	0.67 mm
4	AUT phase center	RP/D/G	5 mm/1 mm	0.023 dB/mm	1.67 mm	0.014 dB/mm	1.67 mm
5	AUT tilt	RP/D/G	0.125 °	1.369 dB/°	0.04 °	0.06 dB/°	0.04 °
6	AUT mismatch	G		—	—	—	—
7	Rx tilt	—	0.1 °	—	—	—	—
8	Rx length	—	100 µm	—	—	—	—
9	Rx phase center	—	5 mm	—	—	—	—
10	Rx Gain	—	0.2 dB	—	—	—	—
11	REF gain	G	0.1 dB	—	—	—	—
12	REF tilt	G	0.125 °	—	—	—	—
13	REF phase center	G	5 mm	—	—	—	—
14	REF mismatch	G		—	—	—	—
15	Connectors	G	0.4 dB	—	—	—	—
16	Trigger position	RP	350 µm				
17	Cable flex	RP		1 dB/dB	0.038 dB	1 dB/dB	0.012 dB
18	Noise	RP/G					
19	AUT-Rx-Polarization	RP/D/G	0.1 °	—	≈ 0	—	≈ 0
20	Distance	G	350 µm	—	—	—	—
21	Multiple reflections	RP/D/G		1 dB/dB	0.049 dB	1 dB/dB	0.036 dB
22	ϕ resolution (3 °)	D		—	—	1 dB/dB	0.005 dB
23	θ resolution (0.25 °)	RP/D		≈ 0	—		
24	Max θ	D		—	—	1 dB/dB	0.009 dB
25	Amplitude drift (1h)	D/G	0.025 dB	—	—	—	≈ 0
26	VNA crosstalk	RP/D	112 nV_{rms}	—	≈ 0	—	≈ 0
27	Receiver non-linearity	RP/D/G		1 dB/dB	0.049 dB	1 dB/dB	0.09 dB
28	Absorber placement	RP/D/G		—	≈ 0	—	≈ 0
Expanded uncertainty $U_c(y)$ (95% confidence):				0.3 dB		0.2 dB	

Bibliography

[1] E. Ozturk, D. Genschow, U. Yodprasit, B. Yilmaz, D. Kissinger, W. Debski, and W. Winkler, "Measuring Target Range and Velocity: Developments in Chip, Antenna, and Packaging Technologies for 60-GHz and 122-GHz Industrial Radars," *IEEE Microwave Magazine*, vol. 18, no. 7, pp. 26–39, Nov. 2017.

[2] D. Heberling and M. Geissler, "Trends on Handset Antennas," in *29th European Microwave Conference*, vol. 1, Oct. 1999, pp. 131–134.

[3] H. Rücker, B. Heinemann, and A. Fox, "Half-Terahertz SiGe BiCMOS Technology," *IEEE 12th Topical Meeting on Silicon Monolithic Integrated Circuits in RF Systems*, pp. 133–136, Jan. 2012.

[4] J. Böck, K. Aufinger, S. Boguth, C. Dahl, H. Knapp, W. Liebl, D. Manger, T. F. Meister, A. Pribil, J. Wursthorn, R. Lachner, B. Heinemann, H. Rücker, A. Fox, R. Barth, G. Fischer, S. Marschmeyer, D. Schmidt, A. Trusch, and C. Wipf, "SiGe HBT and BiCMOS Process Integration Optimization Within the DOTSEVEN Project," *IEEE Bipolar/BiCMOS Circuits and Technology Meeting – BCTM*, pp. 121–124, Oct. 2015.

[5] S. P. Voinigescu, S. Shopov, and P. Chevalier, "Millimeter-Wave Silicon Transistor and Benchmark Circuit Scaling Through the 2030 ITRS Horizon," in *Global Symposium on Millimeter-Waves (GSMM)*, May 2015, pp. 1–3.

[6] Y. Sun, M. Marinkovic, G. Fischer, W. Winkler, W. Debski, S. Beer, T. Zwick, M. G. Girma, J. Hasch, and C. J. Scheytt, "A Low-Cost Miniature 120 GHz SiP FMCW/CW Radar Sensor with Software Linearization," in *IEEE International Solid-State Circuits Conference Digest of Technical Papers*, Feb. 2013, pp. 148–149.

[7] M. Hitzler, L. Boehm, W. Mayer, and C. Waldschmidt, "Radiation Pattern Optimization for QFN Packages with On-Chip Antennas at 160 GHz," *IEEE Transactions on Antennas and Propagation*, Jun. 2018.

[8] W. T. Khan, A. L. V. López, A. Ç. Ulusoy, and J. Papapolymerou, "Packaging a W-Band Integrated Module With an Optimized Flip-Chip Interconnect on an Organic Substrate," *IEEE Transactions on Microwave Theory and Techniques*, vol. 62, no. 1, pp. 64–72, Jan. 2014.

[9] A. Bhutani, B. Goettel, T. Streitz, S. Scherr, W. Winkler, and T. Zwick, "Low-Cost Antenna-in-Package Solution for 122 GHz Radar Module," in *46th European Microwave Conference (EuMC)*, Oct. 2016, pp. 1469–1472.

[10] S. Beer, M. G. Girma, S. Yaoming, W. Winkler, W. Debski, J. Paaso, G. Kunkel, J. C. Scheytt, J. Hasch, and T. Zwick, "Flip-chip Package with Integrated Antenna on a Polyimide Substrate for a 122-GHz Bistatic Radar IC," in *7th European Conference on Antennas and Propagation (EuCAP)*, Apr. 2013, pp. 121–125.

[11] M. Hitzler, S. Saulig, L. Boehm, W. Mayer, W. Winkler, N. Uddin, and C. Waldschmidt, "Ultracompact 160-GHz FMCW Radar MMIC With Fully Integrated Offset Synthesizer," *IEEE Transactions on Microwave Theory and Techniques*, vol. 65, no. 5, pp. 1682–1691, May 2017.

[12] M. Hitzler, P. Grüner, L. Boehm, W. Mayer, and C. Waldschmidt, "On Monostatic and Bistatic System Concepts for mm-Wave Radar MMICs," *IEEE Transactions on Microwave Theory and Techniques*, vol. 66, no. 9, pp. 4204–4215, Sep. 2018.

[13] I. Sarkas, J. Hasch, A. Balteanu, and S. P. Voinigescu, "A Fundamental Frequency 120-GHz SiGe BiCMOS Distance Sensor With Integrated Antenna," *IEEE Transactions on Microwave Theory and Techniques*, vol. 60, no. 3, pp. 795–812, Mar. 2012.

[14] J. Grzyb, K. Statnikov, N. Sarmah, B. Heinemann, and U. R. Pfeiffer, "A 210–270-GHz Circularly Polarized FMCW Radar With a Single-Lens-Coupled SiGe HBT Chip," *IEEE Transactions on Terahertz Science and Technology*, vol. 6, no. 6, pp. 771–783, Nov. 2016.

[15] M. Hitzler, S. Saulig, L. Boehm, W. Mayer, W. Winkler, and C. Waldschmidt, "Compact bistatic 160 GHz transceiver MMIC with phase noise optimized synthesizer for FMCW radar," in *IEEE MTT-S International Microwave Symposium (IMS)*, May 2016, pp. 1–4.

[16] L. Rao, "In The Wake Of 'Antennagate', Apple's Stock Takes A Hit," e-ofStatisticalMethod://techcrunch.com/2010/07/13/in-the-wake-of-antennagate-apples-stock-takes-a-hit/m, accessed: 2017-09-20.

[17] L. Foged, O. Breinbjerg, S. Pivnenko, G. D. Massa, and C. Sabatier, "Antenna Measurement Facility Comparison within the European Antenna Centre of Excellence," in *European Microwave Conference*, vol. 2, Oct. 2005, pp. 4 pp.–792.

[18] IEEE, "IEEE Standard Test Procedures for Antennas," *ANSI/IEEE Std 149-1979*, 1979.

[19] K. A. Remley, J. A. Gordon, D. Novotny, A. E. Curtin, C. L. Holloway, M. T. Simons, R. D. Horansky, M. S. Allman, D. Senic, M. Becker, J. A. Jargon, P. D. Hale, D. F. Williams, A. Feldman, J. Cheron, R. Chamberlin, C. Gentile, J. Senic, R. Sun, P. B. Papazian, J. Quimby, M. Mujumdar, and N. Golmie, "Measurement Challenges for 5G and Beyond: An Update from the National Institute of Standards and Technology," *IEEE Microwave Magazine*, vol. 18, no. 5, pp. 41–56, Jul. 2017.

[20] M. D. Huang, M. H. A. J. Herben, A. C. F. Reniers, and P. F. M. Smulders, "Causes of Discrepancies Between Measurements and EM Simulations of Millimeter-Wave Antennas [Measurements Corner]," *IEEE Antennas and Propagation Magazine*, vol. 55, no. 6, pp. 139–149, Dec. 2013.

[21] "IEEE Standard for Definitions of Terms for Antennas," IEEE Std 145-2013 (Revision of IEEE Std 145-1993), pp. 1–50, Mar. 2014.

[22] A. D. Olver, "Compact Antenna Test Ranges," in *Seventh International Conference on Antennas and Propagation, ICAP 91 (IEE)*, Apr. 1991, pp. 99–108 vol.1.

[23] T. Sehm, J. Ala-Laurinaho, T. Hirvonen, and A. V. Raisanen, "Antenna measurements using a hologram CATR," *Electronics Letters*, vol. 35, no. 10, pp. 757–758, May 1999.

[24] M. Nel, J. Joubert, and J. W. Odendaal, "The Measurement of Complex Antenna Transfer Functions for Ultra-Wideband Antennas in a Compact Range [Measurements Corner]," *IEEE Antennas and Propagation Magazine*, vol. 56, no. 6, pp. 163–170, Dec. 2014.

[25] A. Lonnqvist, T. Koskinen, J. Hakli, J. Saily, J. Ala-Laurinaho, J. Mallat, V. Viikari, J. Tuovinen, and A. V. Raisanen, "Hologram-Based Compact Range for Submillimeter-Wave Antenna Testing," *IEEE Transactions on Antennas and Propagation*, vol. 53, no. 10, pp. 3151–3159, Oct. 2005.

[26] M. Dirix and D. Heberling, "Qualitative Quiet Zone Comparison Using Spherical Near-Field Scanning," in *2012 Loughborough Antennas Propagation Conference (LAPC)*, Nov. 2012, pp. 1–4.

[27] S. F. Gregson and C. G. Parini, "Examination of the Effect of Common CATR Quiet Zone Specifications on Antenna Pattern Measurement Uncertainties," in *Loughborough Antennas Propagation Conference (LAPC 2017)*, Nov. 2017, pp. 1–5.

[28] R. Cornelius and D. Heberling, "Spherical Near-Field Scanning With Pointwise Probe Correction," *IEEE Transactions on Antennas and Propagation*, vol. 65, no. 2, pp. 995–997, Feb. 2017.

[29] R. Cornelius and D. Heberling, "Correction of non-ideal probe orientations for spherical near-field antenna measurements," in *Antenna Measurement Techniques Association Symposium (AMTA)*, Oct. 2017, pp. 1–5.

[30] R. Cornelius and D. Heberling, "Spherical Wave Expansion With Arbitrary Origin for Near-Field Antenna Measurements," *IEEE Transactions on Antennas and Propagation*, vol. 65, no. 8, pp. 4385–4388, Aug. 2017.

[31] C. H. Schmidt and T. F. Eibert, "Multilevel Plane Wave Based Near-Field Far-Field Transformation for Electrically Large Antennas in Free-Space or Above Material Halfspace," *IEEE Transactions on Antennas and Propagation*, vol. 57, no. 5, pp. 1382–1390, May 2009.

[32] M. Dich, "Accurate Determination of Antenna Directivity," *IEEE Transactions on Antennas and Propagation*, vol. 45, no. 10, pp. 1502–1505, Oct. 1997.

[33] C.-T. Tai and C. Pereira, "An Approximate Formula for Calculating the Directivity of an Antenna," *IEEE Transactions on Antennas and Propagation*, vol. 24, no. 2, pp. 235–236, Mar. 1976.

[34] G. Mayhew-Ridgers, P. A. van Jaarsveld, J. W. Odendaal, and J. Joubert, "Accurate Gain Measurements for Large Antennas Using Modified Gain-Transfer Method," *IEEE Antennas and Wireless Propagation Letters*, vol. 13, pp. 369–371, Feb. 2014.

[35] S. V. Parekh, "The measurements column (antenna gain measurement)," *IEEE Antennas and Propagation Magazine*, vol. 32, no. 2, pp. 41–44, Apr. 1990.

[36] H.-C. Lu and T.-H. Chu, "A Quasi-Monostatic Reflective Three-Antenna Method for Antenna Gain and Scattering Measurement," in *IEEE Antennas and Propagation Society International Symposium. Transmitting Waves of Progress to the Next Millennium. 2000 Digest. Held in conjunction with: USNC/URSI National Radio Science Meeting (C*, vol. 3, Jul. 2000, pp. 1746–1749 vol.3.

[37] K. Harima, "Accurate Gain Measurement for Millimeter-Wave Horn and Open-Ended Waveguide Antennas," in *International Symposium on Antennas and Propagation (ISAP)*, Oct. 2012, pp. 1019–1022.

[38] H. Aumann, T. Schmitt, and D. Mooradd, "A Modification of the Two-Antenna Method to Determine the Phase Center Location as well as the Gain of a Wideband Antenna," in *IEEE International Symposium on Antennas and Propagation USNC/URSI National Radio Science Meeting*, Jul. 2015, pp. 854–855.

[39] C. L. Holloway, H. A. Shah, R. J. Pirkl, W. F. Young, D. A. Hill, and J. Ladbury, "Reverberation Chamber Techniques for Determining the Radiation and Total Efficiency of Antennas," *IEEE Transactions on Antennas and Propagation*, vol. 60, no. 4, pp. 1758–1770, Apr. 2012.

[40] H. A. Wheeler, "The Radiansphere around a Small Antenna," *Proceedings of the IRE*, vol. 47, no. 8, pp. 1325–1331, Aug. 1959.

[41] E. Newman, P. Bohley, and C. Walter, "Two Methods for the Measurement of Antenna Efficiency," *IEEE Transactions on Antennas and Propagation*, vol. 23, no. 4, pp. 457–461, Jul. 1975.

[42] R. H. Johnston and J. G. McRory, "An Improved Small Antenna Radiation-Efficiency Measurement Method," *IEEE Antennas and Propagation Magazine*, vol. 40, no. 5, pp. 40–48, Oct. 1998.

[43] M. A. Moharram and A. A. Kishk, "MIMO Antennas Efficiency Measurement Using Wheeler Caps," *IEEE Transactions on Antennas and Propagation*, vol. 64, no. 3, pp. 1115–1120, Mar. 2016.

[44] C. Cho, I. Park, and H. Choo, "A Modified Wheeler Cap Method for Efficiency Measurements of Probe-Fed Patch Antennas With Multiple Resonances," *IEEE Transactions on Antennas and Propagation*, vol. 58, no. 9, pp. 3074–3078, Sep. 2010.

[45] A. C. F. Reniers, A. R. van Dommele, A. B. Smolders, and M. H. A. J. Herben, "The Influence of the Probe Connection on mm-Wave Antenna Measurements," *IEEE Transactions on Antennas and Propagation*, vol. 63, no. 9, pp. 3819–3825, Sep. 2015.

[46] E. Lee, R. Soerens, E. Szpindor, and P. Iversen, "Challenges of 60 GHz on-Chip Antenna Measurements," *IEEE International Symposium on Antennas and Propagation USNC/URSI National Radio Science Meeting*, pp. 1538–1539, Jul. 2015.

[47] R. N. Simons and R. Q. Lee, "On-Wafer Characterization of Millimeter-Wave Antennas for Wireless Applications," *IEEE Transactions on Microwave Theory and Techniques*, vol. 47, no. 1, pp. 92–96, Jan. 1999.

[48] R. N. Simons, "Novel On-Wafer Radiation Pattern Measurement Technique for MEMS Actuator Based Reconfigurable Patch Antennas," *24th Antenna Measurement Techniques Association Meeting and Symposium*, Nov. 2002.

[49] R. N. Simons, D. Chun, and L. P. B. Katehi, "Reconfigurable Array Antenna Using Microelectromechanical Systems (MEMS) Actuators," *IEEE Antennas and Propagation Society International Symposium*, vol. 3, pp. 674–677, Jul. 2001.

[50] K. V. Caekenberghe, K. M. Brakora, W. Hong, K. Jumani, D. Liao, M. Rangwala, Y. Z. Wee, X. Zhu, and K. Sarabandi, "A 2–40 GHz Probe Station Based Setup for On-Wafer Antenna Measurements," *IEEE Transactions on Antennas and Propagation*, vol. 56, no. 10, pp. 3241–3247, Oct. 2008.

[51] T. Zwick, C. Baks, U. R. Pfeiffer, D. Liu, and B. P. Gaucher, "Probe Based MMW Antenna Measurement Setup," *IEEE Antennas and Propagation Society Symposium*, vol. 1, pp. 747–750, Jun. 2004.

[52] S. Ranvier, M. Kyrö, C. Icheln, C. Luxey, R. Staraj, and P. Vainikainen, "Compact 3-D on-Wafer Radiation Pattern Measurement System for 60 GHz Antennas," *Microwave and Optical Technology Letters*, vol. 51, no. 2, pp. 319–324, Dec. 2009. [Online]. Available: http://dx.doi.org/10.1002/mop.24034

[53] D. Titz, F. Ferrero, and C. Luxey, "Development of a Millimeter-Wave Measurement Setup and Dedicated Techniques to Characterize the Matching and Radiation Performance of Probe-Fed Antennas [Measurements Corner]," *IEEE Antennas and Propagation Magazine*, vol. 54, no. 4, pp. 188–203, Aug. 2012.

[54] D. Titz, M. Kyrö, F. Ferrero, S. Ranvier, C. Luxey, P. Brachat, G. Jacquemod, and P. Vainikainen, "Calibration Methodology for a 3D Radiation Pattern Set-up of Probe-fed Millimeter-Wave Antennas," *Microwave and Optical Technology Letters*, vol. 54, no. 5, pp. 1183–1189, May 2012. [Online]. Available: http://dx.doi.org/10.1002/mop.26795

[55] S. Beer and T. Zwick, "Probe Based Radiation Pattern Measurements for Highly Integrated Millimeter-Wave Antennas," *Proceedings of the Fourth European Conference on Antennas and Propagation*, pp. 1–5, Apr. 2010.

[56] J. Saily, P. Eskelinen, and A. V. Raisanen, "Pilot Signal-Based Real-Time Measurement and Correction of Phase Errors Caused by Microwave Cable Flexing in Planar Near-Field Tests," *IEEE Transactions on Antennas and Propagation*, vol. 51, no. 2, pp. 195–200, Feb. 2003.

[57] A. C. F. Reniers, A. R. van Dommele, M. D. Huang, and M. H. A. J. Herben, "Disturbing Effects of Microwave Probe on Mm-Wave Antenna Pattern Measurements," *The 8th European Conference on Antennas and Propagation (EuCAP)*, pp. 161–164, Apr. 2014.

[58] E. C. Lee, E. Szpindor, and W. E. McKinzie III, "Mitigating Effects of Interference in On-Chip Antenna Measurements," *AMTA 37th Annual Meeting and Symposium, Long Beach, California, USA*, Oct. 2015.

[59] D. J. van Rensburg and S. F. Gregson, "Parametric Study of Probe Positioning Errors in Articulated Spherical Near-Field Test Systems for Mm-Wave Applications," *IEEE Conference on Antenna Measurements Applications (CAMA)*, pp. 1–4, Nov. 2014.

[60] D. Novotny, J. Gordon, J. Coder, M. Francis, and J. Guerrieri, "Performance Evaluation of a Robotically Controlled Millimeter-Wave Near-Field Pattern Range at the NIST," *7th European Conference on Antennas and Propagation (EuCAP)*, pp. 4086–4089, Apr. 2013.

[61] J. A. Gordon, D. R. Novotny, M. H. Francis, R. C. Wittmann, M. L. Butler, A. E. Curtin, and J. R. Guerrieri, "Millimeter-Wave Near-Field Measurements Using Coordinated Robotics," *IEEE Transactions on Antennas and Propagation*, vol. 63, no. 12, pp. 5351–5362, Dec. 2015.

[62] D. Novotny, M. Francis, R. Wittmann, J. Gordon, J. Guerrieri, and A. Curtin, "Multi-Purpose Configurable Range for Antenna Testing up to 220 GHz," in *10th European Conference on Antennas and Propagation (EuCAP)*, Apr. 2016, pp. 1–3.

[63] J. A. Gordon, D. R. Novotny, M. H. Francis, R. C. Wittmann, M. L. Butler, A. E. Curtin, J. R. Guerrieri, L. Periasamy, and A. J. Gasiewski, "An All-Metal, 3-D-Printed CubeSat Feed Horn: An assessment of performance conducted at 118.7503 GHz using a Robotic Antenna Range." *IEEE Antennas and Propagation Magazine*, vol. 59, no. 2, pp. 96–102, Apr. 2017.

[64] M. Saporetti, L. J. Foged, L. Scialacqua, F. Saccardi, M. Mercier, J. Lui, F. Z. Xue, L. T. Chen, and B. L. Bu, "Antenna Measurement System Verification by Correlation with Facility-Comparison Campaign in the Framework of the European Association of Antennas and Propagation," in *IEEE International Wireless Symposium (IWS 2014)*, Mar. 2014, pp. 1–4.

[65] M. A. Saporetti, L. Foged, M. S. Castaner, S. Pivnenko, R. Cornelius, and D. Heberling, "Description and Results: Antenna Measurement Facility Comparisons [Measurements Corner]," *IEEE Antennas and Propagation Magazine*, vol. 59, no. 3, pp. 108–116, Jun. 2017.

[66] S. Pivnenko, J. M. Nielsen, and O. Breinbjerg, "Very High-Accuracy Calibration of Radiation Pattern and Gain of a Near-Field Probe," *Antennas and Propagation (EuCAP), 8th European Conference on, The Hague, Netherlands*, pp. 1690–1694, Apr. 2014.

[67] L. Foged, B. Bencivenga, L. Durand, O. Breinbjerg, S. Pivnenko, C. Sabatier, H. Ericsson, B. Svensson, A. Alexandridis, S. Burgos, M. Sierra-Castaner, J. Zackrisson, and M. Boettcher, "Error Calculation Techniques and their Application to the Antenna Measurement Facility Comparison within the European Antenna Centre of Excellence," in *The Second European Conference on Antennas and Propagation, EuCAP 2007*, Nov. 2007, pp. 1–6.

[68] NIST/SEMATECH, "e-Handbook of Statistical Methods," http://itl.nist.gov/div898/handbook/mpc/mpc.htm, accessed: 2017-09-12.

[69] NASA, "Measurement Uncertainty Analysis Principles and Methods," *NASA Measurement Quality Assurance Handbook – ANNEX 3*, Jul. 2010.

[70] H. Eriksson, B. Svensson, and P. Magnusson, "Gain Calibration Uncertainties for Standard Gain Horn Calibration at a Compact Antenna Test Range," *Proceedings of the 5th European Conference on Antennas and Propagation (EUCAP)*, pp. 3746–3750, Apr. 2011.

[71] A. C. Newell, "Error Analysis Techniques for Planar Near-Field Measurements," *IEEE Transactions on Antennas and Propagation*, vol. 36, no. 6, pp. 754–768, Jun. 1988.

[72] M. A. Qureshi, C. H. Schmidt, K. A. Yinusa, and T. F. Eibert, "Far-Field Uncertainty due to Instrumentation Errors in Multilevel Plane Wave Based Near-Field Far-Field Transformed Planar Near-Field Measurements," *6th European Conference on Antennas and Propagation (EUCAP)*, pp. 2518–2522, Mar. 2012.

[73] M. H. Francis, "Estimating Far-Field Errors due to Mechanical Errors in Spherical Near-Field Scanning," *Proceedings of the IEEE International Symposium on Antennas and Propagation*, pp. 1–2, Jul. 2012.

[74] P. Pelland, G. Hindman, and D. J. van Rensburg, "Spherical Near-Field Alignment Sensitivity for Polar and Equatorial Antenna Measurements," *AMTA 2016 Proceedings*, pp. 1–6, Oct. 2016.

[75] S. R. Nichols, "Application of Spherical Near-Field Uncertainty Analysis to Positioner Design," *The 8th European Conference on Antennas and Propagation (EuCAP)*, pp. 154–158, Apr. 2014.

[76] M. H. Francis and R. C. Wittmann, "Uncertainty Analysis for Spherical Near-Field Measurements," *Proceedings of the Antenna Measurement Techniques Association (AMTA)*, Oct. 2003.

[77] F. Martin, S. Burgos, M. Sierra-Castaner, C. V. Pou, and J. L. Besada, "Error Corrections in Outdoor Cylindrical Near Field Radar Antenna Measurement System," *The Second European Conference on Antennas and Propagation, EuCAP*, pp. 1–6, Nov. 2007.

[78] M. S. Castaner, S. B. Martinez, F. M. Jimenez, and J. L. Besada, "Error Analysis and Simulator in Cylindrical Near Field Antenna Measurement Systems," *IEEE Antennas and Propagation Society International Symposium*, pp. 1649–1652, Jun. 2007.

[79] S. Blalock and J. A. Fordham, "Antenna Measurement Uncertainty Method for Measurements in Compact Antenna Test Ranges," *10th European Conference on Antennas and Propagation (EuCAP)*, pp. 1–5, Apr. 2016.

[80] V. Lingasamy, K. T. Selvan, T. S. Bird, and V. Venkatesan, "Uncertainty Estimation in the Two-Antenna Gain Measurement of a 4.8-11-GHz Double-Ridged Horn [Measurements Corner]," *IEEE Antennas and Propagation Magazine*, vol. 59, no. 1, pp. 110–113, Feb. 2017.

[81] L. Boehm, M. Hehl, and C. Waldschmidt, "Influence of the Wafer Chuck on Integrated Antenna Measurements," in *German Microwave Conference (GeMiC)*, Mar. 2016, pp. 274–277.

[82] L. Boehm, A. Foerstner, M. Hitzler, and C. Waldschmidt, "Reflection Reduction Through Modal Filtering for Integrated Antenna Measurements Above 100 GHz," *IEEE Transactions on Antennas and Propagation*, vol. 65, no. 7, pp. 3712–3720, Jul. 2017.

[83] D. Hou, W. Hong, W. L. Goh, J. Chen, Y.-Z. Xiong, S. Hu, and M. Madihian, "D-Band On-Chip Higher-Order-Mode Dielectric-Resonator Antennas fed by Half-Mode Cavity in CMOS Technology," *Antennas and Propagation Magazine, IEEE*, vol. 56, no. 3, pp. 80–89, Jun. 2014.

[84] L. Boehm, F. Boegelsack, M. Hitzler, and C. Waldschmidt, "An Automated Millimeter-Wave Antenna Measurement Setup Using a Robotic Arm," *IEEE AP-S Symposium on Antennas and Propagation*, Jul. 2015.

[85] L. Boehm, F. Boegelsack, M. Hitzler, and C. Waldschmidt, "The Challenges of Measuring Integrated Antennas at Millimeter-Wave Frequencies [Measurements Corner]," *IEEE Antennas and Propagation Magazine*, vol. 59, no. 4, pp. 84–92, Aug. 2017.

[86] Python Software Foundation, "Python Language Reference, version 3.4," http://www.python.org.

[87] J. Hatzis, P. Pelland, and G. Hindman, "Implementation of a Combination Planar and Spherical Near-Field Antenna Measurement System Using an Industrial 6-Axis Robot," *AMTA Proceedings*, pp. 1–6, Oct. 2016.

[88] S. Beer, "Methoden und Techniken zur Integration von 122 GHz Antennen in miniaturisierte Radarsensoren," *Karlsruher Forschungsberichte aus dem Institut für Hochfrequenztechnik und Elektronik*, Feb. 2013.

[89] P. A. Beeckman, "Analysis of Phase Errors in Antenna-Measurements Applications to Phase-Pattern Corrections and Phase-Centre Determination," *IEE Proceedings H – Microwaves, Antennas and Propagation*, vol. 132, no. 6, pp. 391–394, Oct. 1985.

[90] T. Kleine-Ostmann, D. Ulm, and T. Schrader, "Phase Center Estimation and Correction of Multi-Path Effects for the Calibration of mm-Wave Antennas," *41st International Conference on Infrared, Millimeter, and Terahertz waves (IRMMW-THz)*, pp. 1–2, Sep. 2016.

[91] A. C. Newell and G. Hindman, "The Alignment of a Spherical Near-Field Measurement System Using Electrical Measurements," *IEEE Antennas and Propagation Society International Symposium. Digest. Antennas: Gateways to the Global Network. Held in conjunction with: USNC/URSI National Radio Science Meeting (Cat. No.98CH36)*, vol. 3, pp. 1327–1330 vol.3, Jun. 1998.

[92] A. P. Mynster, J. M. Nielsen, and S. Pivnenko, "Electrical Alignment of Antenna Coordinate System in a Planar Near-Field Setup," *Proceedings*

of the 5th European Conference on Antennas and Propagation (EUCAP), pp. 678–682, Apr. 2011.

[93] L. L. Coq, O. Lafond, and M. Himdi, "Flip Test Procedure for Positioning System Errors and Antenna Phase Centre Determinations," *Proceedings of the Fourth European Conference on Antennas and Propagation*, pp. 1–4, Apr. 2010.

[94] L. Boehm, F. Boegelsack, M. Hitzler, and C. Waldschmidt, "Enhancements in Mm-Wave Antenna Measurements: Automatic Alignment and Achievable Accuracy," *IET Microwaves, Antennas Propagation*, vol. 11, no. 12, pp. 1676–1680, Oct. 2017.

[95] E. Muehldorf, "The Phase Center of Horn Antennas," *IEEE Transactions on Antennas and Propagation*, vol. 18, no. 6, pp. 753–760, Nov. 1970.

[96] C. Balanis, *Antenna Theory: Analysis and Design*, ser. Harper & Row series in electrical engineering. Wiley, 1982. [Online]. Available: https://books.google.de/books?id=wARTAAAAMAAJ

[97] J. Kang, "Antenna Measurements and Applications in Millimeter Frequency Range," in *IEEE Conference on Antenna Measurements Applications (CAMA)*, Dec. 2017, pp. 5–8.

[98] J. S. Kang and J. H. Kim, "Extrapolation range for D-band standard gain horn antenna measurement," in *Proc. of 38th Annual Meeting and Symposium of the Antenna Measurement Techniques Association (AMTA)*, Oct. 2016, pp. 5–8.

[99] A. C. F. Reniers, Q. Liu, M. H. A. J. Herben, and A. B. Smolders, "Review of the Accuracy and Precision of mm-wave Antenna Simulations and Measurements," *10th European Conference on Antennas and Propagation (EuCAP)*, pp. 1–5, Apr. 2016.

[100] L. Boehm, M. Hitzler, A. Foerstner, and C. Waldschmidt, "The Performance of Modal Filtering in Passive and Active Integrated Antenna Measurements at 160 GHz," in *AMTA 39th Annual Meeting and Symposium, Atlanta, Georgia, USA*, Oct. 2017.

[101] L. Tiemeijer, R. Havens, A. Jansman, and Y. Bouttement, "Comparison of the "Pad-Open-Short" and "Open-Short-Load" Deembedding Techniques for Accurate on-wafer RF Characterization of High-Quality Passives," *IEEE Transactions on Microwave Theory and Techniques*, vol. 53, no. 2, pp. 723–729, Feb. 2005.

[102] L. Boehm, M. Hitzler, F. Roos, and C. Waldschmidt, "Probe Influence on Integrated Antenna Measurements at Frequencies Above 100 GHz," in *46th European Microwave Conference (EuMC)*, Oct. 2016, pp. 552–555.

[103] L. Boehm and C. Waldschmidt, "Scattering Center Determination for Integrated Antenna Measurements at mm-Wave Frequencies," in *11th European Conference on Antennas and Propagation (EUCAP)*, Mar. 2017, pp. 1622–1625.

[104] Z.-M. Tsai, Y.-C. Wu, S.-Y. Chen, T. Lee, and H. Wang, "A V-Band On-Wafer Near-Field Antenna Measurement System Using an IC Probe Station," *Antennas and Propagation, IEEE Transactions on*, vol. 61, no. 4, pp. 2058–2067, Apr. 2013.

[105] G. Gentile, V. Jovanovic, M. Pelk, L. Jiang, R. Dekker, P. de Graaf, B. Rejaei, L. de Vreede, L. Nanver, and M. Spirito, "Silicon-filled rectangular waveguides and frequency scanning antennas for mm-wave integrated systems," *IEEE Transactions on Antennas and Propagation*, vol. 61, no. 12, pp. 5893–5901, Dec. 2013.

[106] K. A. Ladds, H. P. Nel, and T. Stander, "A Novel E-Band Nearfield Scanner for Wafer Probed on-Chip Antenna Characterisation," in *10th European Conference on Antennas and Propagation (EuCAP)*, Apr. 2016, pp. 1–4.

[107] L. Boehm, S. Pledl, F. Boegelsack, M. Hitzler, and C. Waldschmidt, "Robotically Controlled Directivity and Gain Measurements of Integrated Antennas at 280 GHz," *European Microwave Conference (EuMC), Paris, France*, Sep. 2015.

[108] L. Boehm, F. Boegelsack, M. Hitzler, S. Wiehler, and C. Waldschmidt, "Accuracy Evaluation for Antenna Measurements at mm-Wave Frequencies," in *10th European Conference on Antennas and Propagation (EuCAP)*, Apr. 2016, pp. 1–5.

[109] C. Parini, S. Gregson, J. McCormick, and D. J. van Rensburg, *Theory and Practice of Modern Antenna Range Measurements (IET Electromagnetic Wave Series 55)*. London, United Kingdom: The Institution of Engineering and Technology, 2014.

[110] R. V. D. Jough, M. Hajian, and L. P. Ligthart, "Antenna Time-Domain Measurement Techniques," *IEEE Antennas and Propagation Magazine*, vol. 39, no. 5, pp. 7–11, Oct. 1997.

[111] B. N. Levitas, "Time Domain Antenna Measurement Systems," in *3rd International Conference on Ultrawideband and Ultrashort Impulse Signals*, Sep. 2006, pp. 90–95.

[112] B. N. Levitas and D. M. Ponomarev, "Antenna Measurements in Time Domain," in *IEEE Antennas and Propagation Society International Symposium Digest*, vol. 1, Jul. 1996, pp. 573–576 vol.1.

[113] K. Technologies, "Time Domain Analysis Using a Network Analyzer," http://literature.cdn.keysight.com/litweb/pdf/5989-5723EN.pdf, accessed: 2018-01-15.

[114] J. L. Araque Quijano and G. Vecchi, "Field and Source Equivalence in Source Reconstruction on 3D Surfaces," *Progress In Electromagnetics Research*, pp. 67–100, Jan. 2010.

[115] J. L. A. Quijano, G. Vecchi, M. Sabbadini, L. Scialacqua, B. Bencivenga, F. Saccardi, and L. J. Foged, "Source Reconstruction as a Diagnostics Tool in Advanced Antenna Measurements," *IEEE International Conference on Microwaves, Communications, Antennas and Electronic Systems (COMCAS 2011)*, pp. 1–6, Nov. 2011.

[116] J. L. A. Quijano and G. Vecchi, "Near- and Very Near-Field Accuracy in 3-D Source Reconstruction," *IEEE Antennas and Wireless Propagation Letters*, vol. 9, pp. 634–637, Jun. 2010.

[117] Y. Alvarez, F. Las-Heras, and C. Garcia, "The Sources Reconstruction Method for Antenna Diagnostics and Imaging Applications," *Solutions and Applications of Scattering, Propagation, Radiation and Emission of Electromagnetic Waves*, 2012.

[118] F. Las-Heras, M. R. Pino, S. Loredo, Y. Alvarez, and T. K. Sarkar, "Evaluating Near-Field Radiation Patterns of Commercial Antennas," *IEEE Transactions on Antennas and Propagation*, vol. 54, no. 8, pp. 2198–2207, Aug. 2006.

[119] J. L. A. Quijano, G. Vecchi, L. J. Foged, and F. Chauvet, "Advanced Antenna Diagnostics and Pattern Processing Form Measured Data," in *International Conference on Applications of Electromagnetism and Student Innovation Competition Awards (AEM2C)*, Aug. 2010, pp. 61–65.

[120] J. L. A. Quijano, G. Vecchi, M. Sabbadini, L. Scialacqua, B. Bencivenga, F. Mioc, and L. Foged, "Source Reconstruction in Advanced Processing of Antenna Measurements," in *Proceedings of the 5th European Conference on Antennas and Propagation (EUCAP)*, Apr. 2011, pp. 3875–3879.

[121] Y. Alvarez, F. Las-Heras, and M. R. Pino, "Reconstruction of Equivalent Currents Distribution over Arbitrary Three-Dimensional Surfaces Based on Integral Equation Algorithms," *IEEE Transactions on Antennas and Propagation*, vol. 55, no. 12, pp. 3460–3468, Dec. 2007.

[122] M. Sierra-Castañer, P. González-Blanco García, M. J. López Morales, F. Saccardi, and L. J. Foged, "Time and spatial filtering for echo reduction in antenna measurements," *AMTA 37th Annual Meeting and Symposium, Long Beach, California, USA*, 2015.

[123] J. L. A. Quijano, L. Scialacqua, J. Zackrisson, L. J. Foged, M. Sabbadini, and G. Vecchi, "Suppression of Undesired Radiated Fields Based on Equivalent Currents Reconstruction From Measured Data," *IEEE Antennas and Wireless Propagation Letters*, vol. 10, pp. 314–317, Apr. 2011.

[124] B. Toland and Y. Rahmat-Samii, "Application of FFT and DFT for Image Reconstruction of Planar Arrays in Microwave Holographic Diagnostics," in *Antennas and Propagation Society International Symposium. AP-S. Merging Technologies for the 90's. Digest.*, May 1990, pp. 292–295 vol.1.

[125] F. J. Cano-Facila, S. Burgos, F. Martin, and M. Sierra-Castaner, "New Reflection Suppression Method in Antenna Measurement Systems Based

on Diagnostic Techniques," *IEEE Transactions on Antennas and Propagation*, vol. 59, no. 3, pp. 941–949, Mar. 2011.

[126] A. Yaghjian, "An Overview of Near-Field Antenna Measurements," *IEEE Transactions on Antennas and Propagation*, vol. 34, no. 1, pp. 30–45, Jan. 1986.

[127] J. Hanfling, G. Borgiotti, and L. Kaplan, "The Backward Transform of the Near Field for Reconstruction of Aperture Fields," in *Antennas and Propagation Society International Symposium*, vol. 17, Jun. 1979, pp. 764–767.

[128] C. Balanis, *Advanced Engineering Electromagnetics*. Wiley, 1989.

[129] J. L. A. Quijano and G. Vecchi, "Improved-Accuracy Source Reconstruction on Arbitrary 3-D Surfaces," *IEEE Antennas and Wireless Propagation Letters*, vol. 8, pp. 1046–1049, Sep. 2009.

[130] S. Rao, D. Wilton, and A. Glisson, "Electromagnetic Scattering by Surfaces of Arbitrary Shape," *IEEE Transactions on Antennas and Propagation*, vol. 30, no. 3, pp. 409–418, May 1982.

[131] L. J. Foged, L. Scialacqua, P. Iversen, and E. Szpindor, "Detection and Suppression of Scattered Fields from Coplanar Micro-Probe and Positioner in Millimeter Wave on-Chip Antenna Measurements," *International Symposium on Antennas and Propagation (ISAP)*, pp. 126–127, Oct. 2016.

[132] J. E. Hansen, *Spherical Near-Field Antenna Measurements (IET Electromagnetic Wave Series 26)*. London, UK: The Institution of Engineering and Technology, 2008.

[133] G. Hindman and A. Newell, "Reflection Suppression in a Large Spherical Near-Field Range," *AMTA 27th Annual Meeting & Symposium, Newport, RI*, 2005. [Online]. Available: http://www.nearfield.com/amta/AMTA05-GH.pdf

[134] G. Hindman, "Reflection Suppression to Improve Anechoic Chamber Performance," *AMTA Europe*, pp. 297–302, 2006. [Online]. Available: http://www.nearfield.com/amta/2006_GH_AMTA_Europe_MARS.pdf

[135] S. F. Gregson, A. C. Newell, and G. E. Hindman, "Reflection Suppression in Cylindrical Near-Field Antenna Measurement Systems–Cylindrical MARS," *Antenna Measurement Techniques Association (AMTA), 31st Annual Meeting & Symposium, Salt Lake City, UT*, 2009. [Online]. Available: http://www.nearfield.com/amta/AMTA_09_Papers/2009_AMTA_SG_Reflection_Suppression_in_Cylindrical_Near-field.pdf

[136] S. F. Gregson, A. C. Newell, and G. E. Hindman, "Reflection Suppression in Cylindrical Near-Field Measurements of Electrically Small Antennas," in *Loughborough Antennas Propagation Conference*, Nov. 2009, pp. 393–396.

[137] S. F. Gregson, A. C. Newell, G. E. Hindman, and M. J. Carey, "Advances in Cylindrical Mathematical Absorber Reflection Suppression," in *Proceedings of the Fourth European Conference on Antennas and Propagation*, Apr. 2010, pp. 1–5.

[138] S. F. Gregson, A. C. Newell, G. E. Hindman, and M. J. Carey, "Application of Mathematical Absorber Reflection Suppression to Planar Near-Field Antenna Measurements," *5th European Conference on Antennas and Propagation*, pp. 3412–3416, Apr. 2011.

[139] S. F. Gregson, J. Dupuy, C. G. Parini, A. C. Newell, and G. E. Hindman, "Application of Mathematical Absorber Reflection Suppression to Far-Field Antenna Measurements," in *Loughborough Antennas Propagation Conference*, Nov. 2011, pp. 1–4.

[140] P. Morse and H. Feshbach, *Methods of Theoretical Physics Part II*. New York, USA: McGraw-Hill Book Compnay, Inc., 1953.

[141] J. A. Stratton, *Electromagnetic Theory*. New York, USA: McGraw-Hill Book Company, 1941.

[142] J. A. Nelder and R. Mead, "A Simplex Method for Function Minimization," *The Computer Journal*, vol. 7, no. 4, pp. 308–313, 1965. [Online]. Available: http://comjnl.oxfordjournals.org/content/7/4/308.abstract

Herausgeber:
Prof. Dr.-Ing. Christian Waldschmidt

Integrated antennas are a crucial component in the development of high-performance, fully-integrated transceiver chips. However, due to the small size of integrated antennas and their complicated contacting fixtures, existing measurement setups cannot be used for their characterization. Therefore, new approaches must be investigated to obtain reliable and accurate measurement results and thus to make optimized on-chip antenna designs possible.

This work addresses the challenges of measuring integrated antennas at mm-wave frequencies. It introduces a robotic measurement setup to accurately determine the radiation properties of on-chip antennas and quantifies the achievable measurement accuracy through an in-depth uncertainty analysis. The study also analyzes post-processing techniques to mitigate severe distortions that occur in the measurement environment.

ISBN: 978-3-948303-04-4 ISBN: 978-3-948303-05-1 (E-Book)